A STUDY OF THE ^{9}Be NUCLEUS

Thesis by

Charles Lewis Cocke, Jr.

In Partial Fulfillment of the Requirements

For the Degree of

Doctor of Philosophy

California Institute of Technology

Pasadena, California

1967

(Submitted May 5 , 1967)

ii

ACKNOWLEDGMENTS

ABSTRACT

The reaction ^{7}Li(^{3}He, p)^{9}Be has been used to measure excitations and intrinsic widths of levels in ^{9}Be below the ^{7}Li + d threshold. Previously unreported levels have been found at excitations of (13.78 ± .03) MeV and (16.671 ± .008) MeV with widths of (590 ± 60) keV and (41 ± 4) keV respectively. Two overlapping levels have been found at (11.81 ± .02) MeV and (11.29 ± .03) MeV with widths of (400 ± 30) keV and (620 ± 70) keV respectively. Branching ratios from ^{9}Be levels populated in this reaction to the ground and first excited states of ^{8}Be have been measured by observing the associated protons in coincidence with the decay neutrons. Branching ratios were found to be:

Excitation in ^{9}Be (MeV)	Branching Ratio (percent)	Final Nucleus
2.43	7.5 ± 1.5	^{8}Be(g.s.)
3.03	87 ± 13	
4.65	13 ± 4	
6.76	≤ 2	
11.29	≤ 2	
11.81	≤ 3	
6.76	.41 ≤ B.R. ≤ .69	^{8}Be(2^+)
11.29	14 ± 4	
11.81	12 ± 4	

Corresponding reduced widths for neutron emission are calculated and a comparison of the results with the expectations of current nuclear models is made. In particular the measured branching ratio to ^{8}Be(g. s.) from ^{9}Be(2. 43 MeV) corresponds to an f-wave reduced width of $\theta_f^2 = 2.1 \times 10^{-2}$, in units of $\hbar^2/mR^2$, with R = 4. 35 fm. A comparison of this value with that predicted by a Nilsson model calculation, in which ^{9}Be is taken to be a deformed nucleus, is discussed. The measured value for θ_f^2 is found to be consistent with that expected on the basis of measured E2-transition rates between rotational levels in ^{9}Be.

TABLE OF CONTENTS

I. INTRODUCTION

The development of a consistent picture of the nucleus
has come to involve not so much the solving of a complex equation
of motion as the direct guessing of the solution. At the heart of
current efforts to understand nuclear structure lie attempts to build
models of the nucleus which can account for its various properties.
In this context the nuclear theorist must have at his disposal
considerable experimental information on the properties of nuclear
levels. Experimentally, the excitation region below the ^{7}Li + d
threshold at 16.693 MeV in ^{9}Be has been, until recently, quite
poorly known. This is due in part to the absence in this region
of two-body particle channels through which ^{9}Be may be formed
as a compound nucleus, and to the relatively simple structure of
the excited levels which makes them broad and difficult to study
experimentally. This thesis finds partial motivation in filling in
some of the experimental facts necessary for the theorist to
formulate a consistent picture of ^{9}Be.

Of more specific interest in the case of ^{9}Be is the possi-
bility that this nucleus may exhibit collective features. In the
region of light nuclei with $4 \leq A \leq 16$, the most widely used
nuclear model has been the independent particle shell model,
using the configuration $(1s)^4 (1p)^{A-4}$. The success of this model
in describing level spacings, spins and parities, beta-decay matrix
elements, M1 transition rates and magnetic dipole moments has
been impressive (Barker, 1966; Inglis, 1953; Kurath, 1956;
Cohen and Kurath, 1965). A notable failure of the model has been
its prediction of quadrupole moments and E2 transition rates which
are often several times lower than those observed experimentally

(Warburton et al., 1963; Warburton et al., 1963 a; van der Merwe, 1963). As has been found in intermediate- and high-A nuclei, such large quadrupole matrix elements may be indicative of collective nuclear modes of excitation.

The idea that nuclei as low as the 1p-shell may exhibit collective features is not new. ^{8}Be is well known to have an energy spectrum interpretable as a rotational band based on its 0^+ ground state. Chesterfield and Spicer (1963) have found rotational bands in the energy spectrum of ^{7}Li, and have given a successful description of its ground state magnetic dipole and electric quadrupole moments and the lifetime of its first excited state using a rotational model.

The ^{9}Be nucleus lies far enough from the ends of the 1p-shell that it may be expected to display a large equilibrium deformation. This suspicion is strengthened by the rotational character of its neighbor, ^{8}Be. Blair and Henley (1959) have proposed an alpha-particle model for ^{9}Be to explain the selective population, in the inelastic scattering of alpha-particles, protons and deuterons from ^{9}Be, of rotational levels based on the ground state. They observe that the ground state, 2.43 MeV state, 6.76 MeV state and 11.3 MeV state display a level spacing and population in inelastic scattering experiments consistent with their belonging to a $K = 3/2^-$ rotational band. Kunz (1960) has extended the use of this model to include a $K = 1/2^-$ band, and has found that the quadrupole moment predicted by the model is about a factor of two greater than that predicted by the shell model. Kunz also points out that overlap of the wave functions of the nucleons in the alpha-particles with a 1s-wave function decreases as the nucleus becomes more elongated. The result is that a neutron in a nominal

2s-orbit is allowed a greater component of the 1s-wave function, and a correspondingly lower energy. The low energy of the 1.7 MeV positive parity state may be due to this characteristic. Nguyen Ngoc et al. (1963) have observed that the ratios of the E2 widths to the ^{9}Be ground state from levels at 2.43 and 6.76 MeV are in excellent agreement with rotational model predictions.

This thesis presents a rather open ended study of the ^{9}Be nucleus. As described below, the level scheme of ^{9}Be is not well known. Consequently the first stage of the experimental work was concerned with measuring level positions and total widths of the levels. To this end the reaction ^{7}Li(^{3}He, p)^{9}Be was used.

While considerable information on the spins and parities and electromagnetic matrix elements of ^{9}Be levels is now becoming available, very little is known of the wave functions. The second stage of the work was concerned with measuring the branching ratios in the decay of excited levels of ^{9}Be to the ground and first excited states of ^{8}Be. This information, when combined with the measurement of the total widths of the levels, allows one to calculate neutron reduced widths into these two outgoing channels.

II. $^7\text{Li}(^3\text{He}, p)\,^9\text{Be*}$ SINGLES MEASUREMENTS

A. Introduction

At the outset of the present work, the energy level diagram of Ajzenberg-Selove and Lauritsen (1959) showed only eight excited levels of ^{9}Be below the ^{7}Li + d threshold. The small number of such levels allows a brief level-by-level summary of some of the experimental information on their properties:

(1)   The ground state is known to have spin 3/2 from the quadrupole splitting of its magnetic resonance absorption line (Schuster and Pake, 1951).

(2)   The 1.7 MeV state has been assigned $1/2^+$ from analysis of the ^{9}Be(γ, n) reaction (Guth and Mullin, 1949). Its spectral shape has been adequately represented by Spencer et al., (1960), and by Barker and Treacy (1962). Both analyses assume that the state consists of a neutron in an s-wave orbit about ^{8}Be(g. s.) core, confirming the $1/2^+$ assignment.

(3)   The 2.43 MeV state has been assigned spin 5/2 from a direct interaction interpretation of inelastic scattering angular distributions (Summers-Gill, 1958; Ribe and Seagrave, 1958; Benveniste et al., 1956). This spin is supported, and an unambiguous negative parity assignment is made, on the basis of its excitation by E2 (Nguyen Ngoc et al., 1963) and M1 (Edge and Peterson, 1962) transitions from the ground state in ^{9}Be(e, e') scattering.

(4)   The 3.03 and 4.65 MeV levels are both assigned positive parity on the basis of their strong excitation in ^{9}Be(γ, n), both supposedly being electric dipole transitions (Jakobson, 1961). These assignments are supported by the absence of both levels in ^{9}Be(e, e') at 180$^\text{o}$ (Edge and Peterson, 1962), which excites negative parity levels by M1 transitions. The anisotropic ^{9}Be(γ, n) neutron angular distribution from the 3.03 MeV level is consistent with d-wave neutron emission, supporting 3/2$^+$ or 5/2$^+$ for this level (Jakobson, 1961). This assignment agrees with the analysis of Spencer et al. (1960).

(5)   The 6.76 MeV level is interpreted as the third member of the ground state rotational band, having as such spin and parity 7/2$^-$. (Benveniste et al., 1956; Blair and Henley, 1959; Kunz, 1960). This interpretation is based on its strong excitation in inelastic scattering experiments (Summers-Gill, 1958; Ribe and Seagrave, 1958; Benveniste et al., 1956; Schrank et al., 1962), which should favor transitions within a band. Pinkston (1959) has shown that the inelastic scattering results can also be explained using the shell model for ^{9}Be, the 6.76 MeV level remaining 7/2$^-$. The interpretation of this level as a member of a ground-state-based rotational band is supported by the observation of this level in ^{9}Be(e, e'), where it was found to be strongly excited by an E2 transition from the ground state (Nguyen Ngoc et al., 1963).

(6)   Levels at 7.94 and 11.3 MeV have been reported in ^{9}Be(p, p') (Benveniste et al., 1956; Hasselgren et al., 1965; Britten, 1952). No spin and parity assignments have been hazarded.

(7) A level at 9.1 MeV has been only tentatively reported in ^{7}Li(^{3}He, p)^{9}Be (Almqvist et al., 1955), and has failed to appear in other reactions.

The first T = 3/2 level has been found at 14.392 MeV (Lynch et al., 1965), and has been identified by its extremely narrow width, $\Gamma = 0.8 \pm 0.3$ keV (Griffiths, 1965), which it owes to the absence of T-allowed particle decay channels. Its spin and parity are 3/2$^-$ according to the shell model, an assignment consistent with the observation of its M1 excitation from the ground state in inelastic electron scattering (Edge and Peterson, 1962), and with its strong electromagnetic decay to both the 2.43 MeV state and the ground state, supposedly also by M1 (Griffiths, 1965).

The reaction ^{7}Li(^{3}He, p)^{9}Be has previously been used primarily to study low excitations in ^{9}Be. Population of the ever-present 1.7, 2.43 and 3.03 MeV levels has been reported (Almqvist et al., 1955; Moak et al., 1958; Careaga and Mazari, 1963). In addition, Almqvist et al. (1955) and Moak et al. (1958) report a broad level at approximately 4.8 MeV. At higher excitations, Lynch et al. (1965) have used this reaction to populate the first T = 3/2 level in ^{9}Be. This section of the thesis presents the results of a survey of the entire excitation region in ^{9}Be below the ^{7}Li + d threshold.

B. Experimental Apparatus

(1) Beam

A doubly charged ^{3}He beam of energy ranging from 6 to 12 MeV was provided by the Caltech-ONR Tandem Van de Graaff

accelerator. The beam energy was determined by a 90° magnetic analyzer to a precision of approximately 20 keV. A typical beam spot was a 2 mm square, to which currents ranging from 0.1 to 0.3 μa were delivered. The beam charge was measured by an Eldorado model CI-110 current integrator.

(2) Proton Detection

^{3}He on ^{7}Li can give rise to a host of charged particles through such reactions as:

$$^7\text{Li}(^3\text{He, p})^9\text{Be}$$

$$^7\text{Li}(^3\text{He, d})^8\text{Be}$$

$$^7\text{Li}(^3\text{He, }\alpha)^6\text{Li}$$

$$^7\text{Li}(^3\text{He, t})^7\text{Be .}$$
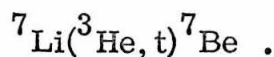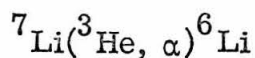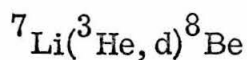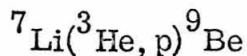
It was therefore important to be able clearly to distinguish protons from other types of particle. For a particle of mass number A, charge Z, and energy E, traveling a fixed orbit at a fixed field in a magnetic spectrometer,

$$E = \text{const.} \times \frac{Z^2}{A} .$$

Thus a magnetic analysis of particle momentum, together with an energy sensitive detector, provide an excellent means of particle identification. If any ambiguity remains, as in the case of doubly-charged alpha-particles and protons, thin foils placed over the

detector can utilize the differing energy loss rates of the various particles for further identification. A magnetic analyzer has the additional advantage of higher resolution than that which is available with the best alternative particle detectors. This characteristic allows accurate Q-value and width measurements of narrow levels. In the present experiment it also allowed narrow contaminant lines from $^{12}C(^{3}He, p)^{14}N$ and $^{16}O(^{3}He, p)^{18}F$ to be resolved from broader ^{9}Be proton groups.

For these reasons, the singles proton spectra were taken using a 61-cm radius double-focusing magnetic spectrometer. The spectrometer target chamber has been described in detail by Groce (1963). The chamber is evacuated by an oil diffusion pump system with a liquid nitrogen cold trap located immediately below the target.

The detector at the focus of the magnet was a single surface barrier solid state detector for low resolution work ($p/\Delta p = 360$ was used). For higher resolution ($p/\Delta p = 720$), an array of sixteen such counters in the focal plane of the magnet was used, allowing simultaneous counting at sixteen different momenta. The details of this array are described by McNally (1966).

C. Targets

The targets were ^{7}Li metal (99.99%) evaporated onto commercially made nickel foils. The targets ranged in thickness from 1 to 20 x 10^{18} atoms/cm^{2} (energy loss 4 to 80 keV for a 10 MeV ^{3}He); the nickel foils, from 500 to 5000 Å (energy loss 11 to 110 keV for a 10 MeV ^{3}He). Since lithium nitrides and oxidizes

on contact with the atmosphere, it was necessary to evaporate the target under vacuum in the spectrometer target chamber. The chamber is equipped with an arrangement whereby the nickel foils can be lowered into the furnace area for evaporation and subsequently raised to the beam level for bombardment. Hand formed boats of 0.08 mm tantalum were loaded with cubes of lithium approximately 2 mm on an edge. The boat temperature was initially raised high enough to melt the shell of hydroxide and nitride which had formed during the loading of the boat, and to evaporate a visible amount of lithium onto the chamber walls. The boat temperature was then lowered for the actual target evaporation. For a given boat, it was found possible to reproduce target deposition rates within about 50 percent by noting the current through the boat. Targets were initially made somewhat thinner than desired, the yield from the lithium measured, and subsequent layers evaporated as necessary.

The high vapor pressure of lithium at low temperatures, relative to that of, for example, Ni and Li_2O, makes evaporation of the target by heating from the beam a problem. At the low target temperatures required most of the energy deposited by the beam is conducted to the target rod through the nickel backing and lithium layer. Since the ratio of energy loss rate to thermal conductivity for lithium is much lower than that for nickel, a high ratio of lithium to nickel favors a lower target temperature. Thin nickel backings were therefore used for thin lithium targets. Frequent runs at checkpoints on the proton spectra were made to ensure the stability of the target. For a 10 MeV doubly-charged

^{3}He beam and 10^{19} atoms/cm^2 lithium on 5000 Å nickel, no
deterioration was noticed at beam currents less than 0.3 μa.

D. Contaminant Problem

A major experimental problem was the buildup of carbon
and, to a much lesser extent, oxygen, on the target surfaces.
Since the momentum range covered by the array is only 1/26 of
momentum at the center counter, it was necessary, with both the
array and the single counter, to scan the proton spectrum in
several steps to cover a region of interest. This process inevitably
allowed proton groups from ^{12}C(^{3}He, p)^{14}N and ^{16}O(^{3}He, p)^{18}F
time to grow.

The oxygen was found to build up only on the surface of
the lithium layer. Runs on oxidized nickel targets were taken and
normalized to the obvious contaminant peaks in the lithium spectra.
The oxygen content in a freshly evaporated lithium target was found
to be sufficiently small that the proton groups from ^{18}F did not
significantly interfere with the ^{9}Be groups. The growth rate was
low enough to allow several hours running on the same target before
^{16}O became a problem.

The carbon, presumably cracked by the beam onto the
target from organic vapors from sources such as diffusion-pump
oil and O-ring grease, was deposited on both the lithium layer and
the back side of the nickel foil at rates approximately equal and
proportional to the beam current. At an ambient pressure of 10^{-6}
mm of mercury, this rate was found to be approximately 1.6×10^{12}
atoms of carbon per micro-coulomb of doubly-charged ^{3}He.

For completeness, it should be mentioned here that runs on an oxidized lithium target carried out on the Kellogg 3MV Van de Graaff accelerator also showed a carbon deposition rate proportional to the beam current. The target chamber was very similar to that used for the tandem work, with a major addition being a cylindrical cold trap extension, of 2 cm inner diameter, which surrounded the target. The target chamber and a cold trap extension very similar to the one used here are described by Cusson (1965). The target in this case was made by evaporating a layer of approximately 0.5×10^{18} atoms/cm^2 of lithium onto a 0.05 mm tantalum blank and exposing it to moist air for ten minutes. At an ambient pressure of 10^{-6} mm of mercury, a 0.5 μa beam of 900 keV ^{3}He was found to deposit approximately 5.5×10^{12} carbon atoms per micro-coulomb of singly charged ^{3}He on the target.

The hydrogen content in the lithium metal targets, in evidence for example in fig. 6, was also found to grow in time.

Two procedures were followed to minimize the contaminant problem:

First, runs on a carbon foil were made to locate the size and relative intensities of ^{14}N lines. Points at expected locations of these lines were then taken immediately following evaporation of the lithium target before contaminants had time to grow. The remaining spectrum was then scanned at comparative leisure. This procedure is illustrated in fig. 4.

Second, the beam energy and proton angle were chosen in a way such that the contaminant groups appeared in as favorable locations as possible with respect to the ^{9}Be states. In order both to avoid crippling contamination and to find spectra in which the

[9]Be groups stood out clearly above the continuum, it was necessary
to tailor the proton angle and beam energy   selectively to each
region of excitation in [9]Be being studied.

E.   Results

(1)   Below 10 MeV in [9]Be

The region below 10 MeV was surveyed at three
combinations of energy and angle (figs. 1 - 3).   In agreement
with previous studies of this reaction, proton groups appear from
states at 0, 1.7, 2.43, 3.03 and 4.6 MeV.   In addition, the 6.76
MeV level is populated strongly in the two spectra taken at 90°.
The 9.1 MeV state tentatively reported by Almqvist, et al. (1955),
is not in evidence.   The extraction of widths for the broad 4.6 and
6.76 MeV levels is inherently inaccurate due to the uncertainty in
subtracting the background.   Using only the criterion that the back-
ground be smooth and "reasonable", upper and lower limits were
placed on the widths for these states, and are given in table I.   The
coincidence work later provided better spectra from which to
extract both of these widths (see pages 34 and 42).

(2)   11.29 and 11.81 MeV States

The region of excitation in [9]Be around 11.5 MeV
revealed two overlapping levels (fig. 4).   It was felt that the
difficulty both of establishing that the qualitative interpretation
of the proton spectra in this region was correct and of extracting
the widths and excitations for the levels warranted a more detailed
analysis than was given the region below 10 MeV.   Consequently

the magnet spectra obtained for this region at three combinations of angle and bombarding energy were converted to excitation spectra (see appendix A for procedure) and a two-level fit to the data was made.

The shape of the spectrum in this excitation region was assumed to have the form of two non-interfering Breit-Wigner resonances superimposed on a linear background:

$$Y(E) = A/[(E-E_{R1})^2 + \Gamma_1^2/4] + B/[(E-E_{R2})^2 + \Gamma_2^2/4] + C + D \times E$$

$$(13, 1)$$

where C and D paramaterize the background. An eight-parameter non-linear least-squares fit was made to the data, allowing A, B, C, D, E_{R1}, Γ_1, E_{R2} and Γ_2 to vary in each spectrum. The minimization of chi-squared was done on the CIT-IBM 7094 computer by the familiar technique of numerically calculating the eight-dimensional gradient of chi-squared, then stepping along this gradient toward decreasing chi-squared until a minimum is reached. For each spectrum several sets of initial trial parameters were used to ensure that the minimum finally reached was not a sensitive function of the starting point. Spectra taken at $[E(^3He) = 10$ MeV, $\theta_p = 1.7^\circ]$, $[E(^3He) = 10$ MeV, $\theta_p = 60^\circ]$ and $[E(^3He) = 7$ MeV, $\theta_p = 10^\circ]$ were fitted in this manner. Corresponding values of the resonance energies and widths are summarized in table I. Fig. 5 shows two of the fits so obtained.

(3) 13.78 MeV State

The excitation region between 12 and 15 MeV revealed a previously unreported level at 13.78 MeV with a width of 590 keV.

Two clean spectra of this level were obtained from runs on thick, freshly evaporated ^{7}Li targets, one of which is shown in fig. 6. The group also appeared in eight other spectra, but in most of these the presence of contaminant lines made the reliable extraction of excitation and width impossible.

(4) 16.671 MeV State

Fig. 7 is a magnet spectrum showing a previously unreported ^{9}Be level at 16.670 MeV. The experimental resolution for this spectrum was calculated to be 18 keV (FWHM) proton energy, being composed of 8 keV from the spectrometer resolution, 15 keV kinematic broadening and approximately 6 keV from target thickness and beam resolution. The experimental width of the curve in fig. 7 is 55 keV. After extracting the finite experimental resolution, the natural line width is left as 52 keV, corresponding to a ^{9}Be center-of-mass width of 40 keV. A similar analysis on a spectrum taken at 10 degrees, also with 18 keV experimental resolution, gave a center-of-mass width of 42 keV. Taking into account the errors involved in the background subtraction, and in determination of the half-width of the proton group, we adopt an average width of 41 ± 4 keV for this level. The resolution functions at both angles were checked using the proton group from the 14.392 MeV level in ^{9}Be, which is known to have an intrinsic width of (.8 ± .3) keV (Griffiths, 1965).

For Q-value measurements, the energy of the ^{3}He beam at the target center was determined from the energy of the proton group from the 14.392 MeV ^{9}Be level [Q = (-3.192 ± .005) MeV]. The average Q-value found from four spectra (table I) was

$Q = (-5.472 \pm .008)$ MeV, corresponding to an excitation in ^{9}Be of $16.671 \pm .008$ MeV.

(5) Peak Identification and Q-value Determination

Each level was observed at several angles and bombarding energies. In order to ensure that the observed protons were in fact coming from a mass 7 target, a chi-squared fit to the Q-value for each level was done assuming the target masses 6 and 9 as well as 7 (table I). The chi-squared for mass 7 is, in the worst case, a factor of fifteen lower than that for the better neighboring mass, eliminating the possibility that the observed groups came from target contaminants. The possibility that a group may come from some more complex mechanism than the population of a level in ^{9}Be, for example by a two-stage sequential decay, is unfortunately not excluded by the determination of the target mass. The behavior with changing bombarding energy of groups produced by two-stage mechanisms is quite different from that of ^{9}Be groups, however. Precautions were taken to vary both the beam energy and the proton angle in all cases.

The current version of the mass 9 isobar diagram is shown for convenience in fig. 35.

III. BRANCHING RATIO MEASUREMENTS

A. Outline of the Problem

^{9}Be has the unfortunate characteristic that the nucleus
to which it neutron-decays, ^{8}Be, is itself particle unstable. This
fact excludes the possibility of using this channel as an entrance
channel in measuring partial neutron widths from ^{9}Be excited
states. The situation is further complicated by the absence, below
the ^{7}Li + d threshold, of any two-body channels through which ^{9}Be
may be formed as a compound nucleus, with the exception of the
^{9}Be + γ channel. The measurement of the partial decay widths
to states in ^{8}Be thus requires the population of the ^{9}Be levels by
a more complicated reaction, and the measurement of the branching
ratios into the various outgoing channels. In the present experi-
ment, levels in ^{9}Be were populated in the ^{7}Li(^{3}He, p)^{9}Be reaction.
The neutrons emitted in the subsequent decay of the ^{9}Be levels
were detected in coincidence with the populating protons, and the
number of such coincidences was divided by the number of
populating protons to find the branching ratio.

The measurement of the energy and angle of the proton from
the first stage of the reaction, for a well defined bombarding energy,
determines kinematically the excitation and vector velocity of the
recoiling ^{9}Be nucleus. The subsequent emission of the neutron to
a sharp state in ^{8}Be will then result in a well defined neutron energy
at each laboratory angle. The energy of this decay neutron is the
signature of the level in ^{8}Be through which the decay is going.

Measurement of both neutron and proton energy is thus
necessary. In the present experiment, the proton energy was

obtained from a surface barrier solid state detector. Since the neutron is emitted promptly, typically within 10^{-21} sec of the proton, the time between the detection of the proton near the target and of the neutron some distance from the target, typically 10^{-8} sec, can be used to measure the velocity of the neutron. Thus a time-of-flight spectrum of the neutrons coincident with protons can be obtained.

The coincidence work historically was done in two separate parts, and accordingly will be described as two separate experiments with liberal references from one to the other. The first part, carried out on the Kellogg 3 MV Van de Graaff generator at a beam energy of 2.2 MeV, was concerned with measuring the neutron widths from ^{9}Be states at 3.03 MeV and 2.43 MeV. The second part consisted in measuring neutron widths from higher ^{9}Be levels at 4.65 MeV, 6.76 MeV, 11.29 MeV and 11.81 MeV and was done on the tandem at bombarding energies between 5 and 10 MeV.

B. 2.43 and 3.03 MeV Regions*

(1) Introduction

The major interest in this excitation region focused on the decay of the ^{9}Be (2.43 MeV) level to ^{8}Be (g.s.). Two-body channels open for this decay are (see fig. 36):

---

* Portions of this section have been taken from a paper by Christensen and Cocke (1967).

$$^9\text{Be (2.43 MeV)} \rightarrow {}^8\text{Be (g. s.)} + n \rightarrow 2\alpha + n \qquad (1)$$

$$\rightarrow {}^8\text{Be (2}^+) + n \rightarrow 2\alpha + n \qquad (2)$$

$$\rightarrow {}^5\text{He (g. s.)} + \alpha \rightarrow 2\alpha + n \qquad (3)$$

$$\rightarrow {}^9\text{Be (g. s.)} + \gamma \, . \qquad (4)$$

Since $\Gamma_{rad.}/\Gamma_{tot.} = (1.16 \pm .14) \times 10^{-4}$ (Purdom et. al.,1966), particle decay dominates. Channels (2) and (3) are available only through the tails of the broad $^8\text{Be}(2^+)$ and ^5He (g.s.). The spin and parity, $5/2^-$, of the ^9Be (2.43 MeV) level require that mode (1) proceed by f-wave neutron emission. Thus the size of the reduced width for this decay provides a direct measurement of the amount of f-wave configuration present in the wave function for this state.

The branching ratio of the 3.03 MeV level in ^9Be through (1) was originally measured for use in analyzing the ^9Be (2.43 MeV) decay. It soon became apparent, however, that this number was interesting in its own right. The single particle nature of this level served as partial motivation for extending the neutron decay measurements to higher excitations.

(2) Kinematics

The velocity diagram for the sequence $^7\text{Li}(^3\text{He, p})^9\text{Be}$ (2.43 MeV)(n)^8Be (g. s.), at a bombarding energy of 2.2 MeV, is shown in fig. 8. The proton, detected at a laboratory angle of 150°, leaves the ^9Be recoil travelling at 15.7° with respect to the beam axis. After travelling a mean distance of approximately 5×10^{-10} cm, the ^9Be nucleus breaks up, sometimes emitting a neutron to

the ground state of ^{8}Be at an angle $\theta_{c,n}$ with respect to the laboratory ^{9}Be velocity direction. The laboratory neutron velocity, $V_{L,n}$, is the vector sum of $V_{c,n}$, with respect to the ^{9}Be, and the laboratory velocity $V_{L,\,^9Be}$ of the ^{9}Be. Since the vector velocity of the ^{9}Be recoil has been defined by the proton detector, the final neutron energy is a unique function of laboratory neutron angle.

If the reaction proceeds by the emission first of an alpha-particle to ^{5}He (g. s.), then of a neutron by the ^{5}He, the resulting neutron spectrum will be a continuum. This result is due in part to the lack of definition of the ^{5}He recoil velocity, and in part to the range of excitation in the broad ^{5}He (g. s.) through which the reaction may go. The shape of the expected neutron time spectrum at $\theta_{L,n} = -15.7^O$ for the conditions used in the present experiment, calculated assuming isotropic angular distributions for both the alpha and neutron decays, is shown in fig. 9. (See appendix B for calculation.) The ^{8}Be (g. s.) neutrons appear at sufficiently high energy to be easily separated from this decay mode. Decay neutrons to the tail of the ^{8}Be (2^+) will also give a continuum, due to the breadth of ^{8}Be (2^+).

(3) Experimental Apparatus

(a) Targets

Targets of approximately 10^{18} ^{7}Li atoms/cm^2 in the form of ^{7}Li$_2$O were prepared by evaporating ^{7}Li (99. 99%) in vacuum onto 0. 025 cm tantalum backings and then exposing them to air for approximately twelve hours. Carbon contamination again loomed as potential problem, in this case the offending reaction

being $^{12}C(^{3}He, \alpha)^{11}C$. Annihilation radiation following the positron decay of ^{11}C caused a high counting rate in the plastic scintillator used for detecting the neutrons, thus contributing to the random coincidence rate. The oxidized targets had the advantage of stability at high enough beam currents (0.5 - 2.0 μa $^{3}He^{+}$) both to provide a good coincidence rate and to keep the target temperature at a level where carbon buildup was not important.

(b) Target Chamber

The target chamber used for the associated particle work is shown in fig. 10. The proton detector is located 3 cm from the target, and is movable over the angular range 150° to -150°. Neutrons leaving the target must pass through the .317 cm brass walls of the chamber en route to the neutron detector. For neutrons energies between 2 and 10 MeV, approximately 3 percent of the outgoing neutrons are inelastically scattered and 5 percent elastically scattered by the walls. When the yield from a monoenergetic neutron line is being measured, all neutrons whose energy has been changed sufficiently by scattering in the walls or whose flight path has been sufficiently lengthened by travel to the neutron detector via the walls to cause them to fall outside the experimental 2 ns time resolution are effectively removed. The inelastically scattered neutrons are immediately excluded. There is some chance that neutrons may be elastically scattered into the scintillator within the allowed 2 ns, after leaving the target at an angle other than the scintillator angle. The size of this effect depends in a complicated way on the neutron angular distribution, the kinematic change with angle of the neutron energy and the detailed geometry of the chamber. An estimate of its size,

assuming a spherical target chamber, isotropic neutron angular
distribution, isotropic scattering without energy loss from copper
and zinc nuclei in the walls and kinematics appropriate to
$^7Li(^3He, p)^9Be$ (2. 43 MeV) (n) ^8Be (g. s.) at $E(^3He)$ = 2. 2 MeV,
$\theta_{L, p}$ = 150°, $\theta_{L, n}$ = -15. 7° and d = 1 m, gives the result that
only 3 percent of the neutrons elastically scattered by the walls
will contribute to the observed neutron peak within the 2 ns
resolution. It was therefore assumed that the neutrons elastically
scattered by the brass walls were entirely removed. The observed
yields were correspondingly multiplied by a correction factor of
1. 08.

(c) Proton Detection

The protons were detected at 150° to the incident
beam in an 850 μ surface barrier detector. Aluminum foils of
0. 025 and 0. 23 mm thickness were placed over the counter to stop
the elastically scattered beam. The resolution of the proton counter,
limited in the case of the thicker foil by straggling, was
125 and 225 keV respectively for the two foils, for 8 MeV protons.
The thicker foil had the advantage of shifting the deuterons from
$^7Li(^3He, d)^8Be$ (g. s.) below the protons from $^7Li(^3He, p)^9Be$ (3. 03
MeV).

The timing signal from the proton counter was
derived from a commercially made ORTEC model 260 time-pickoff
circuit. This unit consists of an inductive pickoff followed by a
fast two-stage amplifier and a tunnel-diode discriminator. The
quiescent bias of the tunnel-diode may be adjusted externally,
allowing a variable setting of the triggering level on the counter

signal. The time slewing of the proton-counter-time-pickoff unit was such that lowering the triggering point on the counter signal from approximately 90 percent to 50 percent shifted the neutron time spectrum by 4 ns. The signal from the time pickoff was used to start an ORTEC model 263 time-to-height-converter (TTHC).

The linear signal from the counter was detected by a Tennelec model 100 A charge-sensitive pre-amplifier, and was followed by a Hamner model N-328 double-delay-line amplifier and single channel analyzer. The analyzer was used to select the region of interest from the proton spectrum. A sample spectrum from the proton detector is shown in fig. 11.

(d) Neutron Detection

The neutrons were detected at 60 to 100 cm from the target in either a (12.7 cm dia. × 5.08 cm thick) NE 102 or a (12.7 cm dia. × 1.91 cm thick) Naton 136 plastic scintillator, coupled to an XP-1040 phototube. The neutron counter could be rotated around the target in the plane defined by the beam axis and the proton detector. The scintillator was tilted with respect to the target scintillator axis at an angle such that the kinematic change in neutron energy over the finite angle subtended by the scintillator was compensated for by the change in flight path over this same angle.

A timing signal was derived from the zero-crossing of the 2 ns delay-line-clipped anode pulse. The zero-crossover pickoff was built after the circuit design of Brafman (1965). The signal from the pickoff was used to stop the TTHC. The best neutron time resolution observed was 1.2 ns (FWHM).

A slow linear signal was taken from the 13th dynode of the phototube, and was used to trigger a low-level discriminator. The signal from the TTHC was stored in a RIDL 400 channel analyzer when it was coincident with signals from the discriminator and from the proton detector single channel analyzer. A block diagram of the electronics is shown in fig. 12.

(e) Neutron Detector Efficiency

The efficiency of the neutron detector depends on the geometry and composition of the detector and on the setting of the low-level discriminator on the linear signal. The discriminator was set, using a ^{137}Cs source, to reject pulses of amplitude less than half-way down on the Compton edge from the 662 keV gamma-ray. The amplifier gain was then raised by a factor of eight before taking neutron spectra.

The relative efficiency of the thick (5.08 cm) scintillator was measured as a function of neutron energy with the CIT-ONR tandem pulsed-beam-time-of-flight system, using the reaction $^{3}T(p, n)^{3}He$. The discriminator cutoff was found to come at a neutron energy of .45 MeV. The theoretical expression for the efficiency (ϵ) is given by

$$\epsilon(E_n) = \frac{E_n - B}{E_n} \left(1 - e^{-\sigma_H N_H L}\right) \tag{23, 1}$$

where N_H is the number of hydrogen atoms/cm^3, σ_H the n-p scattering cross section, L the thickness of the scintillator and B the discriminator cutoff. This formula is derived neglecting

scattering from carbon atoms in the scintillator, and is found to
be adequate in the region of 6 MeV neutron energy (Swartz and
Owen, 1960; Rybakov and Sidorov, 1960). For Ne 102,
N_H = .0525 x 10^{24}/cm^3. With B = .45 MeV, E = 6.0 MeV,
σ_H = 1.45 barn and L = 5.08 cm, expression (23,1) gives
ϵ (6.0 MeV) = 0.295. The relative efficiency data were normalized
to this point. An absolute efficiency measurement made at
E_n = 6.23 MeV using the reaction D(d, n)^{3}He agreed within 10
percent with expression (23,1). Figure 13 shows both measured
and calculated values for ϵ as a function of E_n.

The efficiency of the thin scintillator (1.91 cm)
was measured relative to that of the thick scintillator. For neutron
energies between 1 and 2 MeV it was found that ϵ (thick) = 2.21 x ϵ
(thin).

Table III summarizes the neutron efficiencies
used in the calculations for each part of the experimental work.

(4) Experimental Procedure

The procedure followed was to record a time spectrum,
using the single channel analyzer on the protons to define the region
of interest in ^{9}Be. Figure 14 shows a time spectrum recorded with
the proton window accepting protons corresponding to excitation
energies in ^{9}Be between 2.2 MeV and 3.9 MeV. Figure 15 shows
the same spectrum converted to an energy spectrum. Before
converting the time spectrum the random coincidences, indicated
by the dashed line in fig. 14, were subtracted.

The neutron group from the ^{9}Be (2.43 MeV) to
^{9}Be (g. s.) stands out clearly. The group at E_n = 2.77 MeV is due

to the decay of ^{9}Be (3.03 MeV) to ^{8}Be (g. s.).   Neutrons below
E_n = 1.7 MeV are due mainly to decay modes (2) and (3).   The
background beneath the 2.43 MeV peak and the 3.03 MeV group
may be attributed to neutron decay from the continuous background
in the proton spectrum.

Since the tails of the ^{9}Be (3.03 MeV) and ^{9}Be (1.7 MeV)
states extend below the ^{9}Be (2.43 MeV) peak in the proton spectrum
(see fig. 11), a narrow window around the ^{9}Be (2.43 MeV) proton
group will always produce a peak in the time spectrum corre-
sponding to a ^{8}Be (g. s.) transition.   As the branching ratios to
^{8}Be (g. s.) from ^{9}Be (3.03 MeV) and ^{9}Be (1.7 MeV) are factors of
ten greater than that from ^{9}Be (2.43 MeV), this contribution may
be appreciable.

The proton window for fig. 14 and fig. 15 covered a
wide range of excitations in ^{9}Be.   The neutron group labeled 2.43
therefore cannot have been produced artificially by a narrow proton
window, but must come from a narrow state in ^{9}Be.   The corre-
sponding excitation energy in ^{9}Be calculated from the measured
flight time is 2.44 $\pm$ 0.05 MeV.

Because of counting rate and resolution problems at
lower neutron energies, it was found impractical to distinguish the
^{9}Be (2.43 MeV) neutrons by their flight time alone at all $\theta_{L,n}$.   The
procedure then followed was to set a narrow proton window around
the ^{9}Be (2.43 MeV) proton group and to correct the observed neutron
yield for the contribution from the ^{9}Be (3.03 MeV) state and the
^{9}Be (1.7 MeV) state.   A typical time spectrum obtained by this
procedure is shown in fig. 16B.   The region marked "p-window"
refers to ^{8}Be (g. s.) neutron energies corresponding to the region
of ^{9}Be accepted by the proton window.   The part of the spectrum

marked "3.03" indicates the neutron contribution from that part of the ^{9}Be (3.03 MeV) state falling inside the proton window.

To calculate the contributions to the ^{8}Be (g.s.) neutron group from the ^{9}Be (3.03 MeV) and ^{9}Be (1.7 MeV) states, the populations of these states relative to that of the ^{9}Be (2.43 MeV) state were needed. These were obtained by fitting the observed proton spectrum with appropriate "density of states" functions, as described by Barker and Treacy (1962), assuming $\ell = 2$ and $\ell = 0$ neutron decays to the ^{8}Be (g.s.) for the ^{9}Be (3.03 MeV) and ^{9}Be (1.7 MeV) states respectively. The resulting fits, after folding in the proton counter resolution function, are shown in fig. 11. The relative population of the three levels inside any proton window could then be calculated.

Using the measured yield of ^{8}Be (g.s.) neutrons from the 2.9 - 3.5 MeV region in ^{9}Be (see fig. 17), and assuming that these neutrons came entirely from the ^{9}Be (3.03 MeV) state, the contribution of this state to the ^{8}Be (g.s.) neutron group was calculated for the case where the proton window was narrowed around the ^{9}Be (2.43 MeV) protons. The size of this contribution to the ^{8}Be (g.s.) neutron peak was less than 20 percent of the total number of neutrons in the peak at all angles.

The ^{8}Be (g.s.) contribution from the ^{9}Be (1.7 MeV) state was calculated assuming a branching ratio of 100 percent and an isotropic center-of-mass angular distribution (s-wave neutrons). This contribution to the ^{8}Be (g.s.) neutron peak was never larger than a few percent of the total number of neutrons in the peak.

At $\theta_{L,n} = -15.7^O$ neutron yields obtained by this procedure agreed within statistical error with those obtained from spectra such as fig. 14.

(5) Results

The angular distribution of neutrons from the decay of ^{9}Be (2.9 - 3.5 MeV) to ^{8}Be (g. s.) was measured from $\theta_{c,n} = 0^O$ to $\theta_{c,n} = -80^O$. The result is shown in fig. 17. The vertical scale is the number of neutrons per steradian per 10^3 protons in the proton window, after converting from laboratory system to center-of-mass system, dividing by the neutron detector efficiency, and correcting for scattering in the backing and target chamber wall.

Figure 18 shows the angular distribution of neutrons for the decay of the ^{9}Be (2.43 MeV) state to ^{8}Be (g. s.) from $\theta_{c,n} = -90^O$ to $\theta_{c,n} = 80^O$. The vertical scale is neutrons per steradian per 10^3 protons leaving the ^{9}Be in its 2.43 MeV state.

To obtain the branching ratio for this decay mode, one should measure the neutron distribution over the entire sphere. Parity conservation requires that the angular distribution have even parity, so a measurement over any hemisphere is sufficient. There is in general no axis of symmetry, however.

The angular distribution of the neutrons from the ^{9}Be (2.43 MeV) state to the ^{8}Be (g. s.) is within the experimental errors symmetric about the ^{9}Be (2.43 MeV) recoil axis in the reaction plane. By assuming rotational symmetry about this axis, one finds that 7.5 ± 1.5 percent of the ^{9}Be (2.43 MeV) decays go by an $\ell = 3$ neutron to the ^{8}Be (g. s.).

Similarly, one gets that 61 ± 9 percent of the excitation region 2.9 MeV to 3.5 MeV decays to the ^{8}Be (g. s.). Only 70 ± 5 percent of the protons corresponding to this region leave the ^{9}Be in its 3.03 MeV state. Assuming that it is only the ^{9}Be (3.03 MeV) state which contributes to the ^{8}Be (g. s.) decay, one

finds that 87 ± 13 percent of the time this state decays by an $\ell = 2$ neutron to the ^{8}Be (g. s.).

It may be mentioned here that a number of previous measurements of the branching ratio for the 2.43 MeV state in ^{9}Be to ^{8}Be (g. s.) + n have been reported. Bodansky, Eccles and Halpern (1957) did the experiment ^{9}Be (α, α') ^{9}Be(2.43 MeV) (n)^{8}Be(g. s.)(α) ^{4}He, looking for the alpha particles in the breakup of ^{8}Be(g. s.). Their result was that less than 10 percent of the decay of the 2.43 MeV state in ^{9}Be goes by mode (1). A branching ratio of 12 ± 5 percent for the ground state has been reported by Marion, Levin and Cranberg (1959) from a study of the reaction ^{9}Be(n, 2n)^{8}Be. The lack of vector-momentum definition of the ^{9}Be(2.43 MeV) nucleus in this experiment, however, makes a unique interpretation of the data impossible. The neutron energies from the ^{9}Be(2.43 MeV) decay overlap considerably the energies of the neutrons from the initial population of this state. Mösner, Schmidt and Schintlmeister (1965) have reported a figure of 13 ± 5 percent for the branching ratio from a study of the reaction ^{12}C (n, α)^{9}Be(n)^{8}Be(g. s.)(α) ^{4}He. The interpretation of the data is again ambiguous, as recognized by the authors. In their experiment it was impossible to distinguish between ^{8}Be(g. s.) decays from the 2.43 MeV state in ^{9}Be and those from the tails of the 3.03 MeV state and the 1.7 MeV state.

C. Higher Excitation Regions

(1) Introduction

The primary interest in the ^{8}Be(g. s.) neutron width from the ^{9}Be(2.43 MeV) level was in the small f-wave components

of the wave function. The strong d-wave neutron decay from the
^{9}Be(3.03 MeV) level suggested that much information on the major
components of the wave functions of other ^{9}Be levels might be
available from the neutron decay widths. Consequently the experi-
ment was moved to the tandem accelerator where the greater beam
energy allowed the population of higher states in ^{9}Be. Neutron
decay from levels in ^{9}Be at 4.65, 6.76, 11.29 and 11.81 MeV
was studied. Since the stability of the ^{8}Be nucleus is not a
requirement with the associated particle technique, it was possible
to extract information on neutron decays to ^{8}Be(2^+) as well as to
^{8}Be(g.s.) from the 6.76, 11.29 and 11.81 levels in ^{9}Be. The
relevant decay energies are shown in fig. 36.

(2) Experimental Apparatus

The associated particle time of flight spectrometer
described in Section B was transferred as a whole to the tandem
and, with only a few exceptions, the techniques described above
were employed. Only the exceptions will be discussed below.

Doubly charged ^{3}He beams of 0.1 - 0.2 μa, of energy
ranging from 5 to 10 MeV, were provided by the tandem. It was
not possible to use ^{7}Li$_2$O targets at these beam energies, since
the ^{16}O(^{3}He, α)^{15}O reaction now proceeded much more strongly
than it had at low bombarding energies. Annihilation radiation
from the positron decay of the ^{15}O created a high counting rate
in the plastic scintillator, thus adding to the random rate. Con-
sequently, lithium metal targets of approximately 5×10^{18} atoms/
cm^2, enriched to 99.99% ^{7}Li, were evaporated onto 0.050 - 0.075
mm tantalum backings and transferred under vacuum to the target

chamber. The target transfer system is shown schematically in fig. 10.

The protons were detected in a 1000 μ surface barrier detector. For work at 0°, the ^{3}He beam was ranged out by the tantalum backing, while the protons passed through into the counter.

A Nuclear Data 4096 channel analyzer, operating in a two-dimensional mode, was used to record neutron flight time versus proton energy.

(3) Kinematics and General Features

In the measurement of the branching ratio to ^{8}Be(g. s.) from ^{9}Be(2. 43 MeV), one was dealing with a sharp state in ^{9}Be. At higher excitations in ^{9}Be the levels become broader, and lie on large backgrounds. To interpret the spectra in this region requires that one measure neutron time spectra over a wide range of proton energies. For this reason, a two-dimensional analysis of neutron flight time versus proton energy was made.

The discussion on pages 18 and 19 treats the kinematics for the reaction ^{7}Li + ^{3}He → ^{8}Be(g. s.) + n + p for the case where the reaction proceeds sequentially through a sharp state in ^{9}Be. At the higher excitation regions the breadth of the ^{9}Be levels and competition from other reaction mechanisms require that one adopt a view of the kinematics not restricted to sequential decays. If the total momentum and energy of a three-body final state are given, and if two of the particles are detected in coincidence at fixed angles, a measurement of the energy of one of the detected particles supplies enough information to determine the final vector momenta of all three particles, using only conservation of energy

and linear momentum. Thus a plot of the energy of one detected particle as a function of the energy of the other will result in a kinematic line. As an example, a plot of calculated proton energy versus neutron flight time for the process ^{7}Li + ^{3}He → ^{8}Be(g.s.) + n + p with E(^{3}He) = 10 MeV, $\theta_{L,p}$ = 90°, $\theta_{L,n}$ = 0° is shown in fig. 19. The kinematic line for the case where the ^{8}Be is left in its first excited state is also shown.

Since each point on a kinematic line corresponds to completely determined final momenta for the three particles, the excitations in systems comprised of any two of the particles are also determined. For example, in fig. 19 a point on either kinematic line specifies definite excitations in ^{9}Be, ^{9}B and d. An enhanced population along the line may appear whenever a resonant excitation in one of the above three nuclei is encountered. In the case where such a resonance is very strong, the process is said to proceed sequentially through the corresponding intermediate state.

In the present experiment interest was focused on those resonances for which the reaction proceeded through states in ^{9}Be. The excitation range in the n-p system was sufficiently high that no pronounced structure from this interaction was expected. The same could not be assumed in the case of ^{9}B, however. The reactions ^{7}Li(^{3}He, p)^{9}Be(n)^{8}Be and ^{7}Li(^{3}He, n)^{9}B(p)^{8}Be can both produce resonant groups along ^{8}Be(g.s.) and ^{8}Be(2^+) kinematic lines. Only by tracking such groups as the beam energy or detector angles are changed can the processes be distinguished. Fortunately, the relevant excitation region in ^{9}B showed sufficiently little structure that the ^{9}Be groups could be separated. Individual cases are discussed with the description of the analysis.

Figure 20 shows an oscilloscope display of the experimental data corresponding to fig. 19. A few general features of this spectrum are easily discernible, and are indicated on fig. 19:

1) The decay of the 2.43 MeV state in ^{9}Be to ^{5}He + α appears as a horizontal line. The proton energy from population of the state is fixed, while the two stage process ^{9}Be $\rightarrow$ ^{5}He + α $\rightarrow$ 2α + n produces a continuum of neutron energies.

2) The 3.03 MeV state in ^{9}Be is seen to decay strongly along the ^{8}Be(g. s.) line. The decay of ^{9}Be(4.65 MeV) to ^{8}Be(g. s.) appears as a considerably weaker but still easily discernible group.

3) The 6.76 MeV state in ^{9}Be is seen to decay strongly along the ^{8}Be(2^+) line. There is little, if any, sign of the decay of this state to ^{8}Be(g. s.).

If the proton from the population of a state is observed at an arbitrary laboratory angle, the differential decay probability for the associated neutrons must be measured over the whole sphere. When the proton is observed at 0°, however, the corresponding angular distribution of the decay neutrons must have axial symmetry about the beam axis. Furthermore, if the decay is from a single state in ^{9}Be with a well defined parity, the corresponding neutron angular distribution must have a positive parity. In the present experiment population protons from the 4.65 MeV, 11.29 MeV and 11.81 MeV states in ^{9}Be, were observed at 0° and the associated neutron angular distributions were measured only out to 90° in the ^{9}Be center-of-mass system.

(4) Experimental Procedure and Results

(a) 4.65 MeV State

Figure 21 shows a singles spectrum from the barrier counter taken at $\theta_{L,p} = 0^O$, $E(^3He) = 5.0$ MeV. The deuteron yield from $^7Li(^3He, d)^8Be(2^+)$ completely obscures the proton yield in the region around 4.65 MeV in ^9Be. For this reason a singles spectrum was taken with the magnetic spectrometer at the same angle and energy, separating protons from deuterons. The resulting proton spectrum is shown in fig. 22. The number of times the 4.65 MeV state in ^9Be was populated was derived from this data, using the proton yield to the 2.43 MeV state in ^9Be to normalize this spectrum to that from the solid state counter. The deuterons present no problem to the coincidence spectra, since they cannot be accompanied by neutrons.

Two-dimensional coincidence spectra were taken at thirteen neutron angles between $\theta_{L,n} = 0^O$ and 130°, for $\theta_{L,p} = 0^O$, $E(^3He) = 5.0$ MeV. The procedure followed to obtain the $^8Be(g.s.)$ neutron yield from the $^9Be(4.65$ MeV$)$ state was the following:

1) For each coincidence spectrum, time spectra from each proton channel were plotted. Fig. 23 shows an example of such a spectrum for a proton energy corresponding to 4.75 MeV in ^9Be.

2) The $^8Be(g.s.)$ yield was extracted from each spectrum and plotted as a function of proton channel number. Fig. 24 shows a sample of such a sum along the $^8Be(g.s.)$ line. The

decay of the 4.65 MeV state in ^{9}Be to ^{8}Be(g.s.) appears as a resonant group along this line.

3) The number of neutrons in this group was divided by the neutron detector efficiency, corrected for scattering in the chamber walls and target backing, divided by the number of populating protons and plotted as a function of neutron angle. The 0° yield from the ^{7}Li(^{3}He, d)^{8}Be(g.s.) was used to normalize the coincidence spectra to the singles spectrum.

The measurement of the yield from the ^{9}Be(4.65 MeV) level in both the singles and coincidence spectra depends on knowing the width and excitation of the level. This is especially important in the case of the singles spectrum where the size and shape of the assumed background depend sensitively on the width taken for the proton group. It was found that an excitation energy of 4.65 MeV and width of 900 keV provided consistent fits to both singles and coincidence spectra without requiring the assumption of unreasonable backgrounds. The resulting fits, taken to be of the form

$$Y(E) = (\text{const.})/[(E - E_R)^2 + \Gamma^2/4] \, , \qquad (34, 1)$$

are shown as solid lines in figs. 22 and 24. It was found that the branching ratio decreased by only 10 percent if the width used was increased to 1000 keV, as long as this width was used in fitting both the singles and the coincidence spectra.

To confirm that the group being observed in the coincidence spectrum came from ^{9}Be and not ^{9}B, plots were made of the excitation in ^{9}Be versus that in ^{9}B for the reaction

^{7}Li + ^{3}He ultimately proceeding to ^{8}Be(g. s.) + n + p. The relationship is given in fig. 25 for several values of $\theta_{L,n}$ for E(^{3}He) = 5 MeV, $\theta_{L,p}$ = 0°. The heavy dots are the experimental points, with their associated errors. The excitation of the ^{9}Be(4.65 MeV) group is seen to remain constant at $\theta_{c,n} \leq 90^O$. The deviation in excitation of this group from 4.65 MeV for $\theta_{c,n} \geq 90^O$ may be an indication of a contribution from a ^{9}B level at ~ 9.8 MeV. Since the excitation in ^{9}Be of the ^{9}Be(4.65 MeV) group appeared constant in the forward hemisphere, and there are no known levels between 9.7 and 11.6 MeV in ^{9}B, the region $0^O \leq \theta_{L,n} \leq 70^O$ was used for branching ratio measurements for this state.

The differential branching ratio of neutrons to ^{8}Be(g.s.) from the ^{9}Be(4.65 MeV) state is shown as a function of $\theta_{c,n}$ in fig. 26. Integration of this angular distribution gives a total branching ratio of (13 ± 4) percent.

(b) 11.29 and 11.81 MeV States

The 11.29 and 11.81 MeV levels were populated at E(^{3}He) = 10 and 9 MeV, $\theta_{L,p}$ = 0°. Seven coincidence spectra were taken in the region $0^O \leq \theta_{L,n} \leq 80^O$. The extraction of branching ratios to ^{8}Be from these states required the solution to several new problems:

1) Since these levels overlap considerably, (Γ(11.29 MeV) = 620 keV, Γ(11.81 MeV) = 400 keV), a detailed knowledge of the composition of the proton spectrum was necessary. Fig. 27 shows a solid state counter spectrum corresponding to this region of excitation, for E(^{3}He) = 10 MeV, $\theta_{L,p}$ = 0°. The

experimental resolution in this spectrum is approximately 380 keV, primarily due to the straggle of the protons through the target backing. The widths and relative intensities of the two levels from this reaction had been measured previously at the same bombarding energy and proton angle with a resolution of 50 keV, using a magnetic spectrometer (Fig. 5, page 13). The solid curve through the data points in fig. 27 is a fit to the experimental points of the form given in eq. (13, 1) . The parameters E_{R1}, Γ_1, E_{R2}, Γ_2 and $A/B \times \Gamma_2/\Gamma_1$ are consistent with the values used in the fit of fig. 5, after taking into account the poorer experimental resolution. A comparison of the parameters used in the two fits is made in table II. The background in the solid state counter spectrum is due to deuterons and to protons not stopped in the counter, as well as to the proton continuum. Some sign of ^{12}C, ^{16}O, and ^{1}H target contamination is seen.

2) The large energy release in the decay of these states to ^{8}Be produced much faster neutrons than did the lower lying ^{9}Be states. In order to resolve the $^{8}Be(g.s.)$ from the $^{8}Be(2^{+})$ the neutron counter had to be removed to a distance of about one meter. The corresponding reduction in solid angle, and thereby in counting rate, made it impractical to gather sufficient statistics to make a meaningful plot of either $^{8}Be(g.s.)$ or $^{8}Be(2^{+})$ sum <u>versus</u> proton energy, as was done for the 4. 65 MeV state. The alternate procedure adopted was to evaluate the sum at only four different proton energies. For each coincidence spectrum, time spectra were summed from four strips of the two dimensional spectrum, each strip having the same width along the proton energy axis. The locations of the strips were chosen in such a way that they represent

time spectra from excitations roughly centered at ^{9}Be(11.29 MeV; region III), ^{9}Be(11.81 MeV; region II), ^{9}Be(10.5 MeV; region IV) and ^{9}Be(12.5 MeV; region I). A sample of the raw data is shown in fig. 28 with the appropriate regions outlined; the regions are also indicated on the singles spectrum of fig. 27. Corresponding summed time spectra are shown in fig. 29.

By summing over the several proton channels, it was possible to obtain enough counts to make practical the extraction of the ^{8}Be(2$^+$) and ^{8}Be(g.s.) yields from each region. The variation in time of the ^{8}Be(g.s.) and ^{8}Be(2$^+$) neutrons across such a region, due to the change in excitation in ^{9}Be and to slewing in the proton timing, was approximately .8 ns, as compared to the experimental time resolution of about 2 ns.

Crudely speaking, time spectra from regions I and IV represent a background on which the decay from the 11.29 and 11.81 MeV levels, regions III and II respectively, is expected to lie. By linearly interpolating the behavior of this background between regions I and IV, the resonant behavior in regions II and III could be determined.

For quantitative extraction of the ^{8}Be(2$^+$) yields to ^{9}Be(11.29 MeV) and ^{9}Be(11.81 MeV), the ^{8}Be(2$^+$) neutron yield per proton channel as a function of proton energy was assumed to be of the form of eq. (13,1) at each $\theta_{L,n}$. For each coincidence spectrum, the four unknown parameters in this equation, A, B, C and D, were evaluated from the measured ^{8}Be(2$^+$) yields in the four regions. From the values of these parameters the number of ^{8}Be(2$^+$) neutrons in the 11.29 MeV and 11.81 MeV ^{9}Be groups could be calculated at each $\theta_{L,n}$. This procedure was

checked by extracting A, B, C and D in fig. 27 from the yields in the four regions. The values of these parameters so obtained agreed with those obtained from the curve fitting. A similar procedure was followed for the ^{8}Be(g.s.) neutrons.

The importance of including the background terms (C and D) of eq. (13,1) in the coincident neutron yields cannot be overemphasized, since by no means all of the ^{8}Be(2^+) neutron yield in regions II and III comes from ^{9}Be(11.81 MeV) and ^{9}Be(11.29 MeV) respectively.

3) The determination of the ^{8}Be(2^+) yield from each time spectrum required a knowledge of the shape of the neutron continuum. This continuum is supposedly due to decays through ^{8}Be(4^+) and through ^{5}He + α → 2α + n (see level scheme in fig. 36).

Fig. 30 shows a time spectrum from region II taken at $\theta_{L,n}$ = 30°. The dashed curve is a calculated shape assuming a decay through ^{8}Be(4^+). The solid line is a calculated spectrum assuming isotropic breakups through the ground state of ^{5}He. (See appendix B for calculations.) The representation of the observed neutron spectrum by the latter shape is sufficiently good to lead us to use this continuum shape consistently in the extraction of ^{8}Be(2^+) yields from all the spectra. The continua shown in fig. 29 are of this form, for example. The errors quoted in the final branching ratios are largely due to the uncertainty in this background shape.

The angular distributions of neutrons, divided by the neutron efficiency, corrected for scattering in the chamber wall, and converted to the ^{9}Be system, from the 11.29 MeV and

11. 81 MeV states in ^{9}Be to ^{8}Be(2^+) are shown in figs. 31 and 32. As no pronounced structure in the compound nucleus has been seen at E(^{3}He) in the vicinity of 10 MeV, the polarization of the ^{9}Be nucleus was not expected to change significantly when the bombarding energy was lowered from 10 to 9 MeV, and thus points from the two bombarding energies are included on the same graph. Since the kinematics for the sequential processes ^{7}Li(^{3}He, p)^{9}Be(n)^{8}Be and ^{7}Li(^{3}He, n)^{9}B(p)^{8}Be, vary quite differently as the bombarding energy is changed, the consistency of results at different bombarding energies provides a good check against any possible perturbing influence of decays from levels in ^{9}B.

The branching ratios obtained from the integrated angular distributions are: ^{9}Be(11. 81 MeV) to ^{8}Be(2^+), (12 ± 4) percent; ^{9}Be(11. 29 MeV) to ^{8}Be(2^+), (14 ± 4) percent. Only upper limits could be placed on the ^{8}Be(g. s.) decay: ^{9}Be(11. 81 MeV) to ^{8}Be(g. s.), ≤ 2 percent; ^{9}Be(11. 29 MeV) to ^{8}Be(g. s.), ≤ 3 percent.

(c) 6. 76 MeV Level

The extraction of the neutron decay probabilities for the 6. 76 MeV state of ^{9}Be was hindered by two major difficulties:

1) Since the state is quite broad, it is necessary to operate at a proton angle for which this group stands out strongly above the background in the singles spectra. Whereas the 4. 65, 11. 29 and 11. 81 MeV states were strongly populated at $\theta_{L, p} = 0°$, the 6. 76 MeV level was relatively weak at this angle, standing out strongly at $\theta_{L, p} = 90°$. This made it experimentally impossible to use the axial symmetry gained at $\theta_{L, p} = 0°$.

2) While the neutrons from the decay of the 6.76 MeV region to ^{8}Be(g. s.) were easily separable, those to the broad ^{8}Be(2^+) were difficult to separate from those coming from the ^{5}He + α decay. Accordingly, the analysis of the ^{8}Be(2^+) decay of the 6.76 MeV level in ^{9}Be was directed toward placing limits on the decay probability, rather than extracting a number for the branching ratio.

In fig. 33A is shown the result of projecting onto the proton energy axis the coincidence spectrum of fig. 20, excluding neutrons from the ^{8}Be(g. s.) line. This spectrum will contain neutrons from both ^{8}Be(2^+) and ^{5}He + α decays. The 6.76 MeV level in ^{9}Be stands out strongly above the background, an essential point in the interpretation of its decay spectrum. The neutron time spectrum corresponding to decay from a 600 keV wide region in ^{9}Be centered at an excitation of 6.8 MeV was taken to represent the decay from the ^{9}Be(6.76 MeV) level, the implicit assumption being that the background decay mode is the same as that for this level. Since the background at this point is less than 20 percent of the peak height, this assumption is not expected to introduce a large error into the results. Fig. 34A shows the 6.8 MeV decay spectrum from the coincidence spectrum of fig. 20, converted to a center-of-mass energy spectrum and divided by the neutron detector efficiency, plotted <u>versus</u> excitation in the α-α system. For the choice of $\theta_{L, p}$ and $\theta_{L, n}$ in this figure, the neutrons are being emitted at 0^0 with respect to the laboratory velocity of the recoiling ^{9}Be nucleus. Any attempt to extract a branching ratio from a measurement at a single neutron angle is dangerous, as is evident, for example, from fig. 18. Consequently

a 6.8 MeV decay spectrum taken at $\theta_{L,n} = 25^O$ is also shown (fig. 34B), corresponding to an angle of 79° in the ^{9}Be system for decays through the center of ^{8}Be(2^+). The angle is measured with respect to the laboratory direction of the ^{9}Be recoil. These spectra amount to a poor-man's two-point neutron angular distribution.

The solid curves represent the expected shape of the ^{8}Be(2^+) level, folded into the experimental resolution. These curves are taken to represent upper limits on the amount of ^{8}Be(2^+) decay at the two neutron angles. If a branching ratio in this case is taken, at each angle, to be the number of ^{8}Be(2^+) neutrons divided by the total number of neutrons, upper limits of 68 and 69 percent are found in figs. 34A and 34B respectively for the branching ratios of ^{9}Be(6.76 MeV) to ^{8}Be(2^+).

The lower limits for this decay mode are more difficult to deduce. The dashed curve in fig. 34A represents the spectral shape expected from neutrons from the ground state of ^{5}He for isotropic angular distributions of both the ^{5}He's and the neutrons from the subsequent ^{5}He decay. If an angular distribution of the ^{5}He's given by $W(\theta_{c,n}) = 1 + \cos^2\theta_{c,n}$ in the ^{9}Be system is taken, a somewhat better representation of the spectrum at high ^{8}Be excitations is obtained, although the general features of the spectrum are not drastically affected. Dash-dotted curves in figs. 34A and 34B represent spectral shapes at 0° and 90° in the ^{9}Be system, respectively, using this ^{5}He angular distribution. The height of these curves under the ^{8}Be(2^+) peak has been taken to represent the maximum contribution from ^{5}He decay to this peak. The corresponding lower limits on the ^{9}Be(6.76 MeV) decay to ^{8}Be(2^+) are 41 and 44 percent for figs. 34A and 34B respectively.

Fig. 33B shows the ^{8}Be(g. s.) yield from the spectrum of fig. 20, plotted versus proton energy. No resonant effect is seen at 6.76 MeV. The corresponding upper limit on the branching ratio of ^{9}Be(6.76 MeV) to ^{8}Be(2^+) is 2 percent.

The width of the ^{9}Be(6.76 MeV) level, taken from fig. 33A, is $\Gamma = 2.3 \pm .4$ MeV. A similar spectrum taken at $\theta_{L,n} = 0^O$ gave $\Gamma = 2.2 \pm .5$ MeV. The width used in calculating the partial neutron widths is $\Gamma = 2.3 \pm .4$ MeV.

IV. CALCULATION OF REDUCED WIDTHS:

In order to compare our experimental results with nuclear model predictions it is convenient to extract from our data the reduced widths for single neutron emission from the ^{9}Be states under investigation. Following the R-matrix formalism, the line shape of a ^{9}Be state is assumed to have a "generalized density of states" function (Barker, 1962) of the form

$$\rho(E) = \text{const.} \times \Gamma_T(E) / [(E - E_R - \Delta)^2 + (\Gamma_T^2(E)/2)^2] \qquad (43,1)$$

where

$$\Gamma_\ell(E) = 2kRP_\ell(kR)\gamma_\ell^2$$

$$\Gamma_T(E) = \sum_\ell \Gamma_\ell(E)$$

$$\Delta(E) = -\sum_\ell S_\ell(kR)\gamma_\ell^2$$

$$k = \text{center-of-mass wave number}$$

$$R = \text{channel radius}$$

$$P_\ell(\rho) = 1/F_\ell^2(\rho) + G_\ell^2(\rho), \text{ where } F_\ell \text{ and } G_\ell$$

are the regular and irregular coulomb wave functions, respectively

$$S_\ell(\rho) = \rho \frac{P_\ell(\rho)}{2} \frac{\partial}{\partial \rho} \left(\frac{1}{P_\ell(\rho)} \right)$$

$$\gamma_\ell^2 = \text{Reduced width in channel denoted by } \ell.$$

If Δ is assumed to have a linear variation with E across the resonance, this expression can be written (Thomas, 1951)

$$\rho(E) = \text{const.} \times \Gamma_{TO}(E) / [(E - E_{R'})^2 + (\Gamma_{TO}(E)/2^2]$$

where

$$\Gamma_{TO}(E) = \Gamma_T \times [1 + \sum_{\ell} \gamma_{\ell}^2 \, \partial S_{\ell}/\partial E]^{-1}_{E=E_{R'}} \qquad (44,1)$$

$$E_{R'} = E_R + \Delta(E_R) \ .$$

Although Γ_{TO} itself is a function of energy, due to the dependence of Γ_T on energy, a good representation of the curve shape is obtained by taking Γ_{TO} to be a constant, and to have the value which it has at $E = E_{R'}$. Let

$$\overline{\Gamma}_{TO} = \Gamma_{TO}(E_{R'})$$

$$\overline{\Gamma}_T = \Gamma_T(E_{R'})$$

$$\overline{\Gamma}_{\ell} = \Gamma_{\ell}(E_{R'}) \ .$$

The line shape is then given by

$$\rho(E) = \text{const.} \times \overline{\Gamma}_{TO} / [(E - E_{R'})^2 + (\overline{\Gamma}_{TO}/2)^2] \ . \qquad (44,2)$$

$\overline{\Gamma}_{TO}$ was obtained for each level by fitting the observed [9]Be line shape to expression (44, 2). $\overline{\Gamma}_{T}$ was then obtained using expression (44, 1). Since the evaluation of (44, 1) involves knowledge of γ_{ℓ}^{2}, an iterative procedure was used. Table IV shows values of $\overline{\Gamma}_{T}$ and $\overline{\Gamma}_{TO}$ so obtained. The 3.03 MeV level shows the greatest difference between $\overline{\Gamma}_{T}$ and $\overline{\Gamma}_{TO}$. The 6.76 MeV level has been taken to decay entirely through the channels (2) and (3) (see page 18). No shift function correction has been made for the levels at 11.29 and 11.81 MeV.

Although the branching ratios from a broad level through various decay channels vary, in principle, with excitation within the level, the approximation has been made here that

$$(B. R.)_{\ell} = \overline{\Gamma}_{\ell} / \overline{\Gamma}_{T} \ .$$

Reduced widths, expressed in units of $\hbar^{2}/mR^{2}$, are then given by

$$\theta_{\ell}^{2} = \overline{\Gamma}_{T} \times (B. R.)_{\ell} \times [\, 2kRP_{\ell}(kR)\hbar^{2}/mR^{2}]^{-1} \ . \qquad (45, 1)$$

Table V shows the values of θ_{ℓ}^{2} so obtained. The reduced widths for [8]Be(2^{+}) decay from the 11.29 and 11.81 MeV states have been tabulated assuming both p- and f-wave emission, as discussed below.

V. DISCUSSION

A. Introduction

In this section we attempt to interpret our results in the light of current nuclear models. Our choice of model is directed not solely by the agreement which it affords with our results, but also by the availability of detailed theoretical calculations. The problem naturally divides itself into separate discussions of negative or normal parity states and positive or non-normal parity states. For the former, we compare our results with 1p-shell model calculations; for the latter, with calculations based on a single particle model which in some sense approximates a shell model with higher configurations. A discussion of the applications of the Nilsson model to ^{9}Be is reserved for separate consideration.

B. Non-normal Parity States and the Shell Model

Recent shell model calculations for the A = 9 system, using the $(1s)^4(1p)^5$ configuration, have been done by Barker (1966) and by Cohen and Kurath (1965). The level scheme of Barker, very similar to that of Cohen and Kurath, is shown in fig. 37. The corresponding wave functions are in most cases near the pure LS-coupled wave functions, and, accordingly, the levels in fig. 37 are labeled with the spectroscopic notations of their major LS components. The ^{9}Be ground state, 2.43 MeV state and 6.76 MeV state are taken to be the higher J components of the ^{22}P, ^{22}D and ^{22}F doublets, respectively. The lower J components of these doublets have not been seen experimentally.

Positive parity levels at excitations as high as 11 MeV are expected to be quite broad (see page 50). We accordingly choose to interpret the relatively narrow 11. 29 and 11. 81 MeV states in ^{9}Be as negative parity levels, and to include them in the present discussion.

The reduced widths for single nucleon emission by levels of A = 9 to states in A = 8 have been calculated by Barker (1966a), using his intermediate coupling shell model wave functions (Barker, 1966), and by Kurath (1966) using the wave functions of Cohen and Kurath (1965), and are shown in table VI. Since only 1p configurations are used in both sets of wave functions, only reduced widths for p-wave neutron emission are non-zero. The absolute values of calculated reduced widths depend sensitively on the radial wave functions for the emitted nucleons. As discussed by Lane (1960), it is difficult to calculate this wave function accurately enough for the widths derived from the calculation to be meaningful. Consequently theoretical reduced widths are generally normalized to an empirically determined single particle reduced width, θ^2_{sp}. Lane (1960) finds, from a survey of 1p-shell reduced widths, that a single particle value of $\theta^2_{sp} = .6$ gives an adequate fit to the experimental data. The values of θ^2_p given in the table were calculated using this value for θ^2_{sp}.

(1) 6. 76 MeV State

The spin and parity of this level, 7/2$^-$, forbid its decay to ^{8}Be(g. s.) except by f-wave neutron emission, and it is therefore not surprising that this decay mode was not observed. The upper limit $\theta^2_f \leq 6 \times 10^{-2}$ is greater than the positive result

of $\theta_f^2 = 2.1 \times 10^{-2}$ found for the 2.43 MeV level of ^{9}Be.

The calculated value of θ_p^2 to ^{8}Be(2^+), $\theta_p^2 = .126$ is somewhat smaller than the lower limit of $\theta_p^2 \leq .28$ found experimentally. There are several states predicted by the p-shell model in this excitation region which have never been seen experimentally. It is certainly not possible to rule out that the very broad 6.76 MeV level may contain contributions from more than one level.

(2) 11.29 and 11.81 MeV States

There are at least four theoretical candidates for these two experimental levels, namely the $[4,1]^{22}$G $7/2^-$ and $9/2^-$ levels, and the $[3,2]^{24}$P $1/2^-$ and $3/2^-$ levels. It is possible to get some feeling for what to expect from these levels by looking at these states in the LS-coupling limit. The first three levels in ^{8}Be have a $[4]$ symmetry in this scheme; only states in ^{9}Be of symmetry $[4,1]$ have non-zero parentage for a single nucleon coupled to these ^{8}Be levels. The $[3,2]$ levels would be expected to have zero reduced widths for the emission of neutrons to the first three levels in ^{8}Be in LS coupling.

Continuing in the LS-coupling limit, the doublet G, L = 4, levels cannot be formed by coupling a p-wave nucleon to ^{8}Be(g.s.) (L = 0) or ^{8}Be(2^+) (L = 2). Neutron decay to these levels is thus also forbidden. Decay to ^{8}Be(4^+) is not forbidden from these levels in the LS-coupling limit.

The calculated values in intermediate coupling (a/k = 2.25 ; see Barker, 1966) for θ_p^2 to ^{8}Be(g.s.) and ^{8}Be(2^+) are small for all four shell model states, as would be expected from the above discussion. The finite values for θ_p^2

come from small components of the wave functions which are mixed in as one departs from LS coupling. We conclude that the small observed reduced widths for the decay of ^{9}Be(11.29 MeV) and ^{9}Be(11.81 MeV) to ^{8}Be(g.s.) and ^{8}Be(2^+) are in general agreement with the expectations of the shell model. For any of the suggested assignments these decay modes are sampling only the minor components of the wave functions; consequently, we feel that it is not possible to make shell model assignments for the observed levels on the basis of our observations in these decay channels.

The $9/2^-$ level can decay to ^{8}Be(2^+) only by f-wave neutron emission, from conservation of spin and parity. The sizes of the reduced widths necessary to account for the observed branching ratios to ^{8}Be(2^+) are only $\theta_p^2 = 4.0 \times 10^{-2}$ and 1.8×10^{-2} for the 11.29 and 11.81 MeV levels respectively. In view of the observed f-wave reduced width of 2.1×10^{-2} found for the 2.43 MeV level, it is not possible to eliminate a $9/2^-$ spin assignment for either level on the basis of its non-zero branch to ^{8}Be(2^+).

C. Positive Parity Levels

In the shell model description, non-normal parity levels cannot be formed by a 1p-shell configuration, but require the excitation of at least one particle into a higher shell. The lowest energy configurations so formed are expected to be $(1s)^4 (1p)^{A-5}$ (2s), $(1s)^4(1p)^{A-5}(1d_{3/2}$ or $1d_{5/2})$ and $(1s)^3(1p)^{A-3}$. Lane (1960) has noted the computational difficulties of diagonalizing a Hamiltonian in the basis formed by the inclusion of all possible states belonging to these configurations, and has suggested that

a good approximation for the lowest lying non-normal parity states
of a nucleus A may be found by limiting the basis to states formed
from coupling a single $2s_{1/2}$, $1d_{3/2}$ or $1d_{5/2}$ particle to the lowest
states of the A-1 nucleus. In this way he was able to account with
some success for the low-lying non-normal parity states in many
of the 1p-shell nuclei.

Barker (1961) has made detailed calculations based on this
model for ^{9}Be and ^{13}C. In the ^{9}Be case, he uses a basis formed
by coupling 2s and 1d neutrons to ^{8}Be(g. s.) and ^{8}Be(2^+) cores.
He then diagonalizes a Hamiltonian of residual interactions, similar
to that used in intermediate coupling calculations, to find energy
eigenvalues and wave functions, and, from the latter, neutron decay
widths. The resultant level scheme is shown in fig. 37. Only
relative energies are given by the model, the absolute placement of
the scheme being adjusted to fit the 1.7 and 3.03 MeV levels. Since
all of the positive parity levels have strong single particle
character, they become quite broad as their excitations rise above
^{8}Be(g. s.) and ^{8}Be(2^+) decay channels. The three lowest, and
narrowest, levels of the model, at 1.7, 3.04 and 4.84 MeV, are
to be associated with the experimental 1.67, 3.03 and 4.65 MeV
states. Since Barker has tabulated partial neutron widths, it is
at this level that we make our comparisons in table VII. Reduced
widths are included for convenience. The s-wave single particle
character of the 1.67 MeV state is inferred from the success of
this structure in the analysis of the ^{9}Be(γ, n) reaction, and in
accounting for the spectral shape of the level (see page 4). The
strong d-wave single particle character of the 3.03 MeV level is
in agreement with the model, though the total widths are in
disagreement by almost a factor or two. The agreement of partial

neutron widths from ^{9}Be(4.65 MeV) to ^{8}Be(g.s.) is almost within the experimental error bars. It appears that Barker's model gives at least a qualitatively valid description of the positive parity levels in ^{9}Be.

D. Configuration Mixing and Nilsson Model

The most directly relevant part of this thesis to the question of whether ^{9}Be may be thought of as a deformed nucleus is the measurement of the f-wave neutron width of ^{9}Be(2.43 MeV) to ^{8}Be(g.s.). The eigenfunctions of a single nucleon in an axially deformed potential well are not eigenstates of the orbital angular momentum, but may be expressed as some linear combination of eigenfunctions with different values of orbital angular momentum. The most often used formalism for describing the motion of a single nucleon in an axially deformed potential well is that of Nilsson (1955). Kurath (1965) has used this formalism to predict configuration mixing in the case of ^{7}Li, taking a deformation sufficiently large to account for the observed value of the static quadrupole moment of the ^{7}Li ground state. His result is that the ground state wave function contains, in addition to a major component of approximately 80 percent $(1s)^4(1p)^3$ (in intensity), an admixture of approximately 4 percent of the $(1s)^4(1p)^2(1f)$ configuration, the remainder being comprised of the configurations $(1s)^4(1p)^2(2p)$ and $(1s)^3(1p)^3(2d)$. In view of the many successes of the $(1s)^4(1p)^{A-4}$ shell model, it is particularly gratifying to see that he was able to account for the quadrupole moment while maintaining such a large component of the normal shell model configuration.

Stephenson (1966) has used the Nilsson model to calculate the expected f-wave width to ^{8}Be(g.s.) from the 2.43 MeV state in ^{9}Be. A summary of the steps involved in this calculation follows.

Nilsson gives, for the Hamiltonian of a nucleon in an anisotropic harmonic oscillator potential with spin-orbit coupling,

$$H = \overset{o}{H}_o + H_\delta + C \, \overline{1} \cdot \overline{s} + D \, \overline{\ell}^2 \quad , \text{ where}$$

$$\overset{o}{H}_o = \frac{\hbar \omega_o}{2} [-\nabla_r^2 + r^2] \, , \text{ and } \overline{r} \text{ is related to the spatial}$$

coordinate $\overline{r}'$ by $x = \sqrt{M\omega_o/\hbar} \; x'$, etc.

M = the particle mass,

$$H_\delta = -\delta \hbar \omega_o \frac{4}{3} \sqrt{\frac{\pi}{5}} \; r^2 \, Y_{20}$$

δ = a parameter characterizing the deformation (δ = 0 corresponds to a spherical potential),

C = strength of spin orbit potnetial,

D = strength of term which depresses higher angular momentum states, to be adjusted to give the proper shell order.

$\hbar \omega_o$ = is the energy separation needed to reproduce the observed shell structure of nuclei. If the nucleus is required to have a constant volume under deformation, ω_o becomes a function of δ:

$$\omega_o(\delta) = \overset{o}{\omega}_o (1 - \frac{4}{3} \delta^2 - \frac{16}{27} \delta^3)^{-1/6} \quad .$$

The representation used by Nilsson in the main body of his paper is that in which $\overset{o}{H}_o$ is diagonal. The basis states are eigen-

states of $\bar{\ell}^2$, ℓ_z and s_z with eigenvalues $\ell(\ell + 1)$, Λ and Σ respectively, and are designated by $|N\ell\Lambda\Sigma\rangle$, where N is the number of oscillator quanta.

$$\overset{o}{H}_o \, |N\ell\Lambda\Sigma\rangle = (N + 3/2)\hbar\omega_o \, |N\ell\Lambda\Sigma\rangle \, .$$

The quantum number $\Omega = \Lambda + \Sigma$, the eigenvalue of projection on the symmetry axis of the total angular momentum, is conserved by H. The $\bar{1} \cdot \bar{s}$ term mixes states with different Λ and Σ, while H_δ has off-diagonal matrix elements between states differing in ℓ by 2, and between states differing in N by 2. Since shells separated by $\Delta N = 2$ differ in energy by $2\hbar\omega_o$, and matrix elements of H_δ are usually much smaller than $2\hbar\omega_o$, mixings between major shells were not considered by Nilsson. As shown by Nilsson in an appendix, however, if the spatial coordinates x, y and z in the functions obtained by diagonalizing H, neglecting $\Delta N = 2$ terms, are replaced by x', y' and z', where

$$x' = e^{\alpha}x \, ,$$

$$y' = e^{\alpha}y \, ,$$

$$z' = e^{-2\alpha} \, z \, ,$$

$$\alpha = \frac{1}{2} \, \ell n(1 + \epsilon/3) \text{ and}$$

$$\epsilon = \delta + \delta^2/6 + O(\delta^3)$$

the resulting deformed orbitals are much better approximations to the true wave functions of H, and, in particular, contain the effects of major shell mixing.

The Nilsson configuration for the ground state of ^{9}Be should consist of 4 particles in orbit #1(1s, $\Omega = 1/2$), 4 particles in orbit #3(1p, $\Omega = 1/2$) and 1 remaining particle in orbit #2(1p, $\Omega = 3/2$). The 2.43 MeV level should be the first member of a rotational band based on this state, having as such the same configuration. The wave function for orbit #2, although designated by the spectroscopic notation "p" above, has, when written in the deformed coordinate system, non-zero projections onto the spherical wave functions with principal quantum numbers higher by 2, namely the 2p and 1f orbits. The procedure followed by Stephenson was to explicitly evaluate the overlap between deformed orbital #2 and the spherical 1p, 2p and 1f orbits. Writing

$$| \,(\#2\text{ orbital})\rangle = C_{1p} \,|\, 1p \rangle + C_{1f} \,|\, 1f \rangle + C_{2p} \,|\, 2p \rangle \,,$$

his results are

$$C_{1p} = [\cos h^2(\alpha) \cos h^{1/2}(2\alpha)]^{-1} \qquad (54, 1a)$$

$$C_{1f} = \sqrt{\frac{2}{5}} \times [\tan h(2\alpha) + \tan h(\alpha)] \times C_{1p} \qquad (54, 1b)$$

$$C_{2p} = \sqrt{\frac{1}{10}} \times [\tan h(2\alpha) - 4\tan h(\alpha)] \times C_{1p} \,. \qquad (54, 1c)$$

A derivation of C_{1p} and C_{1f} is given in Appendix D(1).

An alternate procedure to using Nilsson's deformed representation is to calculate the size of major shell admixtures to the wave functions in the spherical representation using first order perturbation theory. This is done for Nilsson orbital #2 in Appendix D(2).

To complete the analysis, the reduced widths for single nucleon emission by f- and p-wave decays by the ^{9}Be(2.43 MeV; 5/2$^-$) and ^{9}Be(g.s.; 3/2$^-$) levels, respectively, to ^{8}Be(g.s.), are taken by Stephenson to be proportional to the squares of the expansion coefficients:

$$\frac{\theta_f^2}{\theta_p^2} = \left| \frac{C_{1f}}{C_{1p}} \right|^2 . \tag{55, 1}$$

The evaluation of the equilibrium value of δ for a given Nilsson configuration may be obtained by finding that value which minimizes the total energy of the configuration. Alternatively it may be found from an observed quadrupole moment or E2 transition rate. The latter method is perhaps to be desired, since it relates the deformation directly to a measurable property of the nucleus. Nilsson (1955) gives for the intrinsic quadrupole moment of a nucleus of charge Z, mass number A and a deformation characterized by δ:

$$Q_0 = .8 \times Z \times R_z^2 \times \delta(1 + \frac{2}{3}\delta) \tag{55, 2}$$

where

$$R_z \simeq 1.2 \times A^{1/3} \text{ fm} . \tag{55, 3}$$

Nguyen Ngoc et al. (1963) evaluate Q_0 from the observed E2 widths to ^{9}Be(g.s.) from ^{9}Be(2.43 MeV) and ^{9}Be(6.76 MeV), assuming collective transitions. Their value is

$$Q_0 = (.26 \pm .01) \ b \ .$$

Substituting this value for Q_0, $Z = 4$ and $A = 9$ into eqs. (55, 2)
and (55, 3), one finds

$$\delta \simeq .8 \ .$$

Evaluating Stephenson's expression (54, 1b) for $\delta = .8$ gives

$$\frac{C_{1f}}{C_{1p}} = .244 \ .$$

The value for θ_p^2 calculated for the ground state of ^{9}Be to
^{8}Be(g. s.) from the shell model wave function of Cohen and Kurath
is given in table VI as

$$\theta_p^2 = .348 \ .$$

If one inserts these values into expression (55, 1), the f-wave
reduced width is predicted to be

$$\theta_f^2 = 2.08 \times 10^{-2} \ ,$$

a value to be compared with that found experimentally,

$$\theta_f^2 = 2.1 \times 10^{-2} \ .$$

The proton decay from the ^{9}B(2.71 MeV) and ^{9}B(2.34 MeV) states to ^{8}Be(g.s.) has been measured by Wilkinson, Sample and Alburger (1965). These states are the analogs of the ^{9}Be(3.03 MeV) and ^{9}Be(2.43 MeV) states, respectively. Their results were that ^{9}B(2.71 MeV) goes almost entirely to ^{8}Be(g.s.), a result consistent with the branching ratio of (87 ± 13) percent for ^{9}Be(3.03 MeV) to ^{8}Be(g.s.) obtained in the present experiment; however, they found only an upper limit for the f-wave decay of ^{9}B(2.43 MeV):

$$\theta_f^2 \leq .5 \times 10^{-2} .$$

The sensitivity of the reduced width to the radius R for the ^{9}Be case is such that a 10 percent decrease of R changes θ_f^2 by a factor of 1.84, while a 10 percent increase of R changes θ_f^2 by a factor of .58. A 20 percent increase in R is therefore necessary to change the reduced width by a factor of four; it is furthermore very unlikely that the radius of ^{9}Be should be larger than the radius of ^{9}B where the coulomb repulsion is more important. The disagreement between the two experimental results is at present unresolved.

E. Conclusion

The ^{7}Li(^{3}He, p)^{9}Be reaction has been found to populate all known levels in ^{9}Be below the ^{7}Li + d threshold, with the exception of the 7.94 and 9.1 MeV levels, neither of which has been well established. Of those found here, the levels at 16.671, 13.78, 11.81 and possibly 11.29 MeV have not been seen previously. It

is interesting to notice that the widths of the 11.29 and 11.81 MeV levels in ^{9}Be are quite small (620 and 400 keV respectively) compared to the width of 2.3 MeV found for the 6.76 MeV state in ^{9}Be. This characteristic is due at least in part to the small reduced widths of the former states for neutron emission to ^{8}Be(g.s.) and ^{8}Be(2^+); however, their main decay must be attributed to neutron emission to ^{8}Be(4^+) or to alpha-channels, and it is the small widths in these channels which must be explained.

The neutron decay widths to ^{8}Be(g.s.) and ^{8}Be(2^+) from normal parity states in ^{9}Be have been found to be in fair agreement with shell model predictions. The expectation that states at high excitations in ^{9}Be have small parentages for low-lying states in ^{8}Be plus a neutron is fulfilled. Unfortunately it has not been possible to observe the decays of the ^{9}Be(11.29 MeV) and ^{9}Be(11.81 MeV) levels to ^{8}Be(4^+), since only the tail of this level is energetically available. Measurements of decays in the ^{8}Be(g.s.) and ^{8}Be(2^+) channels have provided details concerning the ^{9}Be states without producing needed information on their major constituents.

The observation of the large reduced width to ^{8}Be(g.s.) from the ^{9}Be(3.03 MeV) level supports the suggestion by Lane (1960) that the lowest non-normal parity states in ^{9}Be should be formed by promoting a single neutron into a 2s- or 1d-orbit and taking the eight remaining nucleons to form a ^{8}Be core in a low excitation. The extension of this idea by Barker (1961) into a more detailed model has provided satisfactory agreement also with the observed decay rate to ^{8}Be(g.s.) from the ^{9}Be(4.65 MeV) level. The success of this model is especially interesting in view of the very simple structure which it ascribes to the non-normal parity states in the 1p-shell.

Although large quadrupole moments and E2 widths strongly suggest such admixtures, the non-zero reduced width found for the ^{8}Be(2.43 MeV) decay to ^{8}Be(g.s.) provides the first direct evidence for f-wave mixing in the 1p-shell. The precise quantitative agreement of the measured value for θ_f^2 with that predicted by the simple Nilsson calculation, though pleasing, is almost certainly fortuitous. Uncertainty in the value of θ_p^2 used in the calculation, and of the channel radius chosen, to which the reduced width extracted from the observed branching ratio is very sensitive (p. 57), leave room for variation in both values. It can be said, however, that the value of θ_f^2 measured here appears to be accounted for by assuming a deformation of ^{9}Be consistent with observed E2 transition rates between rotational levels of the nucleus.

The disagreement of the value of θ_f^2 found here for the ^{9}Be(2.43 MeV) decay with the upper limit on θ_f^2 reported by Wilkinson et al. for the ^{9}B(2.34 MeV) decay is viewed as serious and indicates that further experimental work is needed.

APPENDIX A

Conversion of Magnetic Analyzer Spectrum to Excitation Spectrum

We adopt the conventional notation $m_1 + m_2 \rightarrow m_3 + m_4$ where m_1 is incident with energy E_1 upon the stationary target m_2, and m_3 is observed at a fixed laboratory angle θ_L. m_1, m_2 and m_3 have definite masses, and m_4, the residual nucleus, is left at an excitation E_x above its ground state. If m_3 is observed in a magnetic spectrometer, there is a one-to-one correspondence between the momentum of m_3, as measured by the spectrometer, and E_x. The conversion of the spectrometer spectrum to an excitation spectrum consists of two steps:

(1) The momentum axis must be re-labelled with the corresponding values of E_x.

(2) The number of counts at each momentum must be multiplied by the appropriate factor to convert it to counts per unit excitation interval.

Step (1) has been covered extensively in the literature (e. g. , see Brown et al. , 1951). Quantities which must be measured in order to calculate the excitation are E_3 (the energy of m_3), E_1 and θ_3. E_3 is related to the frequency of the nuclear magnetic resonance probe used to measure the magnetic field of the spectrometer by the expression

$$E_3 = kf^2 \times \frac{Z^2}{m_3/m_p} \times [1 - \frac{E_3}{2m_3c^2}]$$

where k is the calibration constant of the spectrometer, and m_p is the proton mass. k has been determined, using a Thorium-B alpha-source, to be .01139 MeV-$(MC)^{-2}$ (Groce, 1963). Corrections for the dependence of k on frequency (McNally, 1965) were made. The observation angle θ_3, was taken from the spectrometer track calibration made by Groce (1964). The energy of the incident beam at the center of the lithium layer was calculated from the observed position of the proton groups from either ^{9}Be(g. s.) (Q = 11.199 MeV) or from ^{9}Be(14.392 MeV) (Q = -3.192 ± .005 MeV). By this procedure effects of energy loss by the outgoing proton in the target (typically less than 10 keV) were implicitly taken into account. For the ^{9}Be(16.671 MeV) state, small corrections for the variation of this energy loss with outgoing proton energy were made.

Step (2) consists of two stages:

(a) Conversion of Spectrometer Spectrum to Laboratory Energy Spectrum

For a fixed magnetic field strength, the finite radial extent Δr of a counter at the spectrometer focus subtends a finite window ΔE in particle energy. For the 61 cm radius magnetic spectrometer, the relationship is (Groce, 1963):

$$\frac{\Delta E}{E} = \frac{2}{D} \frac{\Delta r}{r} \quad \text{where}$$

D = the dispersion of the magnet, approximately independent of field,

= 3.75,

r = the mean radius of the particle trajectory,

= 61 cm,

E = the mean particle energy.

To obtain an energy spectrum one must divide the number of counts ΔN at each field setting by the corresponding ΔE:

$$\frac{dN}{dE} = \frac{\Delta N}{E} \times \left(\frac{D}{2} \frac{r}{\Delta r} \right).$$

(b) Conversion of Laboratory Energy Spectrum to Excitation Spectrum

As shown by Williams (1961), it is true relativistically that

$$\frac{1}{p_L} \left(\frac{d^2 N}{dE_L d\Omega_L} \right) = \frac{1}{p_c} \left(\frac{d^2 N}{dE_c d\Omega_c} \right)$$

where

p_L = laboratory momentum of m_3

p_c = center-of-mass momentum of m_3

$\dfrac{d^2 N}{dE_L d\Omega_L}$ = laboratory energy spectrum of m_3

$\dfrac{d^2 N}{dE_c d\Omega_c}$ = center-of-mass energy spectrum of m_3 .

In the non-relativistic approximation, this expression gives

$$\frac{d^2N}{dE_c \, d\Omega_c} = \frac{d^2N}{dE_L \, d\Omega_L} \sqrt{\frac{E_L}{E_c}}$$

where E_L and E_c are related by

$$E_c = E_L + \frac{m_1 m_3}{(m_1 + m_2)^2} E_1 - (2 \cos\theta_L) \times \left[\frac{E_1 E_2 m_1 m_3}{(m_1 + m_2)^2} \right]^{1/2} .$$

From

$$E_x = \frac{m_1 E_1}{m_1 + m_2} + Q_0 - \frac{m_1 + m_2}{m_4} E_c ,$$

where Q_0 = Q-value to the ground state of m_4

E_x = excitation in m_4,

one finally obtains

$$\frac{d^2N}{dE_x \, d\Omega_c} = - \frac{d^2N}{dE_c \, d\Omega_c} \frac{m_4}{m_1 + m_2} .$$

APPENDIX B

Energy Spectra from a Two Stage Breakup

The particle decay of ^{9}Be levels below the ^{7}Li + d threshold ultimately results in the three particles $\alpha + \alpha + n$. In the foregoing analysis it has been assumed that the mechanism by which this decay occurs is well approximated by an incoherent superposition of two-stage decays in which the final state is dominated by either the $\alpha - \alpha$ interaction or the $\alpha - n$ interaction, referred to in the text as decays through ^{8}Be and through ^{5}He respectively. The calculation of neutron energy spectra used in the analysis is described below for the cases of dominant $\alpha - \alpha$ and $\alpha - n$ interaction.

Using the factored wave function representation, as discussed for example by Gillespie (1964), it is possible to write the transition probability for a three-body decay, in which the interaction between particles 1 and 2 dominates the final state, as the product of a term T_o, representing an unenhanced transition probability, with an enhancement factor F, representing the interaction between particles 1 and 2:

$$T = T_o \times F \ .$$

Following Barker (1962), we represent the enhancement factor by a "generalized density of states" function of the form

$$F = \rho(E) = \text{const.} \times \frac{\sin^2 \beta_\ell}{k_{12}R_{12}P_\ell(k_{12}R_{12})} \ ,$$

where

$$\beta_\ell \quad = \delta_\ell + \varphi_\ell(\rho),$$

δ_ℓ = ℓ-wave nuclear phase-shift parameterizing the (1, 2) interaction,

k_{12} = center-of-mass wave number in the (1)-(2) channel,

R_{12} = interaction radius of (1)-(2) channel,

$P_\ell(\rho) = 1/[\, F_\ell{}^2(\rho) + G_\ell{}^2(\ell)\,]$, where F_ℓ and G_ℓ are the regular and irregular coulomb wave functions, respectively,

$\varphi_\ell(\rho) = \arctan(F_\ell(\rho)/G_\ell(\rho))$.

We use for T_O

$$T_O = k_3 R_3 P\,(k_3 R_3)$$

where

k_3 = center-of-mass wave number in the (3)-(1, 2) channel,

R_3 = interaction radius of (3)-(1, 2) channel.

The factor $k_3 R_3$ is proportional to the density of final states of the (3)-(1, 2) system, while $P(k_3 R_3)$ takes into account the dependence of T_O on centrifugal and coulomb barriers in the (3)-(1, 2) channel.

(1) Neutron Energy Spectrum from Decays Through ^{8}Be

The center-of-mass neutron spectrum for the dominant $\alpha - \alpha$ interaction is given by

$$\frac{dN}{dE_n} (E_n) = \text{const.} \times [kRP_\ell (kR)]_{8_{Be-n}} \times [\frac{\sin^2 \beta_\ell}{kRP_\ell (kR)}]_{\alpha - \alpha}$$

where E_n is the center-of-mass neutron energy. This expression was used in calculating neutron line shapes for decays to ^{8}Be(2^+) (fig. 34) and ^{8}Be(4^+) (fig. 30). The parameters used were:

$\alpha - \alpha$ channel:

$$R_{\alpha - \alpha} = 4.0 \text{ fm}$$

$$\ell = 2 \text{ or } 4$$

n - ^{8}Be channel:

$$R_n = 4.35 \text{ fm}$$

$$\ell = 1 \quad .$$

The experimental $\alpha - \alpha$ phase shifts were used for δ_ℓ (Tombrello and Senhouse, 1963).

(2) Neutron Energy Spectrum from Decays Through ^{5}He(g. s.)

The neutron energy spectrum in this case owes its continuum shape both to the width of the ^{5}He(g. s.) and to the

emission of the neutron in the second stage of the decay. The shape of the spectrum depends on both the variation of the transition matrix element with the excitation of the ^{5}He produced in the first stage and the angular distributions of particles emitted in both stages.

The shape of the expected spectrum for a two-stage decay proceeding through a sharp intermediate state, for arbitrary angular distributions of both stages, is given in closed form by Morinigo (1963). We summarize only those results relevant to the analysis described in the text. For an angular distribution of the ^{5}He in the first stage given by

$$W(\theta) = 1 + \beta \cos^2 \theta$$

and an isotropic ^{5}He decay, the center-of-mass neutron energy spectrum is given by

$$\frac{dN}{dE_n} (E_n, E_x) = \frac{\text{const.}}{vw} \times [\, 1 + \frac{3b^2 + 4_{gc}}{8g^4} \beta \,]$$

where

$\quad$ v $\quad$ = velocity of ^{5}He after the first stage,

$\quad$ w $\quad$ = velocity of emitted neutron with respect to the ^{5}He,

$\quad$ g $\quad$ = resulting center-of-mass neutron velocity,

$\quad$ b $\quad$ = $\frac{gz}{v} (g^2 - w^2 + v^2)$,

$$c = w^2(1 - y_o^2) - g^2 z^2 \, ,$$

$$y_o = g^2 - v^2 - w^2/2vw \, ,$$

E_x = excitation in the $\alpha - n$ system. The velocities are implicit functions of E_x.

This expression is valid for

$$|v - w| \leq g \leq |v + w| \, ;$$

otherwise

$$\frac{dN}{dE_n} = 0 \, .$$

The transition probability for the process as a function of E_x is given by

$$\frac{dT}{dE_x} = \text{const.} \times [\, kRP_\ell(kR) \,]_{5_{He - \alpha}} \times F(E_x)_{\alpha - n} \, .$$

The enhancement factor F was approximated for the calculations by the expression

$$F(E_x)_{\alpha - n} = (E_x)^{3/2} / (\, (E_x - .7)^2 + .16)$$

where E_x is in MeV.

The parameters used in the $\alpha - {}^5\text{He}$ channel were:

$$R = 4.0 \quad \text{fm}$$

$$\ell = 2 \, .$$

The final neutron spectrum is obtained by integrating over E_x:

$$\frac{dN}{dE_n} (E_n) = \text{const.} \times \int_o^{E_{cm}} \frac{dN}{dE_n} (E_n, E_x) \frac{dT}{dE_x} \, dE_x \, ,$$

where E_{cm} is the total center-of-mass energy available to the $\alpha + \alpha + n$ system.

APPENDIX C

Branching Ratio Calculations

(1) Differential Branching Ratio

The differential branching ratio at a single neutron angle, expressed in the ^{9}Be center-of-mass system, is given by

$$\frac{dB}{d\Omega} (\theta_{c,n}) = \frac{N_n}{N_p} \times \frac{C}{\epsilon} \times \frac{1}{\Delta\Omega_L} \times \text{C. M. F.} \qquad (70,1)$$

where

N_n = Observed number of neutron counts through the decay mode of interest,

N_p = Corresponding number of populating protons,

C = Correction factor for neutron scattering in target backing and chamber walls,

ϵ = Neutron detector efficiency,

$\Delta\Omega_L$ = Laboratory solid angle subtended by neutron counter,

C. M. F. = Factor for converting the laboratory solid angle into the ^{9}Be center-of-mass system. Referring to the velocity diagram in fig. 8,

$$\text{C. M. F.} = [1 - x^2\sin^2\theta]^{1/2} [x\cos\theta + (1 - x^2\sin^2\theta)^{1/2}]^{-2} \quad (71, 1)$$

where

$$\theta = |\theta_{L,n} - \theta_{L,^9Be}| \quad \text{and}$$

$$X = V_{L,^9Be} / V_{c,n} \ .$$

As an example, the branching ratio from $^9Be(2.43 \text{ MeV})$ to $^8Be(g.s.)$, at $\theta_{c,n} = 0^\circ$, will be calculated below. The neutron time spectrum for this case is that shown in fig. 14.

N_n: The background under the $^8Be(g.s.)$ decay peak from the 2.43 MeV state in ^9Be was estimated by linear extrapolations of the low energy side of the group marked "3.03" and the high energy side of the decay from modes (2) and (3) (see page 24). Integration of the peak gives

$$N_n = 601 \text{ cts.} \quad .$$

N_p: The proton window for this run included excitations in ^9Be between 2.2 and 3.9 MeV. From a spectrum similar to that of fig. 11, it was calculated that 54 percent of the protons in this window populated the 2.43 MeV state in ^9Be. During the taking of the neutron spectrum in fig. 14, a scaler (fig. 12) recorded 15.47×10^6 counts in the proton window, giving the number of population protons as

$$N_p = 8.38 \times 10^6 \text{ cts.} \quad .$$

C: Approximately 2 percent of the neutrons are scattered passing through the .05 cm tantalum target backing. Taking this as the removal percentage and adding an 8 percent correction for removal by the chamber walls gives C = 1.10.

ϵ: The thin scintillator was used for this run. From table III,

$$\epsilon = .19 \quad .$$

$\Delta\Omega_L$: A 12.7 cm diameter scintillator at 100 cm from the target subtends a solid angle of

$$\Delta\Omega_L = 1.26 \times 10^{-2} \text{ ster.} \quad .$$

C.M.F.: Expression 71,1 above gives, for $|\theta_{L,n} - \theta_{L,{}^9Be}| = 0$, X = .702,

$$C.M.F. = .345 \quad .$$

Evaluation of expression (70,1) yields $\frac{dB}{d\Omega}(0^o) = 11.4 \times 10^{-3}$ neutrons per proton per steradian.

(2) Total Branching Ratio

In all cases axial symmetry about the laboratory ${}^9Be$ recoil direction and symmetry about 90° in the ${}^9Be$ center-of-mass system was assumed. Under these conditions, the total branching ratio is given by

$$B.R. = 4\pi \int_0^{\pi/2} \frac{dB}{d\Omega}(\theta_{c,n}) \sin\theta_{c,n} \, d\theta_{c,n} \quad .$$

APPENDIX D

Calculation of f-wave Components of Nilsson Orbital #2

(1) Deformed Representation:

For a spherical potential, Nilsson orbital #2 is given by the pure basis vector $|111+\rangle$, in the $|N\ell\Lambda\Sigma\rangle$ notation, where the $+$ signifies positive projection of the nucleon spin along the z-axis in the body coordinates. In Nilsson's spherical representation, neglecting major shell mixing, this basis vector remains an eigenstate even when the nucleus is deformed, since there are no other basis vectors in the same major shell with $\Omega \equiv \Lambda + \Sigma = 3/2$ which can be mixed in. To obtain the deformed Nilsson orbital which implicitly contains the effects of major shell mixing, one need only write the vector $|111+\rangle$ in the deformed coordinate system. Overlaps of this deformed wave function with spherical solutions can then be evaluated to find the coefficients in the expansion

$$| (\#2\ \text{orbital})\rangle = C_{1p} | 1p, m_\ell = 1\rangle + C_{1f} | 1f, m_\ell = 1\rangle + C_{2p}| 2p, m_\ell = 1\rangle .$$

The coefficients C_{1p} and C_{1f} are evaluated below.

In spherical coordinates, the properly normalized solutions for a particle in an isotropic harmonic oscillator potential well for 1p and 1f orbits, with $m_\ell = 1$, are

$$\psi_{1p,1} = [\ \frac{8}{3} \sqrt{\frac{\lambda^5}{\pi}}\ ]^{1/2}\ r\ e^{-\lambda r^2/2}\ Y_{11}(\theta,\varsigma)$$

$$\psi_{1f,1} = \left[\frac{32}{105} \sqrt{\frac{\lambda^9}{\pi}} \right]^{1/2} r^3 e^{-\lambda r^2/2} Y_{31}(\theta, \varsigma)$$

where $\lambda = m\omega/\hbar$. Spin functions are suppressed throughout this section.

In Cartesian coordinates,

$$\psi_{1p,1} = \left[\frac{\lambda^5}{\pi^3} \right]^{1/4} (x + iy) e^{-\lambda/2(x^2 + y^2 + z^2)}$$

$$\psi_{1f,1} = \left[\frac{\lambda^9}{100\,\pi^3} \right]^{1/4} (x+iy)(4z^2-x^2-y^2) e^{-\lambda/2(x^2+y^2+z^2)} .$$

The spatial wave function for Nilsson orbital #2 is obtained by making the substitutions (cf. p. 53)

$$x \rightarrow e^{\alpha} x = xT$$

$$x \rightarrow e^{\alpha} y = yT$$

$$z \rightarrow e^{-2\alpha} z = zL$$

into the above expression for $\psi_{1p,1}$, giving

$$\psi(\#2 \text{ orbital}) = \left[\frac{\lambda^5}{\pi^3} \right]^{1/4} T(x+iy) e^{-\lambda/2[(x^2+y^2)T^2 + z^2L^2]} .$$

Evaluating the overlaps,

$$
C_{1p} = [\frac{\lambda^5}{\pi^3}]^{1/2} \int_{-\infty}^{\infty} dx \int_{-\infty}^{\infty} dy \int_{-\infty}^{\infty} dz \left\{ (x-iy) e^{-\lambda/2[x^2+y^2+z^2]} \right.
$$

$$
\left. \times T(x+iy) e^{-\lambda/2[(x^2+y^2)T^2 + z^2L^2]} \right\} .
$$

Setting $\quad dxdy = \rho d\rho d\theta$ and $x^2 + y^2 = \rho^2$,

$$
C_{1p} = [\frac{\lambda^5}{\pi^3}]^{1/2} \int_{-\infty}^{\infty} dz\, e^{-\lambda/2[1+L^2]z^2} \times T \int_{o}^{2\pi} d\theta \int_{o}^{\infty} \rho d\rho\, \rho^2 e^{-\lambda/2\rho^2[1+T^2]}
$$

$$
= 4\sqrt{2}\, \frac{T}{(1 + L^2)^{1/2} (1 + T^2)^2} .
$$

The 1f overlap is evaluated in a similar way, giving

$$
C_{1f} = \frac{16}{\sqrt{5}} T [\frac{1}{(1 + L^2)^{3/2}(1 + T^2)^2} - \frac{1}{(1 + L^2)^{1/2}(1 + T^2)^3}] .
$$

The ratio C_{1f} to C_{1p} is then given by

$$
\frac{C_{1f}}{C_{1p}} = \sqrt{\frac{2}{5}} \times 2 [\frac{1}{(1 + L^2)} - \frac{1}{(1 + T^2)}]
$$

$$= \sqrt{\frac{2}{5}} \ [\tanh(2\alpha) + \tanh(\alpha)] \ .$$

(2) Perturbation theory:

The major shell mixings can also be calculated in first order perturbation theory using Nilsson's spherical representation. The total Nilsson Hamiltonian can be written as

$$H = H_1 + H_{\delta 1} + H_{\delta 2} \qquad \text{where,}$$

$$H_1 = \overset{o}{H}_o + C \ \bar{\ell} \cdot \bar{s} + D \ \bar{\ell}^2 \ .$$

Here we take $H_{\delta 1}$ to represent that part of H_δ which does not include matrix elements between major shells, and $H_{\delta 2}$ to represent only that part of H_δ which has matrix elements between major shells. Nilsson has diagonalized $H_1 + H_{\delta 1}$; the problem here is to evaluate the size of major shell mixing caused by $H_{\delta 2}$. The f-wave admixture into Nilsson orbit #2 is considered below.

The explicit form of H_δ is given by

$$H_\delta = -\delta \hbar \omega_o \ \frac{4}{3} \ \sqrt{\frac{\pi}{5}} \ r^2 \ Y_{20} \ .$$

The eccentricity ϵ of the deformed shape is related to δ by

$$\epsilon = \delta + \frac{1}{6} \ \delta^2 + O(\delta^3) \ .$$

The relative scales in the x- and z-directions are given by

$$\frac{z_o}{x_o} = \left(\frac{1 + \epsilon/3}{1 - 2\epsilon/3}\right)$$, where x_o and z_o are the distances along the x- and z-axes respectively to an equipotential surface. The shape is prolate for positive ϵ.

H_δ conserves the quantum numbers Λ and Σ, and connects states differing in N and ℓ by 2. In the major shell two quanta above the 1p shell there is only one basis vector with $\ell = 3$ which will be mixed into Nilsson orbit #2 by H_δ, namely the $|331+\rangle$ vector. In first order perturbation theory

$$|(\#2 \text{ orbital})\rangle = |111+\rangle + \frac{\langle 331+ | H_\delta | 111+\rangle}{2\hbar\omega_o} |331+\rangle + \text{---} .$$

Relevant matrix elements of r^2 and Y_{20} are given by Nilsson:

$$\langle N-2, \ell-2 | r^2 | N, \ell \rangle = (n+\ell+1/2)(n+\ell-1/2)$$

$$\langle \ell'\Lambda' | Y_{20} | \ell \Lambda \rangle = \sqrt{\frac{5}{4\pi}} \; \frac{2\ell+1}{2\ell'+1} \; \langle \ell 2 \Lambda 0 | \ell 2 \ell' \Lambda' \rangle$$

$$\times \; \langle \ell 2 0 0 | \ell 2 \ell' 0 \rangle$$

where $n = \frac{N - \ell}{2}$.

Evaluating the perturbation matrix element above gives

$$| (\#2 \text{ orbital}) \rangle \simeq |111+\rangle + \frac{\delta}{\sqrt{10}} |331+\rangle + \text{----} \quad .$$

This result may be compared with the results of section (1) for small values of δ:

$$\frac{C_{1f}}{C_{1p}} = \sqrt{\frac{2}{5}} \left[\tanh(2\alpha) + \tanh(\alpha) \right] \rightarrow \sqrt{\frac{2}{5}} \, 3\alpha \rightarrow \frac{\delta}{\sqrt{10}} \quad .$$

For a value of $\delta = .6$, the perturbation expression gives

$$\frac{C_{1f}}{C_{1p}} = .190 \quad ,$$

while the deformed representation expression gives

$$\frac{C_{1f}}{C_{1p}} = .188 \quad .$$

APPENDIX E

The ^{7}Li(^{3}He, α)^{6}Li Reaction

This section describes work done on the reaction ^{7}Li(^{3}He, α)^{6}Li. Its relationship to the main body of the thesis is technical only, the target and bombarding particle being the same as those used in the study of ^{9}Be. The incentive for this work was quite independent and will be reviewed briefly.

Of the various reactions which have been used to explore the level structure of ^{6}Li, the reaction ^{7}Li(^{3}He, α)^{6}Li has been one of the most prolific. In 1960 Allen et al. (1960) published an alpha-particle spectrum, taken at E(^{3}He) = .9 MeV, which showed levels in ^{6}Li at excitations of 0.0, 2.19, 3.56, 4.3, 5.35, 5.6, 6.63, 7.40, 8.37 and possibly 9.3 MeV. Alpha-deuteron scattering had previously revealed levels at excitations of 2.187 MeV (Lauritsen et al., 1953), 4.53 MeV and 5.4 MeV (Galonsky et al., 1955; Galonsky and McEllistrem, 1955); Day and Walker (1952) had found a γ-emitting state at 3.58 MeV. For the levels above 6 MeV, however, the spectrum of Allen et al. was the sole evidence. Linck et al. (1961) subsequently published an alpha-particle spectrum, taken at E(^{3}He) = 5 MeV, which had little in common with that of Allen et al., and which later proved to contain numerous spurious peaks. In 1963 Linck et al. (1963) published a revised version of the ^{7}Li(^{3}He, α)^{6}Li reaction, including several spectra at ^{3}He energies between 1 and 5 MeV. Their results were in general agreement with those of Allen et al., with one conspicuous difference: none of their spectra showed any levels above 6 MeV excitation. Groce and Whaling (1963) had similarly been unable to

observe the population of levels above 6 MeV in the reaction $^8Be(p, \alpha)^6Li$. Senhouse and Tombrello (1964) have found some indication of negative parity levels in this region in alpha-deuteron scattering, although they feel that more extensive measurements are necessary to establish the order and position of the levels.

The present work was undertaken to resolve the conflict between Allen et al. (1960) and Linck et al. (1963) with respect to levels in ^6Li above 6 MeV. Target preparation, beam handling and particle detection procedures were very similar to those described in the singles phase of the ^9Be work, (pp. 6-10), the only difference being the detection of alpha-particles instead of protons.

Alpha spectra have been taken at ^3He energies between .9 and 12 MeV. In none of these has any evidence of levels in ^6Li above 6 MeV appeared. At bombarding energies above 8 MeV alpha groups from sequential decays through ^8Be have been identified.

(1) Studies at Tandem Bombarding Energies

Targets of ^7Li metal ranging in thickness from 6 to 40×10^{18} atoms/cm^2 were evaporated in situ onto nickel backings, and were bombarded with ^3He beams of energies between 3.78 and 12 MeV, at typical currents of $0.2 \mu a$. The alpha particles were detected in surface barrier counters at the focus of the 61-cm radius magnetic spectrometer, using a foil arrangement to identify the particles.

(a) Spectra for $E(^3He)$ Between 3.78 and 5 MeV:

A total of ten spectra were taken at angles from 15° to 150° and ^3He energies from 3.78 to 5 MeV. In all of the spectra the 0.0, 2.18, 3.56 and 5.35 MeV levels are seen and perhaps a

broad level at 4.4 MeV, though the last group is too broad and weak to be unambiguously interpreted. In none of the spectra is there evidence for levels above 6 MeV. A sample spectrum, taken at a bombarding energy of 3.78 MeV, is shown in fig. 38. The data was taken with the magnetic spectrometer and subsequently converted to an alpha-particle energy representation. Positions of the levels found by Allen et al. are indicated.

(b) Spectra for $E(^3He) = 10$ MeV

The alpha continuum increases rapidly as the bombarding energy is raised, due at least in part to the increasing availability of processes which emit alpha-particles in a second stage. For example, highly excited states in ^9Be, ^9B and ^8Be, populated by $(^3He, p)$, $(^3He, n)$ and $(^3He, d)$ reactions respectively, may produce secondary alpha particles by their decay. The alpha spectra taken at $E(^3He)$ near 10 MeV are characterized by an intense continuum which complicates the search for ^6Li levels considerably. A sample spectrum is given in fig. 39. The levels at 0.0, 2.18, 3.56 and 5.35 MeV in ^6Li are clearly discernible. Also prominent are groups at frequencies of approximately 33 and 23 MC/S. These groups represent dramatic evidence that a bump on the spectrum of c particles from a reaction of the type A(b, c)D does not necessarily correspond to a state in the nucleus D. The group at 33 MC/S, which was studied in some detail, comes not from a state in ^6Li but from the two stage process $^7Li(^3He, d)$ $^8Be(16.62\,MeV)(\alpha)^4He$. This identification of the group was established from two types of experimental information, as discussed below. The first was the agreement between the measured energy

distribution of the alpha particles and the shape predicted from the angular distribution of the deuterons populating the 16.62 MeV state in ^{8}Be; the second was the kinematic behavior of the group as the bombarding energy was changed.

The lack of definition of the ^{8}Be recoil velocity in the above two stage process will result in the alpha particles' presenting a continuum distribution at given laboratory angle, kinematically constrained to lie within some energy limits which are functions of the bombarding energy, angle and Q-values. These limits are indicated, for example, in fig. 39 for the sequences ^{7}Li(^{3}He, d) ^{8}Be(16.62 MeV)(α)^{4}He and ^{7}Li(^{3}He, d)^{8}Be(g. s.)(α)^{4}He. If the ^{8}Be nucleus is emitted preferentially in some laboratory direction, its momentum becomes more nearly defined, and the resulting energy distribution of the alpha particles will reflect this characteristic by tending to form a peak in their energy spectrum.

The angular distribution for the reaction ^{7}Li(^{3}He, d) ^{8}Be(16.62 MeV) was measured for the purposes of verifying that the 33 MC/S alpha-particle group in fig. 39 did in fact come from the breakup of this state in ^{8}Be. Fig. 40 A shows a sample spectrometer deuteron yield in the vicinity of the 16.62 and 16.92 MeV levels in ^{8}Be; Fig. 40 B shows the center-of-mass angular distribution of the deuterons to the 16.62 MeV level in ^{8}Be. The angular distribution from the 16.9 2 MeV state in ^{8}Be was found to be roughly isotropic.

The effect of the strong forward peaking of the ^{8}Be(16.62 MeV) deuterons on the energy distribution of the subsequently emitted alpha-particles may be qualitatively understood by noting that the ^{8}Be recoil nucleus is preferentially emitted at $\theta = 180^O$. If the alpha particle is observed at a forward angle the

recoil velocity of the ^{8}Be is preferentially directed against the laboratory alpha velocity, tending to group the alpha energies at their low energy limit.

A quantitative evaluation of the alpha spectrum expected was calculated from the observed ^{8}Be(16.62 MeV) deuteron angular distribution, assuming isotropic ^{8}Be decay. The result is shown as a shaded group in fig. 39, with its expected intensity. The formulae of Morinigo (1963) were used in the calculation; the width of the ^{8}Be(16.62 MeV) level was taken to be 100 keV.

An independent check on the interpretation of this alpha group is provided by tracking the position of its lower edge as the bombarding energy is changed. Fig. 41 shows that this edge follows nicely the kinematics expected for the ^{7}Li(^{3}He, d)^{8}Be(16.62 MeV)(α)^{4}He process, and not at all the kinematics expected for a group leaving a state in ^{6}Li.

Although no such exhaustive study has been given the group at 23 MC/S in fig. 39, it is believed to come from the process ^{7}Li(^{3}He, d)^{8}Be(g. s.)(α)^{4}He. This interpretation is based solely on the agreement of the location of its high energy edge in this spectrum with that expected for the ^{8}Be(g. s.) process.

(2) At E(^{3}He) = 900 keV

The failure of attempts to find levels above 6 MeV in ^{6}Li at higher beam energies suggested that an alpha-particle spectrum should be taken under conditions as similar as possible to those used by Allen et al. For this phase of the work the Kellogg 3 MV Van de Graaff generator provided a 900 keV singly-charged beam of 0.5 μa of ^{3}He. The alpha particles were detected at the focus

a 40-cm double focusing magnetic spectrometer, using a surface barrier solid state counter and foil arrangement for particle identification. The target used was of Li_2O on a tantalum backing, and is described on page 11 .

The buildup of carbon on the surface of the target was such that, by the end of the fourteen hours required to complete the run, the beam energy was degraded by 50 keV in passing through the carbon layer. Because of the high coulomb barrier in the incident channel, this energy loss resulted in an observed 16 percent decrease in counting rate. A correction factor proportional to total charge delivered to the target was applied to the observed number of counts to compensate for this loss in counting rate. No corresponding corrections were applied to the energy scale. The use of a Li_2O target, $E(^3He) = 900$ keV and $\theta = 90^O$ were conditions common to the experiment of Allen et al.

The resulting spectrum is shown in fig. 42. ^6Li recoil ions from $^6Li(0.0$ MeV) and $^6Li(3.56$ MeV) were also seen. Fig. 42 shows the same spectrum converted to an alpha-particle energy representation. The states above 6 MeV are not observed, and we must conclude that these states in the spectrum of Allen et al. were spurious. Thinking it not impossible that these peaks could have resulted from proton or deuteron beam contaminants in the experiment of Allen et al., we have run proton and deuteron beams on $^7Li_2O$ targets. No peaks which could have been mistaken for these states in ^6Li were observed.

Average values of excitations and widths of ^6Li levels found in the present work are given in table VIII.

REFERENCES

F. Ajzenberg-Selove and T. Lauritsen, Nucl. Phys. 11, 1 (1959).

E. Almqvist, K. W. Allen, and C. B. Bigham, Phys. Rev. 99, 631A (1955).

K. W. Allen, E. Almqvist and C. B. Bigham, Proc. Phys. Soc. 75, 913 (1960).

F. C. Barker, Nucl. Phys. 28, 96 (1961).

F. C. Barker and P. B. Treacy, Nucl. Phys. 38, 33 (1962).

F. C. Barker, Nucl. Phys. 83, 418 (1966).

F. C. Barker, private communication (1966a).

J. Benveniste, R. G. Finke, and E. A. Martinelli, Phys. Rev. 101, 655 (1956).

J. S. Blair and E. M. Henley, Phys. Rev. 112, 2029 (1959).

D. Bodansky, S. F. Eccles and I. Halpern, Phys. Rev. 108, 1019 (1957).

H. Brafman, Nuc. Inst. and Meth. 34, 239 (1965).

R. Britten, Phys. Rev. 88, 283 (1952).

A. B. Brown, C. W. Snyder, W. A. Fowler and C. C. Lauritsen, Phys. Rev. 82, 159 (1951).

J. A. Careaga and M. Mazari, Bull. Am. Phys. Soc. 8, 124 (1963).

C. M. Chesterfield and B. M. Spicer, Nucl. Phys. 41, 675 (1963).

P. R. Christensen and C. L. Cocke, Nucl. Phys. 89, 656 (1967).

S. Cohen and D. Kurath, Nucl. Phys. 73, 1 (1965).

R. Y. Cusson, Ph. D. Thesis, California Institute of Technology (1965).

R. B. Day and R. L. Walker, Phys. Rev. 85, 582 (1952).

R. D. Edge and G. A. Peterson, Phys. Rev. 128, 2750 (1962).

A. Galonsky, R. A. Douglas, W. Haeberli, M. T. McEllistrem and H. T. Richards, Phys. Rev. 98, 586 (1955).

A. Galonsky and M. T. McEllistrem, Phys. Rev. 98, 590 (1955).

J. Gillespie, Final State Interactions, Holden Day, Inc., San Francisco, California, pp. 2-13 (1964).

G. M. Griffiths, Nucl. Phys. 65, 647 (1965).

D. E. Groce, Ph. D. Thesis, California Institute of Technology (1963).

D. E. Groce and W. Whaling, Phys. Rev. 132, 2614 (1963).

E. Guth and C. J. Mullin, Phys. Rev. 76, 234 (1949).

D. Hasselgren, P. U. Renber, O. Sundberg, and G. Tibell, Nucl. Phys. 69, 81 (1965).

D. R. Inglis, Rev. Mod. Phys. 25, 390 (1953).

M. J. Jakobson, Phys. Rev. 123, 229 (1961).

P. D. Kunz, Ann. Phys. (New York) 11, 275 (1960).

D. Kurath, Phys. Rev. 101, 216 (1956).

D. Kurath, Phys. Rev. 140, B1190 (1965).

D. Kurath, private communication (1966).

J. Linck, S. Nicolas, R. Bilwes and D. Magnette-Valette, J. Physique Rad. 22, 581 (1961).

J. Linck, I. Nicolas-Linck, R. Bilwes and D. Magnette-Valette, J. Physique 24, 983 (1963).

A. M. Lane, Rev. Mod. Phys. 32, 519 (1960).

T. Lauritsen and F. Ajzenberg-Selove, Nucl. Phys. 78, 1 (1966).

T. Lauritsen, T. Huus and S. G. Nilsson, Phys. Rev. 92, 1501 (1953).

B. Lynch, G. M. Griffiths, and T. Lauritsen, Nucl. Phys. 65, 641 (1965).

J. B. Marion, J. S. Levin and L. Cranberg, Phys. Rev. 114, 1584 (1959).

J. H. McNally, Ph. D. Thesis, California Institute of Technology (1966).

J. H. Van der Merwe, Phys. Rev. 131, 2181 (1963).

C. D. Moak, A. Golonsky, R. L. Traughber, and C. M. Jones, Phys. Rev. 110, 1369 (1958).

F. B. Morinigo, Ph. D. Thesis, California Institute of Technology (1963).

J. Mösner, G. Schmidt and J. Schintlmeister, Nucl. Phys. 64, 169 (1965).

H. Nguyen Ngoc, M. Hors and J. Perez y Jorba, Nucl. Phys. 42, 62 (1963).

S. G. Nilsson, Mat. Fys. Medd. Dan. Vid. Selsk. 29, No. 16 (1955).

W. T. Pinkston, Phys. Rev. 115, 963 (1959).

P. Purdom, Jr., P. A. Seeger and R. W. Kavanagh, Nucl. Phys. 83, 513 (1966).

F. L. Ribe and J. D. Seagrave, Phys. Rev. 94, 934 (1958).

B. V. Rybakov and V. A. Sidorov, Fast-neutron spectroscopy, ed.,
N. A. Vlasov (translated from Russian, Consultants
Bureau, New York, 1960).

G. Schrank, E. K. Warburton and W. W. Daehnik, Phys. Rev. 127,
2159 (1962).

N. A. Schuster and G. E. Pake, Phys. Rev. 81, 886 (1951).

L. S. Senhouse, Jr. and T. A. Tombrello, Nucl. Phys. 57, 624 (1964).

R. R. Spencer, G. C. Phillips and T. E. Young, Nucl. Phys. 21, 310
(1960).

G. J. Stephenson, Jr., Proc. of the Int. Conf. on Nuclear Physics,
Gatlinburg, Tennessee, Sept. (1966).

R. G. Summers-Gill, Phys. Rev. 109, 1591 (1958).

C. D. Swartz and G. E. Owen, Fast neutron physics, part I,
chapter II B, ed., J. B. Marion and J. L. Fowler (Inter-
science Publishers, New York, 1960).

T. A. Tombrello and L. S. Senhouse, Phys. Rev. 129, 2252 (1963).

R. G. Thomas, Phys. Rev. 81, 148 (1951).

E. K. Warburton, D. E. Alburger and D. H. Wilkinson, Phys. Rev.
129, 2180 (1963).

E. K. Warburton, D. E. Alburger, D. D. Wilkinson and J. M. Soper,
Phys. Rev. 129, 2191 (1963).

D. H. Wilkinson, J. T. Sample and D. E. Alburger, Phys. Rev. 146,
662 (1966).

W. S. C. Williams, An Introduction to Elementary Particles, Academic Press, New York, New York, pp. 356-378 (1961).

Table I

Summary of Data from ^{7}Li(^{3}He, p)^{9}Be Singles

A summary by individual spectrum is shown of the data from which the average excitations of levels in ^{9}Be were found. For each level and for each spectrum the beam energy, observation angle, calculated excitation and estimated excitation error are given. The value of chi-squared, divided by(the number of degrees of freedom minus one), was calculated for the best fit to a single Q-value for each proton group, using the listed error estimates, and assuming target masses of 6, 7 and 9. Average level positions and intrinsic widths, both expressed in terms of excitation in ^{9}Be, are presented. See pages 12-15.

TABLE 1. Summary of Data from ^{7}Li(^{3}He, p)^{9}Be*

Proton Group	E(^{3}He) (MeV)	Lab. Proton Angle (degrees)	Excitation in ^{9}Be (MeV)		Chi-squared/(Number of degrees of freedom minus one) Assuming Target Mass:			Average Excitation in ^{9}Be (MeV)	Intrinsic Width in ^{9}Be (MeV)
			Value	Error	6	7	9		
p1	10	90	1.626	0.02	518.	.55	901.	1.64	
	8	90	1.650	0.02					
	8	15	1.653	0.02					
p2	10	90	2.418	0.02	496.	.23	930.	2.429 ± 0.012	≤ 0.035
	8	90	2.436	0.02					
	8	15	2.432	0.02					
p3	10	90	3.029	0.02	259.	.72	605.	3.031 ± 0.010	0.274 ± 0.015
	8	90	3.034	0.02					
	8	15	3.009	0.02					
	10	90	3.051	0.02					
p4	8	15	4.46	0.2	3.56	.23	23.4	4.57 ± 0.1	$0.6 \leq \Gamma \leq 1.0$
	10	90	4.60	0.2					
	8	90	4.64	0.2					
p5	10	90	6.7	0.1	5.73	.12	10.9	6.7 ± 0.1	$1.7 \leq \Gamma \leq 2.2$
	8	90	6.7	0.1					
	8	15	6.8	0.2					
p6	10	1.7	11.31	0.02	59.6	.75	86.8	11.29 ± 0.03	0.62 ± 0.07
	10	60	11.27	0.03					
	7	10	11.28	0.03					
p7	10	1.7	11.81	0.01	59.5	.42	109.6	11.81 ± 0.02	0.40 ± 0.03
	10	60	11.81	0.03					
	7	10	11.83	0.02					
p8	9	12	13.78	0.04	17.9	.72	22.9	13.78 ± 0.03	0.59 ± 0.06
	10	50	13.78	0.03					
	10	90	13.6	0.15					
p9	10	10	16.670	0.01	59.9	.20	137.1	16.671 ± 0.008	0.041 ± 0.004
	10	30	16.665	0.02					
	12	45	16.678	0.01					
	10	15	16.670	0.01					

Table II

Comparison of Spectrometer and Surface Barrier Counter Spectra

A comparison is made of the parameters of eq. (13,1) used in fitting proton spectra from ^{7}Li(^{3}He, p)^{9}Be taken with the magnetic spectrometer (fig. 5, upper curve) and with a barrier counter (fig. 27). Both spectra were taken at E(^{3}He) = 10 MeV, $\theta_p \simeq 0^o$. All energies are expressed as excitations in the ^{9}Be system. The quantity A/B x Γ_2/Γ_1 is the ratio of intensities of the ^{9}Be(11.29 MeV) and ^{9}Be(11.81 MeV) levels. The greater values of the widths used for the solid state counter spectrum reflect the poorer experimental resolution in this case. See text, pages 35 and 36.

Table II

Comparison of Spectrometer and Solid State Spectra

Parameter	Spectrometer		Surface Barrier Counter
E_{R1} (MeV)	11.81	$\equiv$	11.81
$E_{R1} - E_{R2}$ (MeV)	.52	$\equiv$	.52
Γ_1 (MeV)	.620		.644
Γ_2 (MeV)	.400		.550
$\dfrac{A}{B} \times \dfrac{\Gamma_2}{\Gamma_1}$	.608		.562

Table III

Neutron Detector Efficiencies

The neutron detector efficiencies used in this calculation of branching ratios, with the corresponding assigned errors, are given. See text, pages 23 and 24.

Table III

Neutron Detector Efficiencies

$E(^3He)$ (MeV)	Excitation Range in ^9Be (MeV)	Neutron Energy Range (MeV)	Scintillator Thickness (cm)	Efficiency
2.2	2.4 - 3.5	1.0 - 3.3	5.08	$.42 \pm .04$
			1.9	$.19 \pm .02$
5.0	3.8 - 5.4	1.9 - 3.6	1.9	$.18 \pm .02$
9.0 - 10.0	12.5 - 10.3	5 - 8.6	5.08	$.28 \pm .04$

Table IV

^{9}Be Level Widths

The observed intrinsic widths of ^{9}Be levels, $\overline{\Gamma}_{TO}$, and the level widths, $\overline{\Gamma}_T$, which were used in the calculation of partial neutron widths are shown. All widths are given in terms of excitation in the ^{9}Be system. The difference between $\overline{\Gamma}_{TO}$ and $\overline{\Gamma}_T$ is explained in the text, page 44. Where no value of $\overline{\Gamma}_T$ is given, $\overline{\Gamma}_T$ was set equal to $\overline{\Gamma}_{TO}$ in the calculation of partial neutron widths. Unless otherwise indicated, values listed for excitations and observed widths are taken from table I. Experimental values for Jπ are taken from the recent compilations of Ajzenberg-Selove and Lauritsen (1966). See pages 43 and 44.

Table IV

^{9}Be Level Widths

Excitation (MeV)	$J\pi$	$\bar{\Gamma}_{TO}$ (keV)	$\bar{\Gamma}_{T}$ (keV)
2.43	$5/2^-$	$1.0 \pm .2$[b]	
3.03	$(5/2)^+$	265 ± 17	433 ± 28
4.65[a]	$5/2^+, 3/2^+$	900 ± 250[a]	930 ± 258
6.76	$7/2^-$	2300 ± 500[c]	2830 ± 615
11.29		640 ± 70	
11.81		410 ± 30	

(a) Text, page 34.

(b) Purdom et al., 1966.

(c) Text, page 42.

Table V

Partial and Reduced Neutron Widths

A summary of the partial widths, $\bar{\Gamma}_\ell$, and reduced widths, θ_ℓ^2, for neutron emission to ^{8}Be(g. s.) and ^{8}Be(2^+) from states in ^{9}Be found in the present experiment is shown. Values of the assumed ℓ-value of the outgoing neutron, the corresponding penetration factor, the measured branching ratio and the deduced values of partial and reduced neutron widths are given. All calculations have been done for a channel radius R = 4.35 fm. The reduced widths are expressed in units of $\hbar^2/mR^2 = 2.47$ MeV. See pages 43-45.

Table V

Partial and Reduced Neutron Widths

Decay to ^{8}Be(g. s.)

Excitation (MeV)	ℓ_n	kRP	Branching Ratio (percent)	$\bar{\Gamma}_\ell$ (keV)	θ_ℓ^2 ($\times 10^2$)
2.43	3	$.703 \times 10^{-3}$	7.5 ± 1.5	$.075 \pm .021$	$2.1 \pm .6$
3.03	2	$.921 \times 10^{-1}$	87 ± 13	377 ± 61	81 ± 13
4.65	2	.407	13 ± 4	121 ± 50	6.0 ± 2.5
6.76	3	.241	≤ 2	≤ 56	≤ 6
11.29	1	2.47	≤ 2	≤ 13	≤ 1
11.81	1	2.55	≤ 3	≤ 12	≤ 1

Decay to ^{8}Be(2^+)

Excitation (MeV)	ℓ_n	kRP	Branching Ratio (percent)	$\bar{\Gamma}_\ell$ (keV)	θ_ℓ^2 ($\times 10^2$)
6.76	1	.849	$.41 \leq B.R. \leq .69$	$1160 \leq \Gamma_\ell \leq 1950$	$.28 \leq \theta_\ell^2 \leq .47$
11.29	1	1.964	14 ± 4	90 ± 27	$.93 \pm .28$
	3	.464			$4.0 \pm .12$
11.81	1	2.064	12 ± 4	49 ± 16	$.48 \pm .16$
	3	.540			$1.8 \pm .6$

Table VI

Theoretical Reduced Widths

Reduced widths to ^{8}Be(g. s.) and ^{8}Be(2^+) from levels in ^{9}Be, calculated from the 1p-shell wave functions of Cohen and Kurath (1965) and Barker (1966) are shown. All reduced widths are calculated for p-wave neutron emission, and are normalized to a single particle reduced width $\theta_{sp}^2 = .6$. The excitation values are those calculated by Barker (1966), while the spectroscopic designations refer to the main components of the wave functions when they are expressed in an LS coupled basis. See pages 46-49.

Table VI

Theoretical Reduced Widths

Level	$J\pi$	Excitation (MeV)	$\theta_p^2 (\times 10^2)$ Kurath $^8\text{Be(g.s.)}$	$^8\text{Be}(2^+)$	Barker $^8\text{Be}(2^+)$
$[4,1]^{22}\text{P}$	$3/2^-$	0.0	34.8	43.5	
	$1/2^-$	2.02	43.2	27.6	
$[4,1]^{22}\text{D}$	$5/2^-$	2.41	0.0	68.7	
	$3/2^-$	4.60	3.0	69.3	
$[4,1]^{22}\text{F}$	$5/2^-$	5.90	0.0	23.7	
	$7/2^-$	6.14	0.0	12.6	
$[4,1]^{22}\text{G}$	$9/2^-$	10.46	0.0	0.0	0.0
	$7/2^-$	11.35	0.0	1.5	2.2
$[3,2]^{22}\text{P}$	$1/2^-$	11.88			0.07
	$3/2^-$	12.76			0.11

Table VII

Positive Parity States

A comparison between the present experimental results for neutron decay widths to ^{8}Be(g. s.) by positive parity levels in ^{9}Be is made with the theoretical calculations made by Barker (1961). Theoretical calculations of the observed total widths and partial neutron widths which are enclosed in parentheses are not expected by Barker to be reliable, but are included for completeness. Unless otherwise indicated, experimental values for $\overline{\Gamma}_{TO}$ are taken from table IV, and values for $\overline{\Gamma}_{\ell}$ and θ^2 are taken from table V. Experimental values for J_π are taken from the recent compilation of Ajzenberg-Selove and Lauritsen (1966). See pages 49-51.

Table VII

Positive Parity States

Decay to ^{8}Be(g. s.)

Theoretical

Excitation (MeV)	Jπ	$\overline{\Gamma}_{TO}$ (keV)	ℓ_n	$\overline{\Gamma}_\ell$ (keV)
1.75	$1/2^+$	(530)	0	(560)
3.04	$5/2^+$	150	2	230
4.84	$3/2^+$	(1000)	2	180

Experimental

Excitation (MeV)	Jπ	$\overline{\Gamma}_{TO}$ (keV)	ℓ_n	$\overline{\Gamma}_\ell$ (keV)	θ_ℓ^2 ($\times 10^2$)
1.67	$1/2^+$	224 ± 25[a]	0		
3.03	$(5/2)^+$	265 ± 17	2	377 ± 61	81 ± 13
4.65	$3/2^+$, $5/2^+$	900 ± 250	2	121 ± 50	6.0 ± 2.5

[a] Ajzenberg-Selove and Lauritsen (1966).

Table VIII

Excitations and Widths of States in ^{6}Li from ^{7}Li(^{3}He,α)^{6}Li

The excitations and widths of states in ^{6}Li found in the reaction ^{7}Li(^{3}He, α)^{6}Li by Allen et al. (1960), by Linck et al. (1963) and in the present work are shown. All energies are in MeV. The widths are expressed in terms of energy in the ^{6}Li system. See pages 81, 82 and 85.

Table VIII

Excitations and Widths of States in ^{6}Li from ^{7}Li(^{3}He, α)^{6}Li

Allen et al.		Linck et al.		Present	
Excitation	Γ	Excitation	Γ	Excitation	Γ
0	0	0	0	0	0
2.187	$\leq$ .1	2.179 $\pm$ .008	$\leq$.04	2.17 $\pm$ .02	
3.56 $\pm$ 0.06	$\leq$ .1	3.568 $\pm$ .008	$\leq$.04	3.55 $\pm$ .02	
4.3 $\pm$ 0.2					
5.35 $\pm$ 0.07	.1	5.47 $\pm$ .04	.600	5.34 $\pm$ .02	.36 $\pm$ .04
5.6 $\pm$ 0.2	2.0				
6.63 $\pm$ 0.08	.2				
7.40 $\pm$ 0.10	.6				
8.37 $\pm$ 0.08	.2				
(9.3 $\pm$ 0.2)	.6				

Figure 1

A proton spectrum from the magnetic spectrometer taken at $E(^3He)$ = 10 MeV, θ_p = 90° is shown. The abscissa is the frequency of the nuclear magnetic resonance probe used to measure the magnetic field strength. The region between 33.2 and 37.0 MC/S was taken with a thinner target than was the remaining spectrum. Corrections for energy loss in the target by both beam and protons have not yet been made. Groups at 7.94 and 9.1 MeV are not in evidence. See page 12.

Figure 1
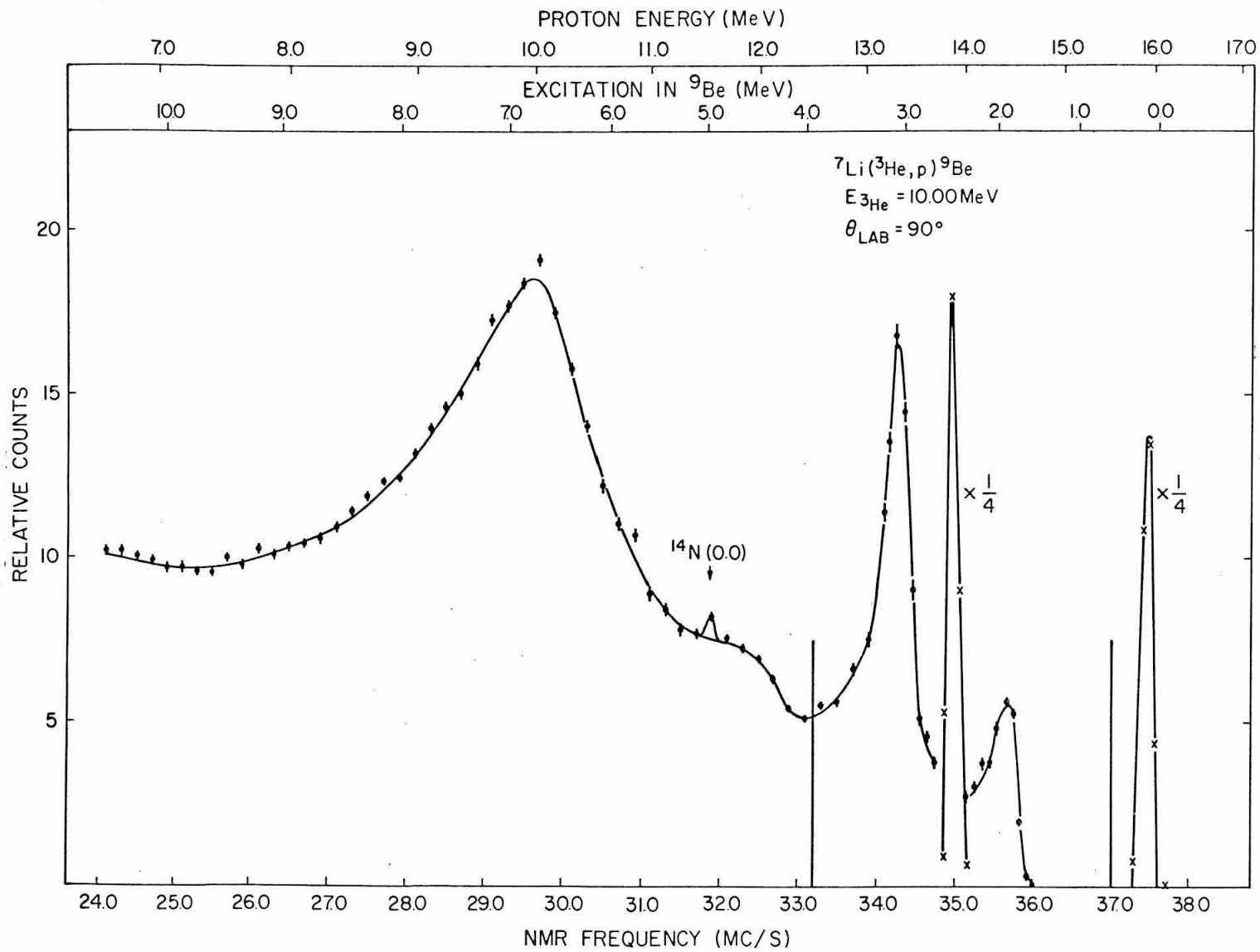
Figure 2

A proton spectrum from the magnetic spectrometer taken at $E(^3He) = 8$ MeV, $\theta_p = 90^O$ is shown. Corrections for energy loss in the target by both the beam and protons have not yet been made. See page 12.

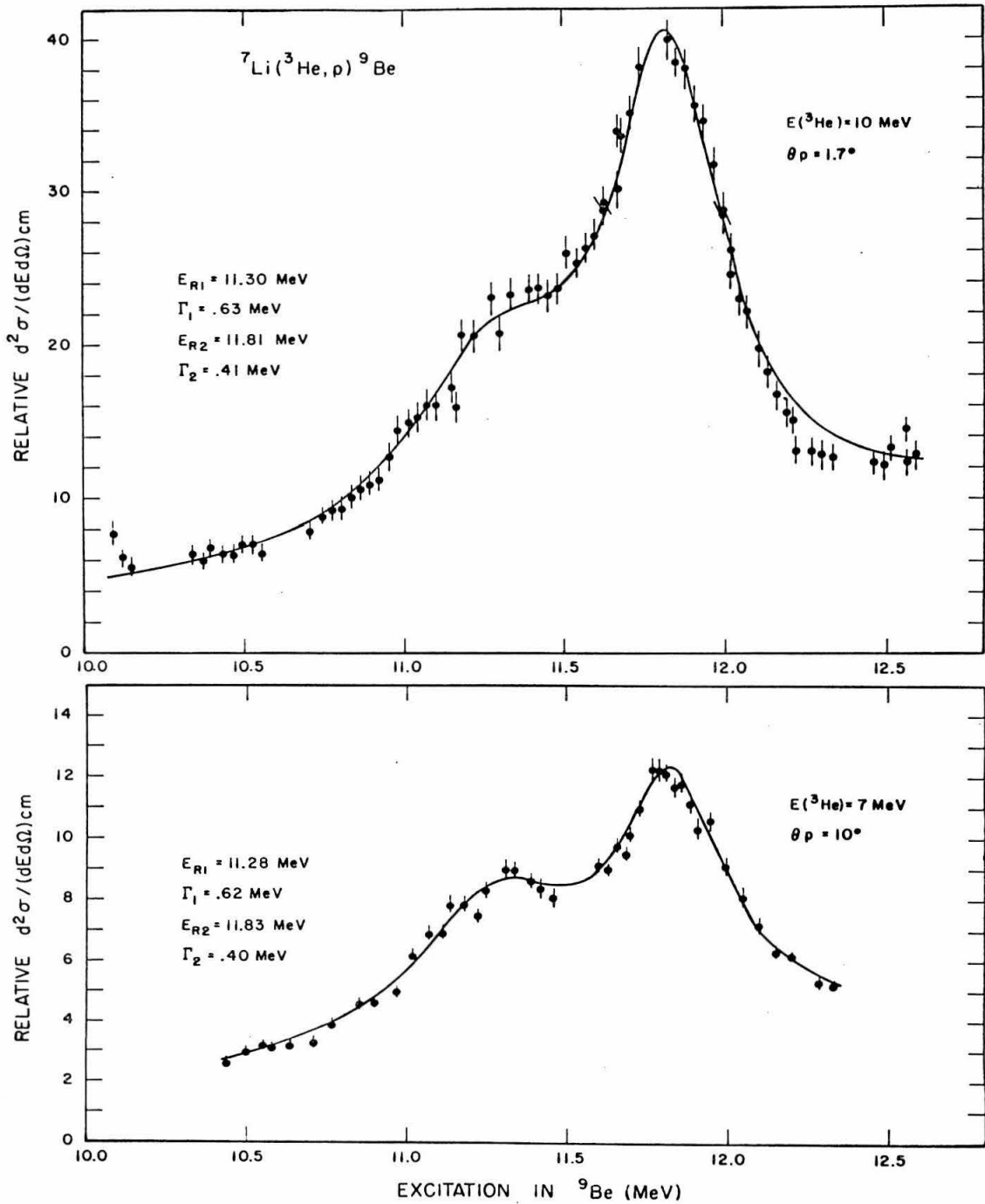Figure 2
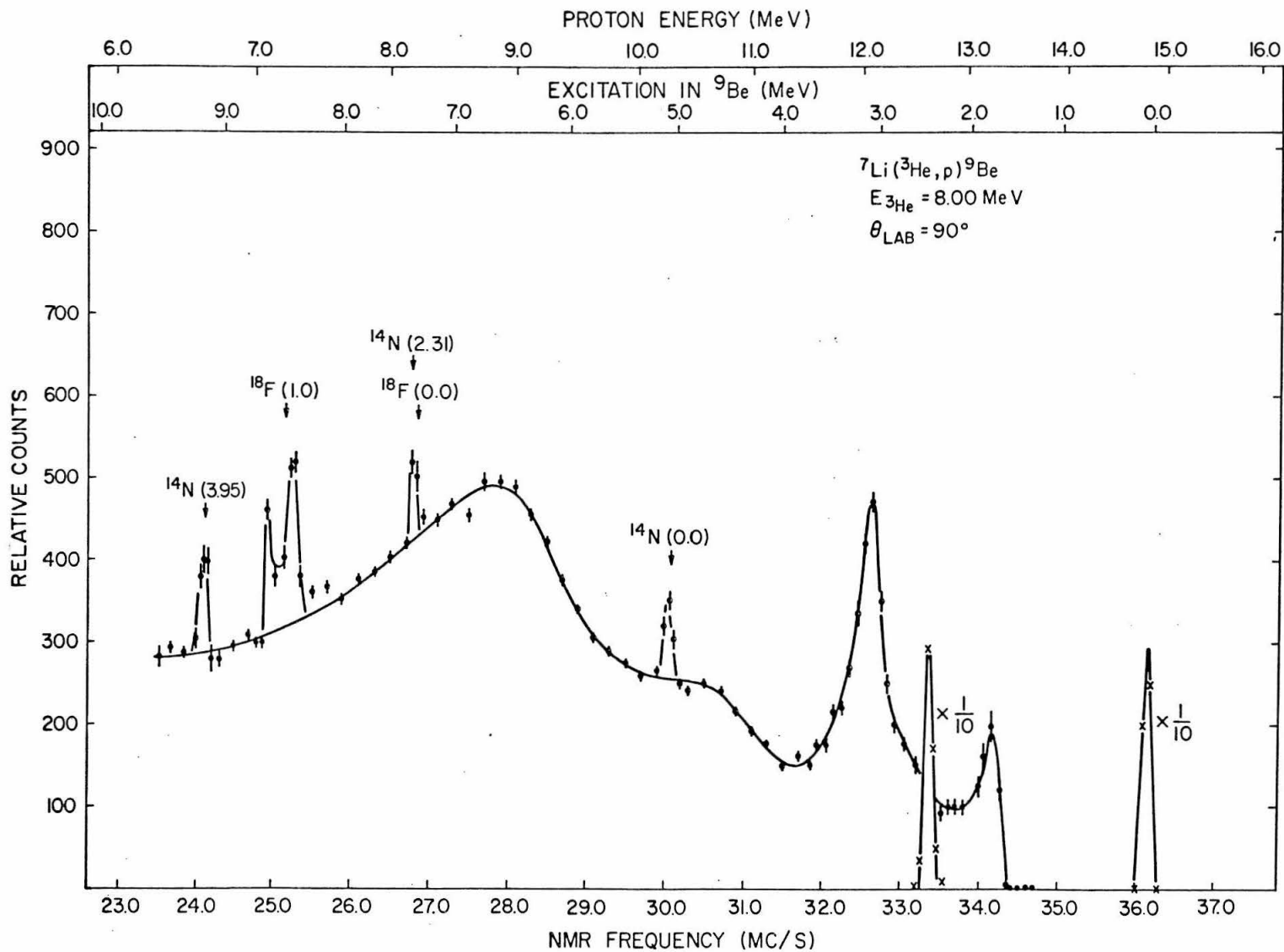
Figure 3

A proton spectrum from the magnetic spectrometer taken at $E(^3He) = 8$ MeV, $\theta_p = 15^O$ is shown. The 4.6 MeV state in ^9Be stands out more clearly in this spectrum than in any others taken. Double-peaked contaminants are from carbon buildup on both sides of the target. Corrections for energy loss in the target by both the beam and protons have not yet been made. See page 12.

Figure 3

PROTON ENERGY (MeV)

EXCITATION IN ^{9}Be (MeV)

^{14}N (2.31)

^{18}F (0.0)

^{14}N (0.0)

^{7}Li(^{3}He,p)^{9}Be
E_{3He} = 8.00 MeV
θ_{LAB} = 15°

RELATIVE COUNTS

NMR FREQUENCY (MC/S)

$\times \frac{1}{10}$

$\times \frac{1}{10}$

112
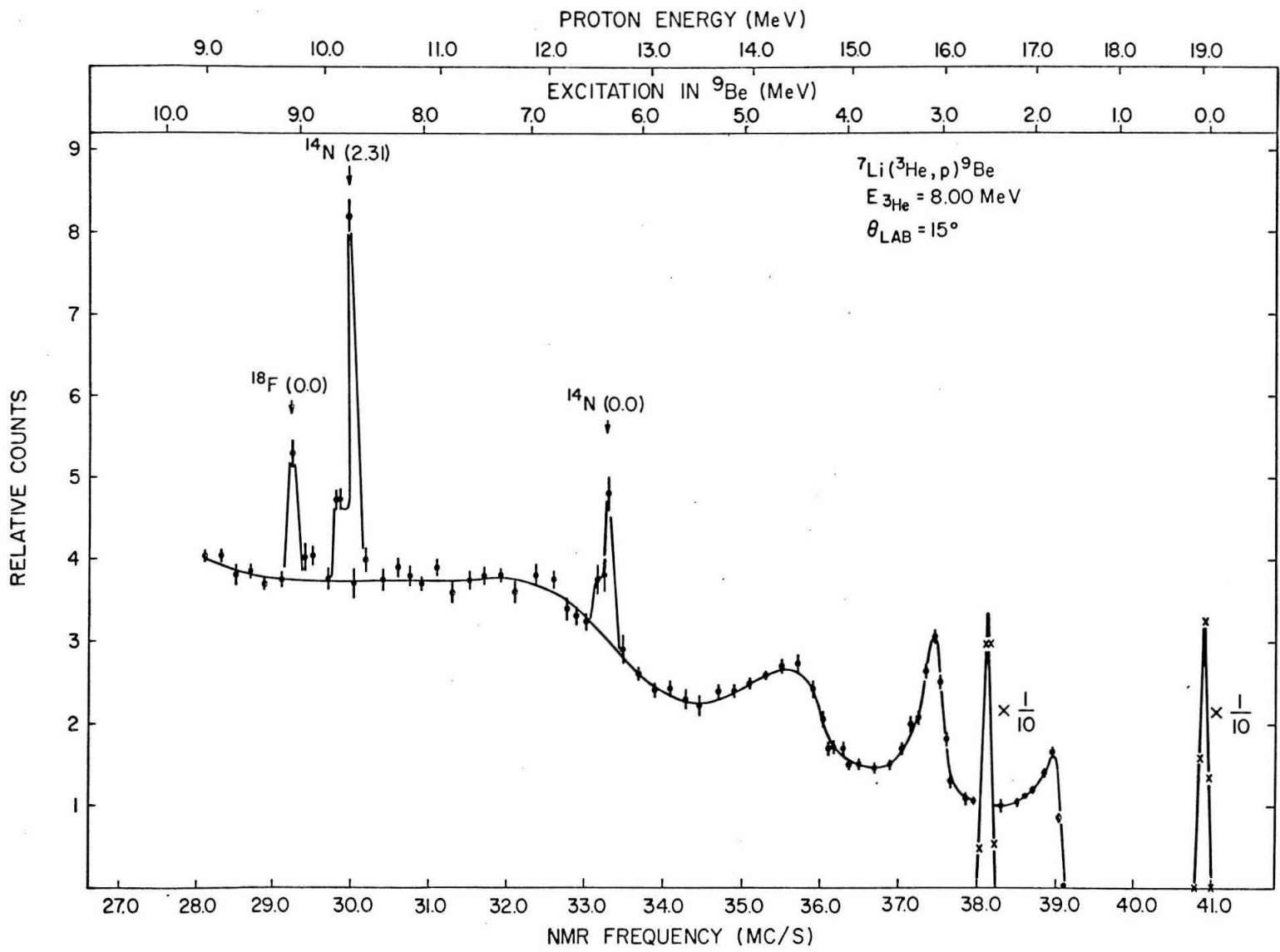
Figure 4

A proton spectrum from the magnetic spectrometer taken at $E(^3He) = 10$ MeV, $\theta_p = 1.7^O$, demonstrates the carbon contamination problem in the excitation region around the 11.29 MeV and 11.81 MeV levels in ^{9}Be. Points shown as triangles were taken immediately following evaporation of the lithium target. Points shown as solid dots were then taken, scanning toward higher frequencies beginning at 26.0 MC/S, in 15 μc runs. Points shown as x's were taken after the target had been bombarded by 1750 μc. The +'s show the proton yield from the reaction $^{12}C(^3He, p)^{14}N$, for which a natural carbon target was used. The growth with bombardment of carbon on the lithium target is apparent. See pages 10-12.

Figure 4

114

PROTON ENERGY (MeV)

EXCITATION IN ^{9}Be (MeV)

^{7}Li(^{3}He,p)^{9}Be

$E_{^3He}$ = 10.00 MeV

θ_{LAB} = 1.7°

△ PROTONS FROM FRESH ^{7}Li TARGET

● SCAN TOWARD HIGHER FRE-QUENCIES IN 15μC RUNS

x AFTER 1,750μC BOMBARDMENT

+ PROTONS FROM CARBON FOIL

EX. IN ^{14}N (MeV)

NMR FREQUENCY (MC/S)
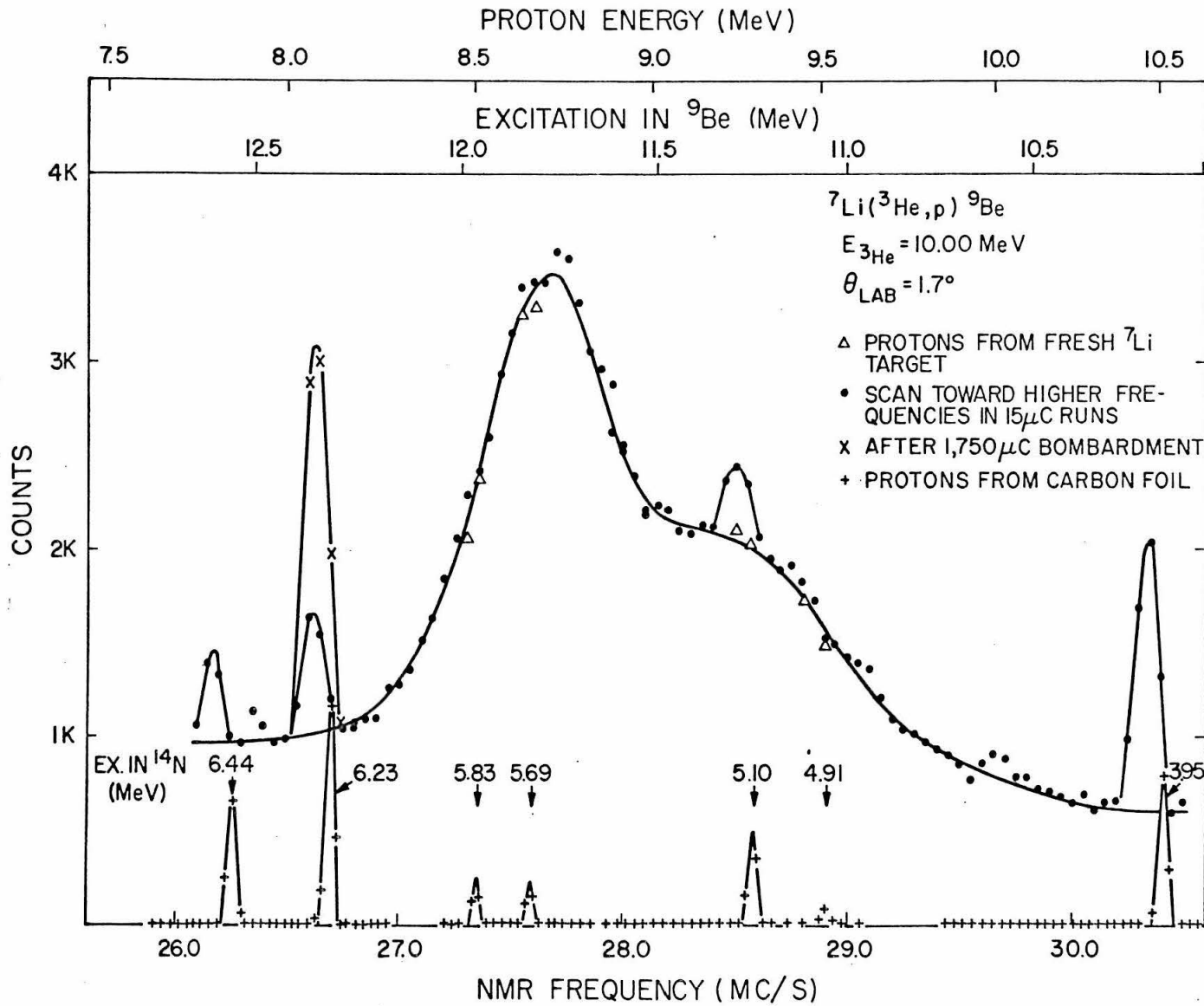
Figure 5

Excitation spectra, converted from magnetic analyzer spectra in the region of the 11.81 and 11.29 MeV states in ^{9}Be are shown for E(^{3}He) = 10 MeV, θ_p = 1.7^O and for E(^{3}He) = 7 MeV, θ_p = 10°. The spectrum at E(^{3}He) = 10 MeV is a conversion of fig. 4. Corrections for energy losses in the targets have been made. Regions suspected of having large contributions from contaminant lines have been omitted. The ordinates on the two spectra are independently arbitrarily normalized.

The solid lines have the form of two non-interfering Breit-Wigner resonance shapes superimposed on a linear background, as given by eq. (13,1). In each spectrum the parameters used in this equation were adjusted to yield the lowest value of chi-squared. The corresponding values of the resonance parameters found are shown in the two spectra. See pages 12 and 13.

Figure 5

Figure 6

A proton spectrum from the magnetic spectrometer taken at $E(^3He) = 9$ MeV, $\theta_p = 12^O$ is shown. Proton groups from states in ^9Be at 14.392 MeV and 13.78 MeV are seen. The group at 23.6 MC/S represents protons elastically scattered by hydrogen in the target. The width of this group is due to its large change in energy over the acceptance angle of the spectrometer. See pages 13 and 14.

Figure 6

PROTON ENERGY (MeV)

EXCITATION IN ^{9}Be (MeV)

^{7}Li(^{3}He,p)^{9}Be
E(^{3}He) = 10.00 MeV
$\theta_p = 15°$

COUNTS

NMR FREQUENCY (MC/S)

118
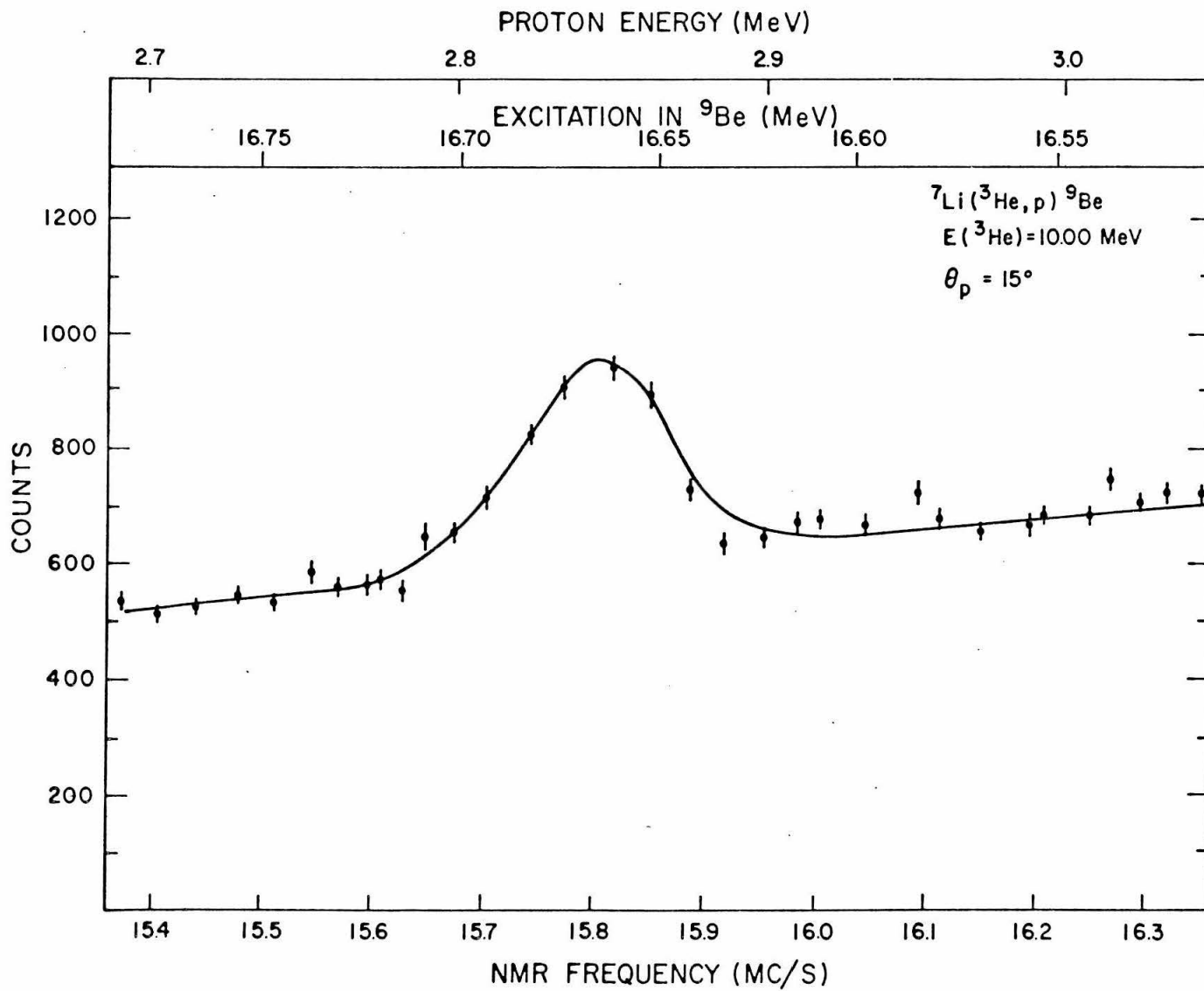
Figure 7

A proton spectrum from the magnetic spectrometer taken at $E(^3He) = 10$ MeV, $\theta_p = 15^O$ shows the 16.671 MeV state in ^9Be. See pages 14 and 15.

PROTON ENERGY (MeV)

EXCITATION IN ^{9}Be (MeV)

^{7}Li(^{3}He,p)^{9}Be

$E_{3_{He}}$ = 9.00 MeV

θ_{LAB} = 12°

p(^{3}He,p)^{3}He

COUNTS

Figure 7

120

NMR FREQUENCY (MC/S)
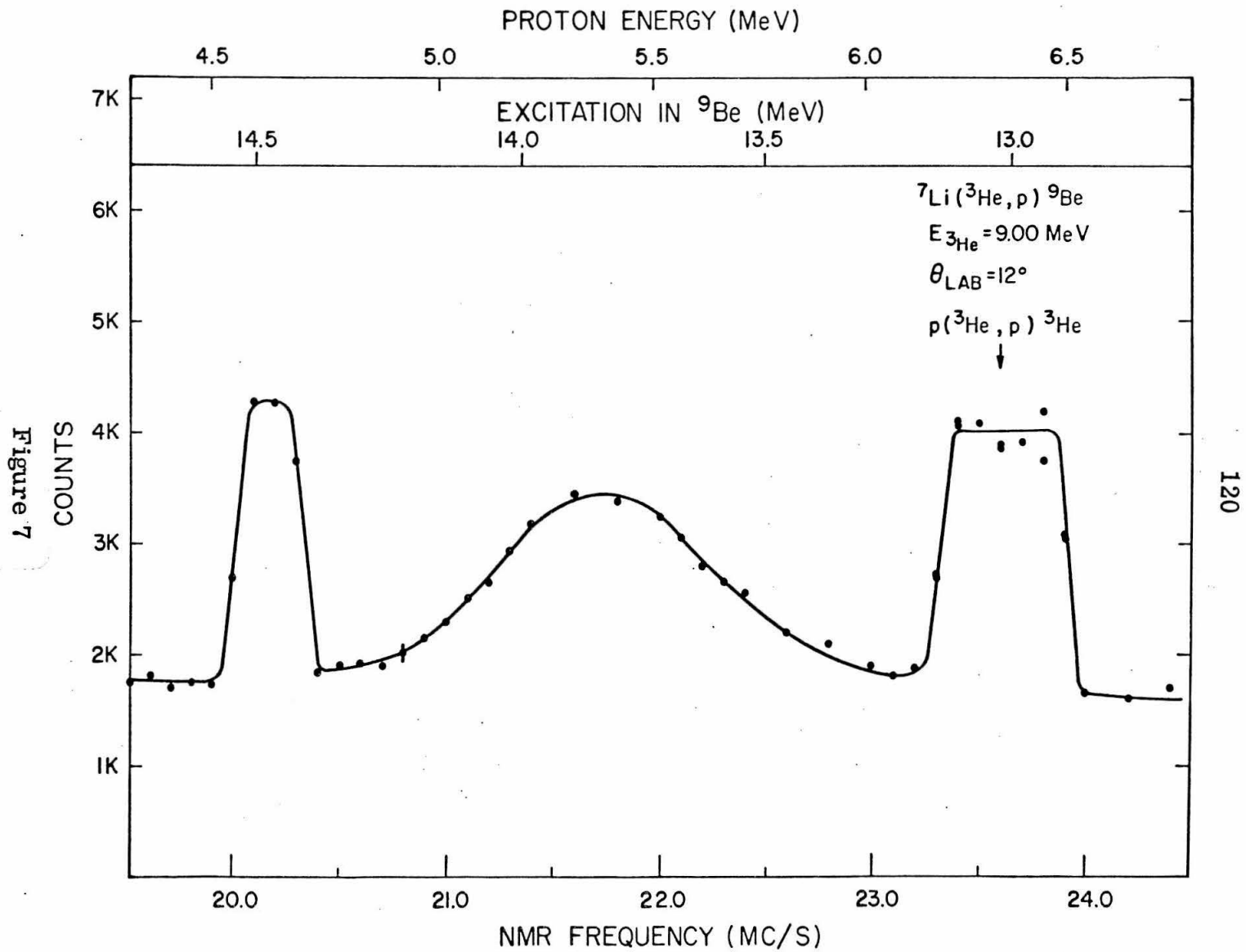
Figure 8

The velocity diagram for the sequence $^7\text{Li}(^3\text{He, p})^9\text{Be}(2.43)(\text{n})^8\text{Be}(\text{g. s.})$ is shown for the conditions used in the measurement of the $^8\text{Be}(\text{g. s.})$ decay from $^9\text{Be}(2.43 \text{ MeV})$. All velocities are to scale. See pages 18 and 19.

VELOCITY DIAGRAM
^{7}Li(^{3}He,p)^{9}Be(2.43)(n)^{8}Be(g.s.)
E(^{3}He) = 2.2 MeV
$\theta_{L,p}$ = 150°

^{3}He BEAM AXIS

$V_{L,p}$

$V_{L,n}$

$V_{C,n}$

$\theta_{C,n}$

$\theta_{L,n}$

$V_{L,^9Be}$

$\theta_{L,^9Be}$

$\theta_{L,p}$

Figure 8

122
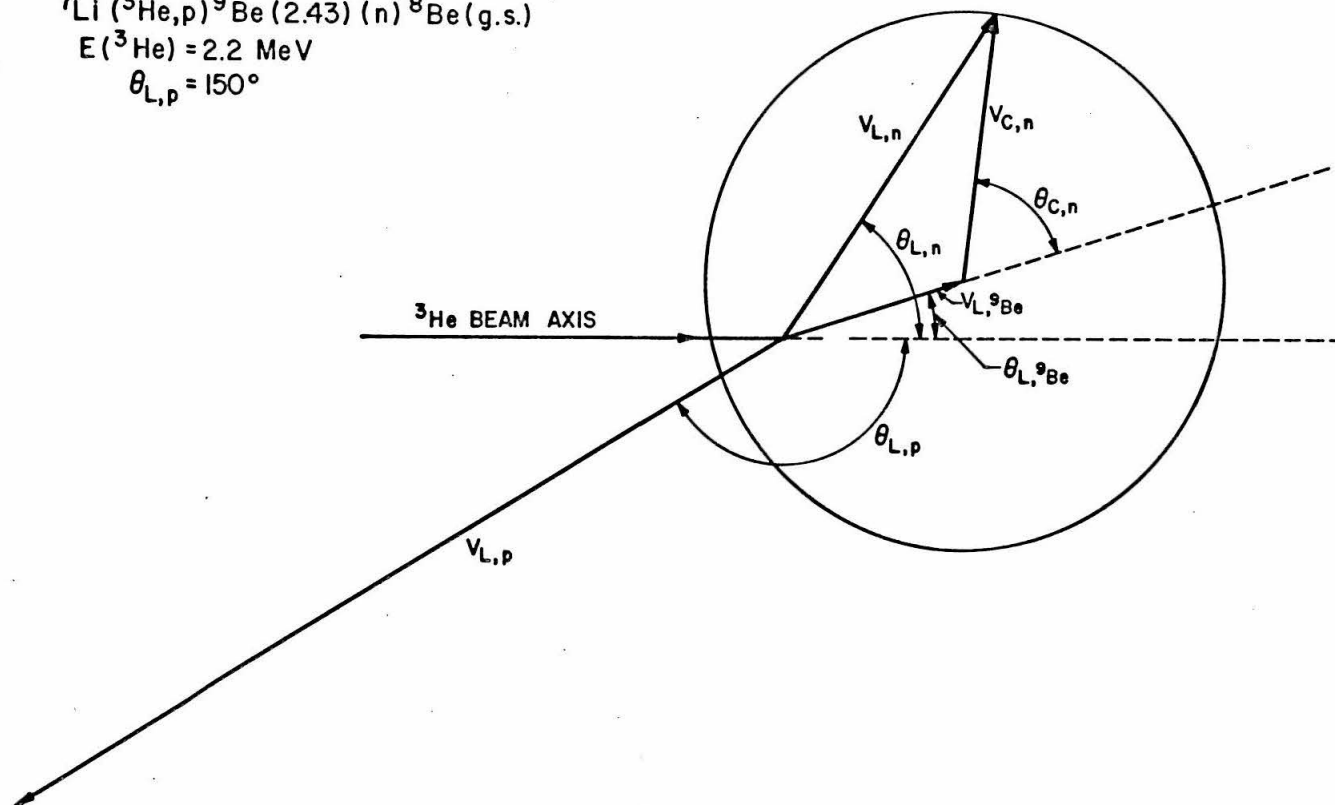
Figure 9

The solid curve represents the laboratory neutron time-of-flight spectrum which would result from the sequence ^{7}Li(^{3}He, p)^{9}Be(2. 43 MeV)(α)^{5}He(g. s.)(n)^{4}He, for values of the parameters given, if the decays of both ^{9}Be(2. 43 MeV) and ^{5}He(g. s.) are isotropic in their respective centers-of-mass. The α-particle has been taken to leave the ^{9}Be with and orbital angular momentum $\ell = 2$. A detailed description of the calculation is given in appendix B, pages 66-69 . The expected location of neutrons from the sequence ^{7}Li(^{3}He, p)^{9}Be(2. 43 MeV)(n)^{8}Be(g. s.) is indicated by an arrow. See page 19.

CALCULATED NEUTRON TIME SPECTRUM FROM
^{7}Li(^{3}He,p) ^{9}Be(2.43 MeV) (α) ^{5}He(g.s.)(n) ^{4}He

$E(^{3}$He) = 2.2 MeV

$\theta_{L,p}$ = 150°

$\theta_{L,n}$ = -15.7°

d = 100 cm

^{8}Be(g.s.)

Figure 9

124
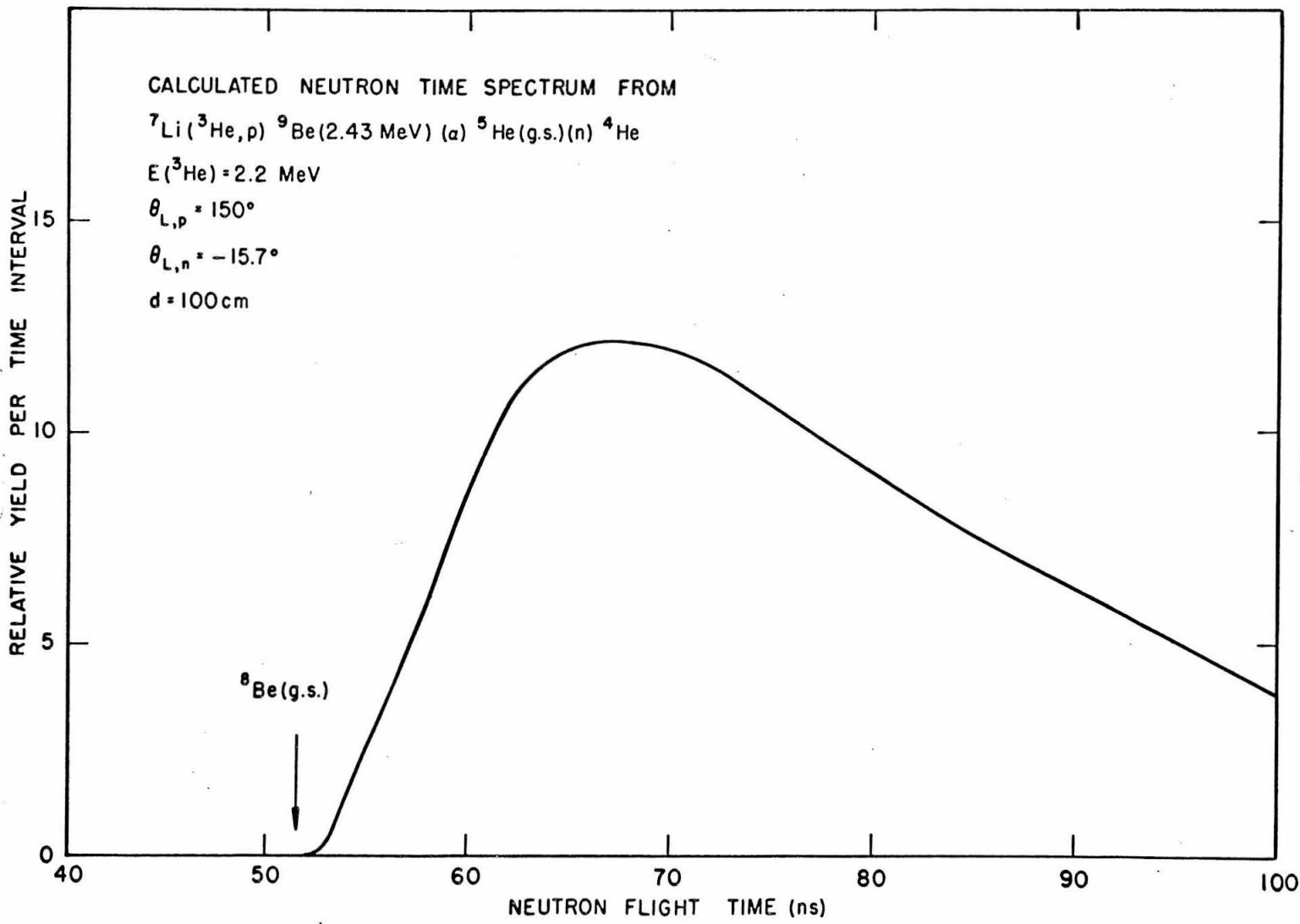
Figure 10

The target chamber used for the branching ratio
measurements is shown. The target transfer system is
shown schematically in the side view. The target rod may be
withdrawn into its sleeve, maintaining a vacuum between the
O-rings on the rod. The entire sleeve may then be transferred
to another vacuum system without exposing the target to the
atmosphere. See pages 20, 29 and 30.

BRASS

TARGET

NEUTRONS

^{3}He BEAM

COLLIMATOR

APERTURE

FOIL

SURFACE BARRIER DETECTOR

5 cm

TOP VIEW

LUCITE

TARGET

SURFACE BARRIER DETECTOR

BEAM AXIS
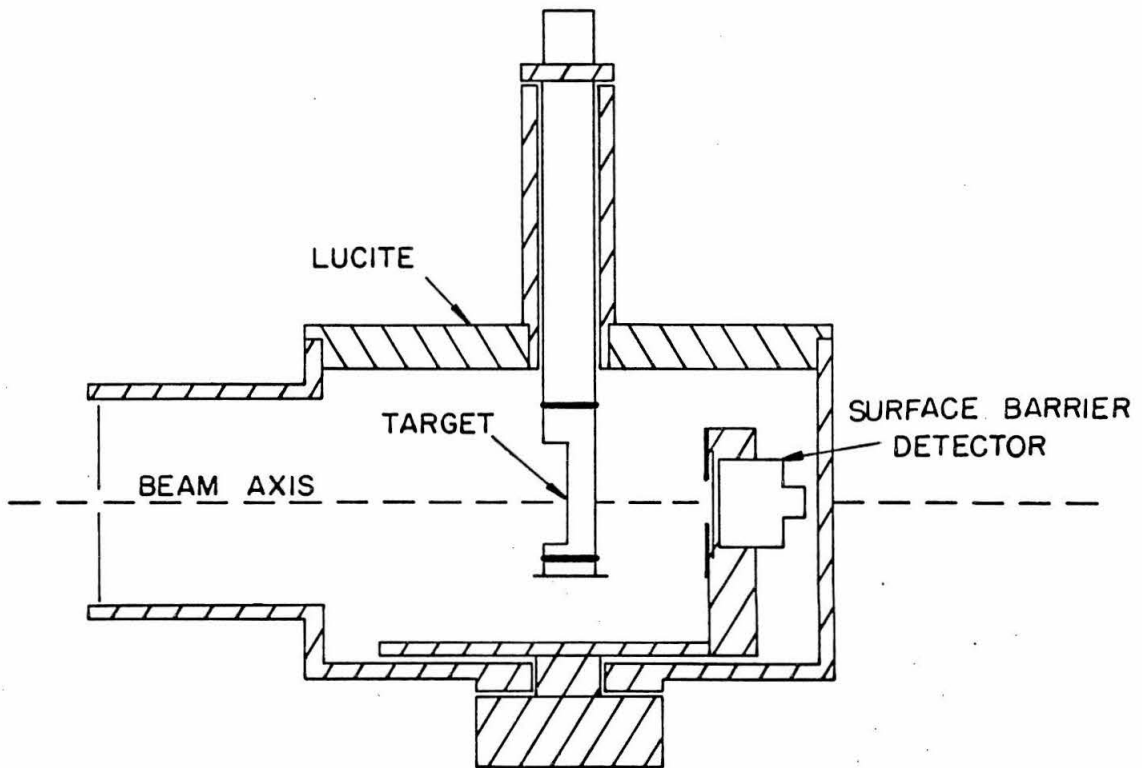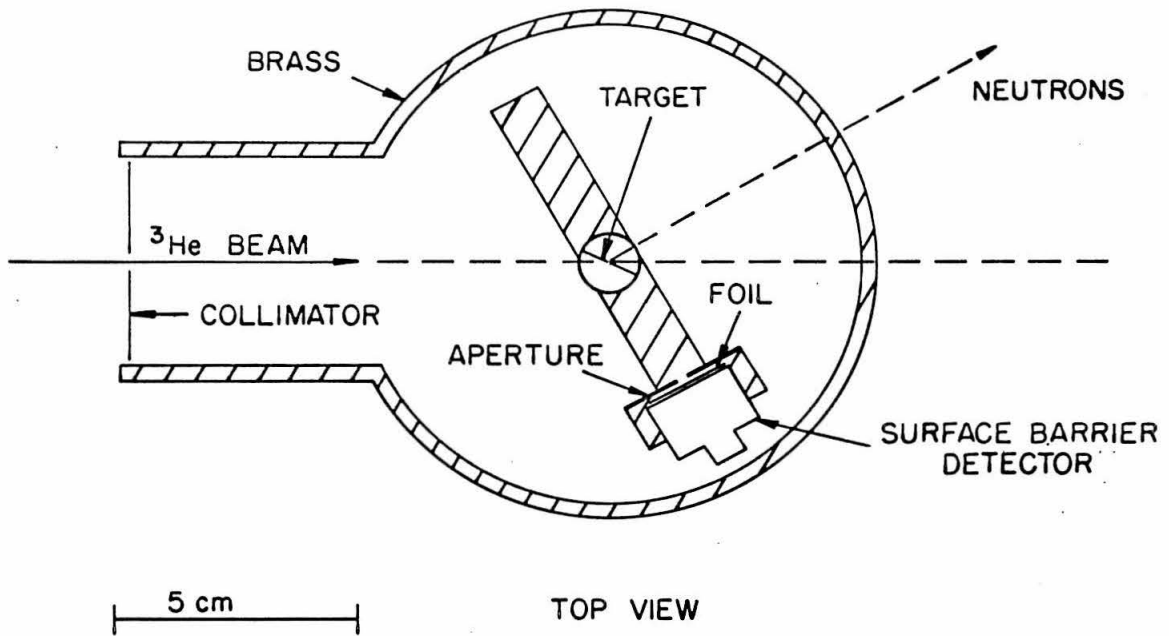
SIDE VIEW

Figure 10

Figure 11

A sample spectrum from the surface barrier detector used in the measurement of neutron decay from the 2.43 and 3.03 MeV states in ^{9}Be is shown. The counter was covered with a 0.023 cm. aluminum foil. The solid line shapes drawn below the proton groups from the 3.03 and 1.70 MeV states in ^{9}Be have the form of the appropriate "generalized density of states" functions (Barker and Treacy, 1962), folded into the experimental resolution. See pages 21 and 22.
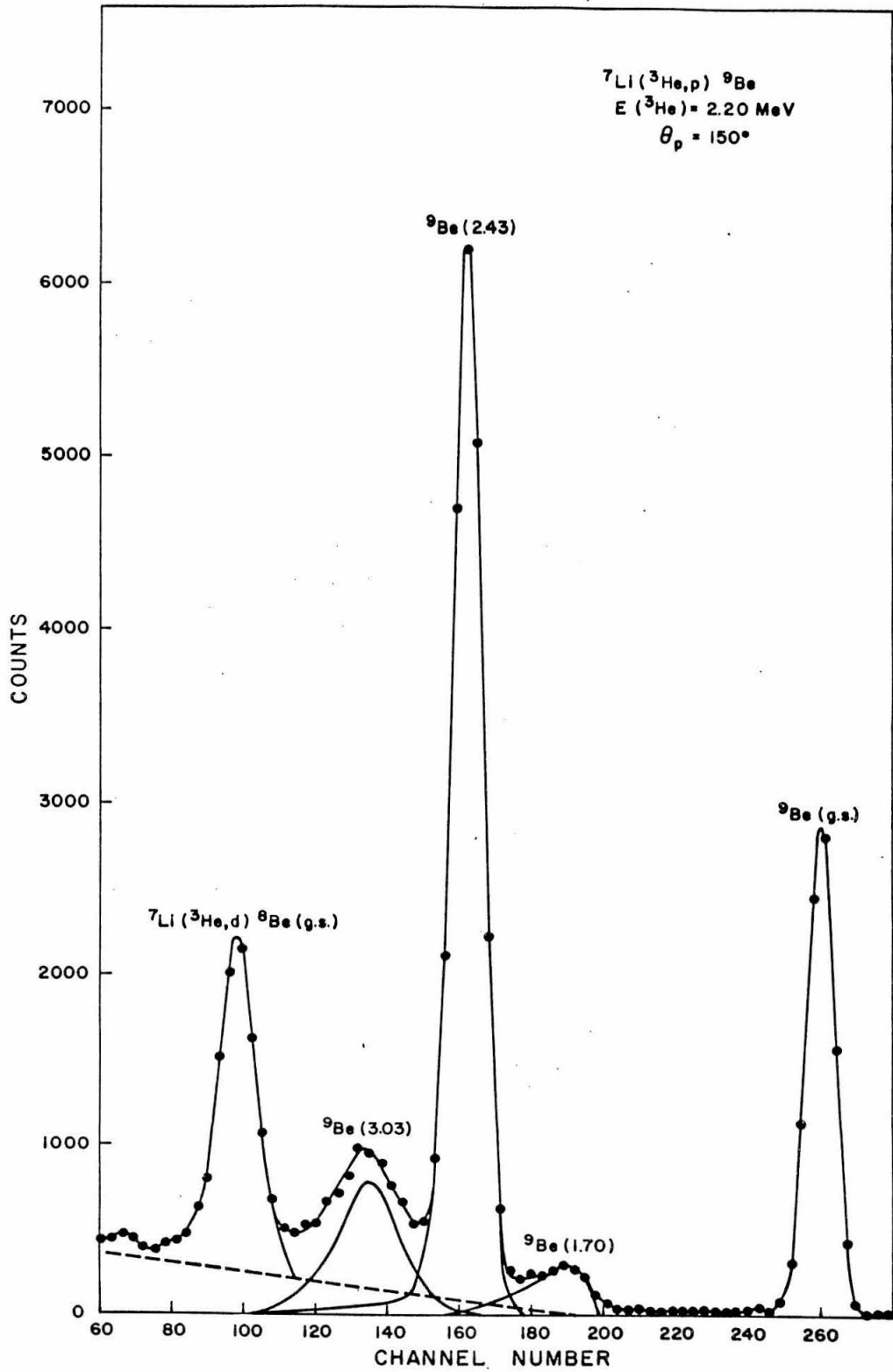
Figure 11

Figure 12

A block diagram of the electronics used in measuring
the neutron decay from the 2.43 and 3.03 MeV states of ^{9}Be
is shown. See pages 21-23.

Figure 12

130
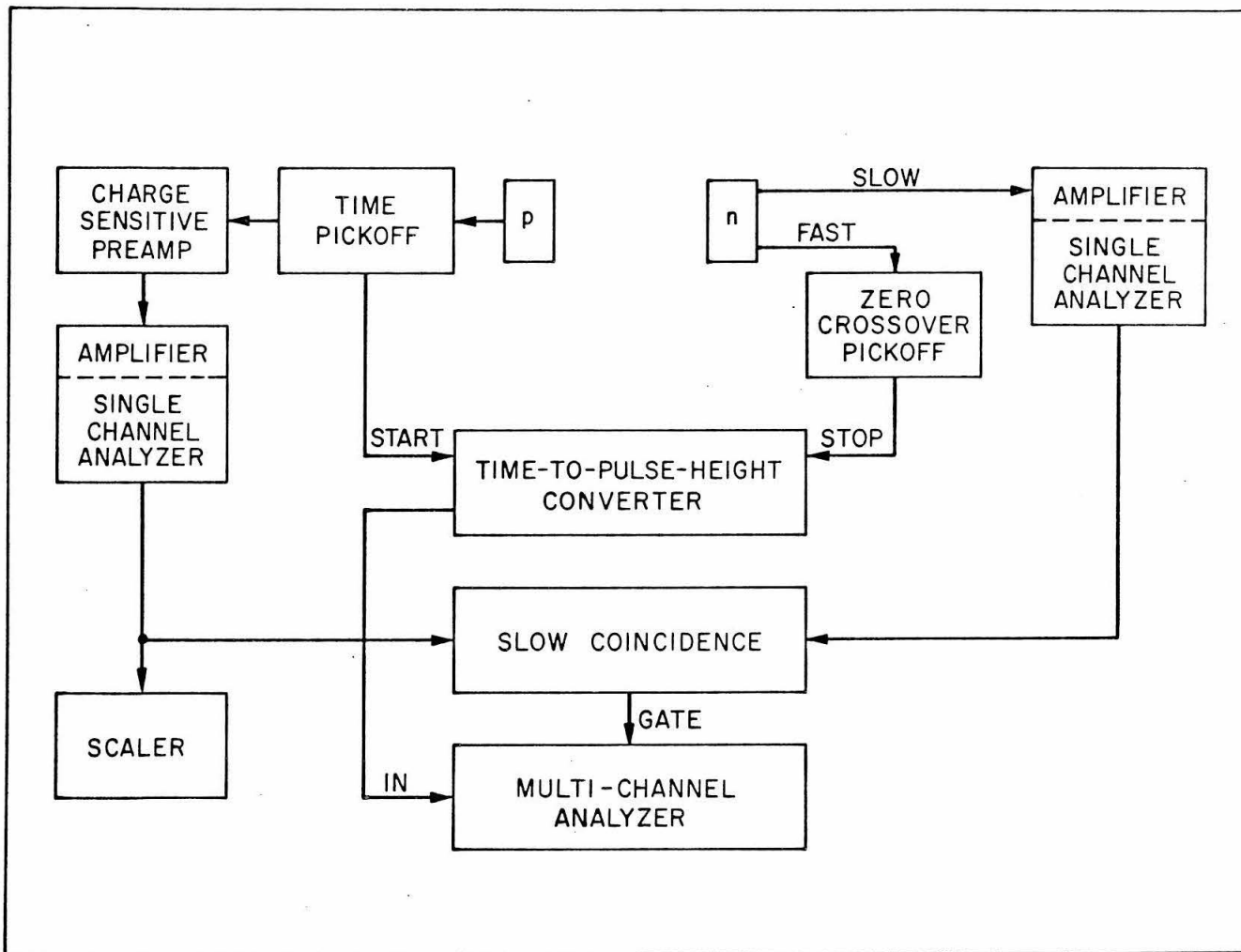
Figure 13

Measurements of the relative efficiency of the neutron detector as a function of neutron energy, using the reaction ^{3}T(p, n)^{3}He, are shown as open circles. The solid line is a theoretical curve, calculated ignoring scattering of the neutrons by carbon atoms in the scintillator, and taking the bias cutoff to occur at a neutron energy of 450 keV. The relative data points are normalized to lie on this curve at a neutron energy of 6 MeV. The point shown as a triangle represents an absolute efficiency measurement done with the reaction D(d, n)^{3}He, using a gaseous deuterium target. See pages 23 and 24.

EFFICIENCY OF NEUTRON DETECTOR

○ RELATIVE POINTS FROM $^3T(p,n)\,^3He$

△ ABSOLUTE POINT FROM $d(d,n)\,^3He$

—— $\frac{E_n-B}{E_n}(1-e^{-\sigma_H N_H L})$

DETECTOR EFFICIENCY

NEUTRON ENERGY (MeV)

Figure 13

132
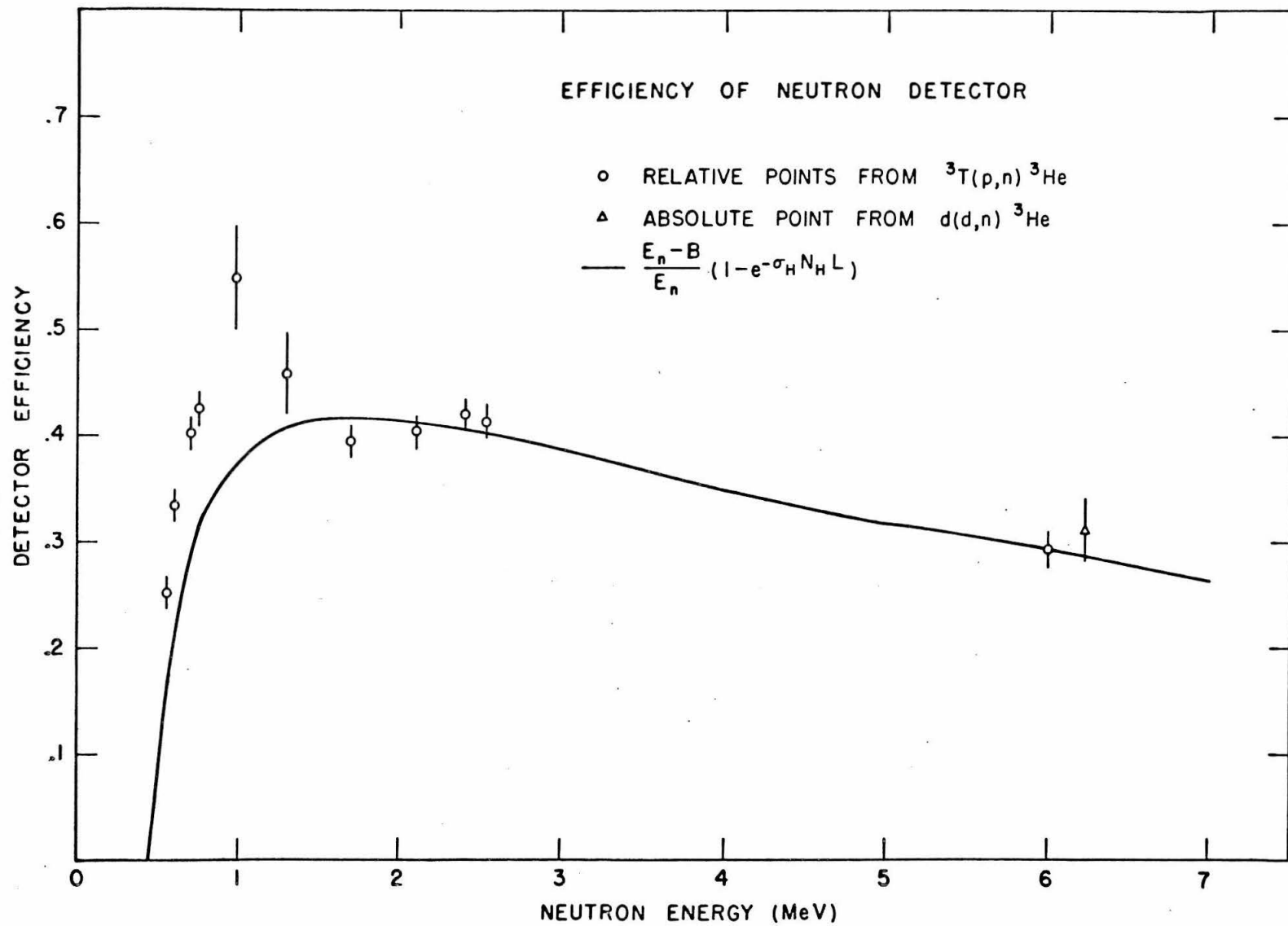
Figure 14

This neutron time-of-flight spectrum was recorded with the proton detector window accepting protons corresponding to the excitation region in ^{9}Be between 2.2 and 3.9 MeV. Groups marked 3.03 and 2.43 represent neutrons from the ^{8}Be(g. s.) decay of the 3.03 and 2.43 MeV levels in ^{9}Be. The neutron flight time corresponding to a ^{8}Be(g. s.) decay from an excitation of 3.9 MeV in ^{9}Be is marked "p-window". The broad neutron group peaking near channel 305 represents neutrons from the decay of the 2.43 MeV state in ^{9}Be via modes (2) and (3) (see text, page 18). The dashed line indicates the random time coincidence background. See pages 24 and 25.

Figure 14

134

NEUTRON TIME SPECTRUM
$^7Li(^3He,p)\ ^9Be(n)\ ^8Be$
$E\ (^3He) = 2.20\ MeV$
$\theta_p = 150°$
$\theta_n = -15.7°$
$d = 100\ cm$
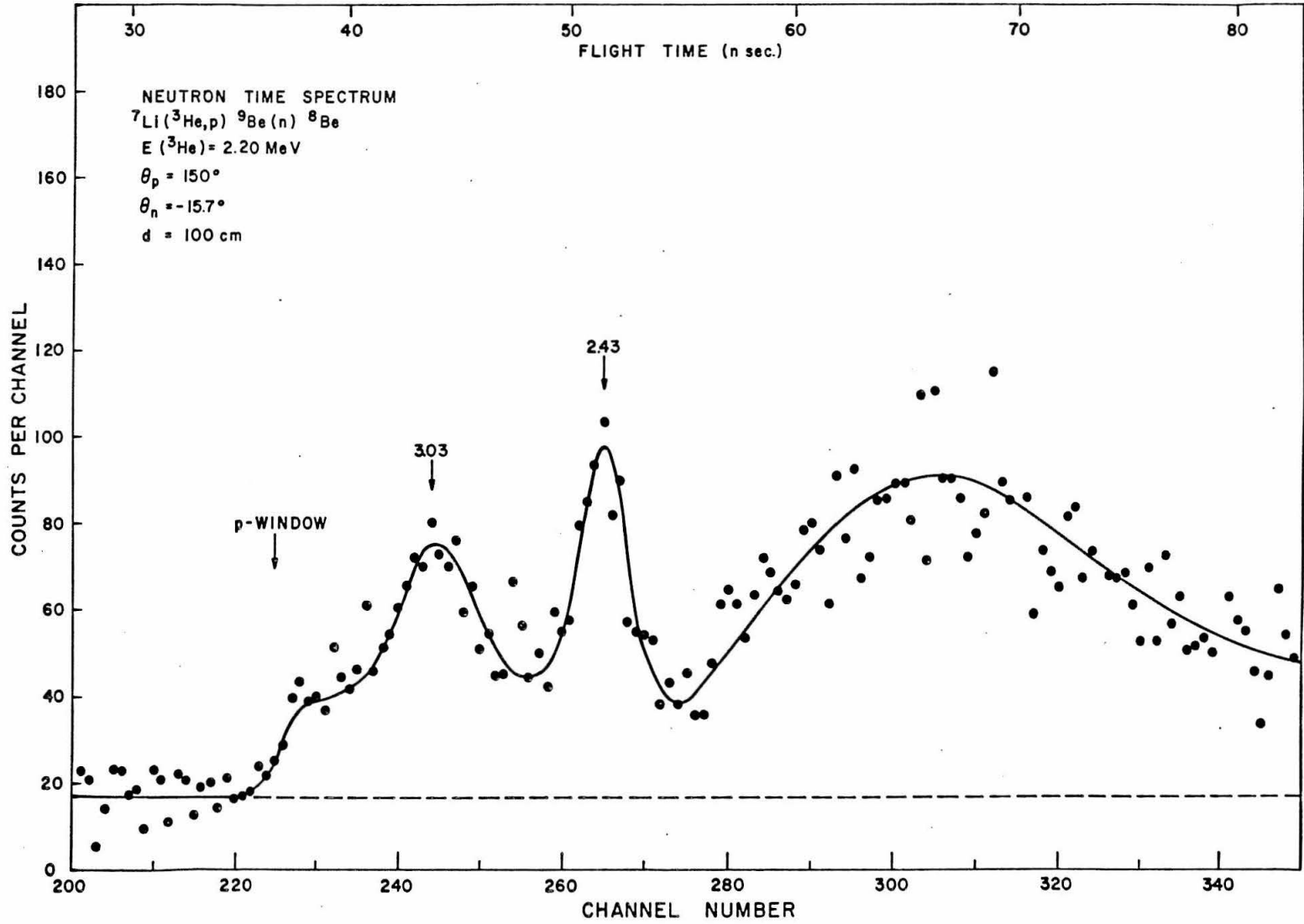
Figure 15

The time-of-flight spectrum of fig. 14 has been converted to counts per neutron energy interval <u>versus</u> neutron energy. Each point below E_n = 2.2 MeV represents an average over approximately a 50 keV interval of the corresponding points in the time spectrum, while each point above E_n = 2.2 MeV is an average of two points in the time spectrum. The upper scale refers to excitation energies in ^{9}Be if the neutron decay goes to ^{8}Be(g. s.).

Figure 15

EXCITATION IN ^{9}Be (MeV)

NEUTRON ENERGY SPECTRUM
^{7}Li(^{3}He,p)^{9}Be(n)^{8}Be
E(^{3}He) = 2.2 MeV
θ_p = 150°
θ_n = -15.7°
d = 100 cm

2.43

3.03

p-WINDOW CUTOFF

RELATIVE COUNTS PER ENERGY INTERVAL

NEUTRON ENERGY (MeV)

136

Figure 16

These neutron time-of-flight spectra were recorded with narrow proton windows. The scale above spectrum B shows corresponding excitations for ^{8}Be(g. s.) neutron decay and refers to both spectra. Each region indicated by "p-window" shows, when read on the upper scale, the region of excitation in ^{9}Be accepted by the proton window. A) The ^{9}Be(2.9 - 3.5 MeV) excitation region is seen to decay predominantly to ^{8}Be(g. s.). B) The ^{9}Be(2.17 - 2.65 MeV) excitation region decays mainly via modes (2) and (3) (see text, page 18). ^{8}Be(g. s.) decays from the ^{9}Be(2.43 MeV) state and from the tail of the ^{9}Be(3.03 MeV) state are indicated by arrows. See pages 25 and 26.

NEUTRON TIME SPECTRUM
^{7}Li(^{3}He,p)^{9}Be(n)^{8}Be
E(^{3}He) = 2.2 MeV
θ_p = 150°
θ_n = −30.7°
d = 62.5 cm
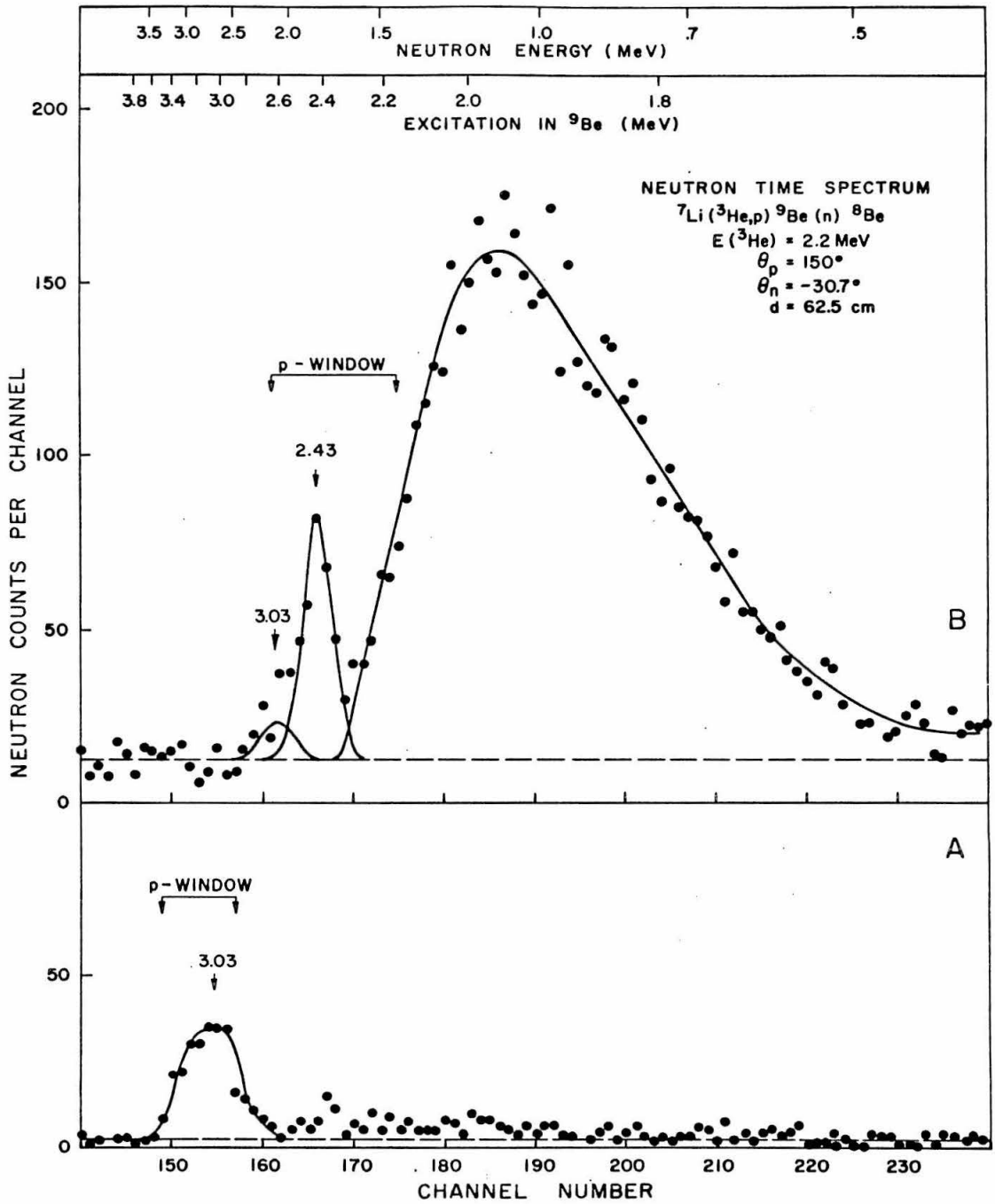
Figure 16

Figure 17

The angular distribution of neutrons from the decay of ^{9}Be(2.9 - 3.5 MeV) excitation region to ^{8}Be(g. s.) in the ^{9}Be(3.03 MeV) center-of-mass system is shown. The vertical scale is the number of neutrons per steradian per 10^3 protons in the proton window. See pages 26 and 27.

ANGULAR DISTRIBUTION OF
NEUTRONS IN ^{9}Be SYSTEM
^{7}Li (^{3}He,p) ^{9}Be(3.03) (n) ^{8}Be(g.s.)
E (^{3}He) = 2.20 MeV
θ_p = 150°
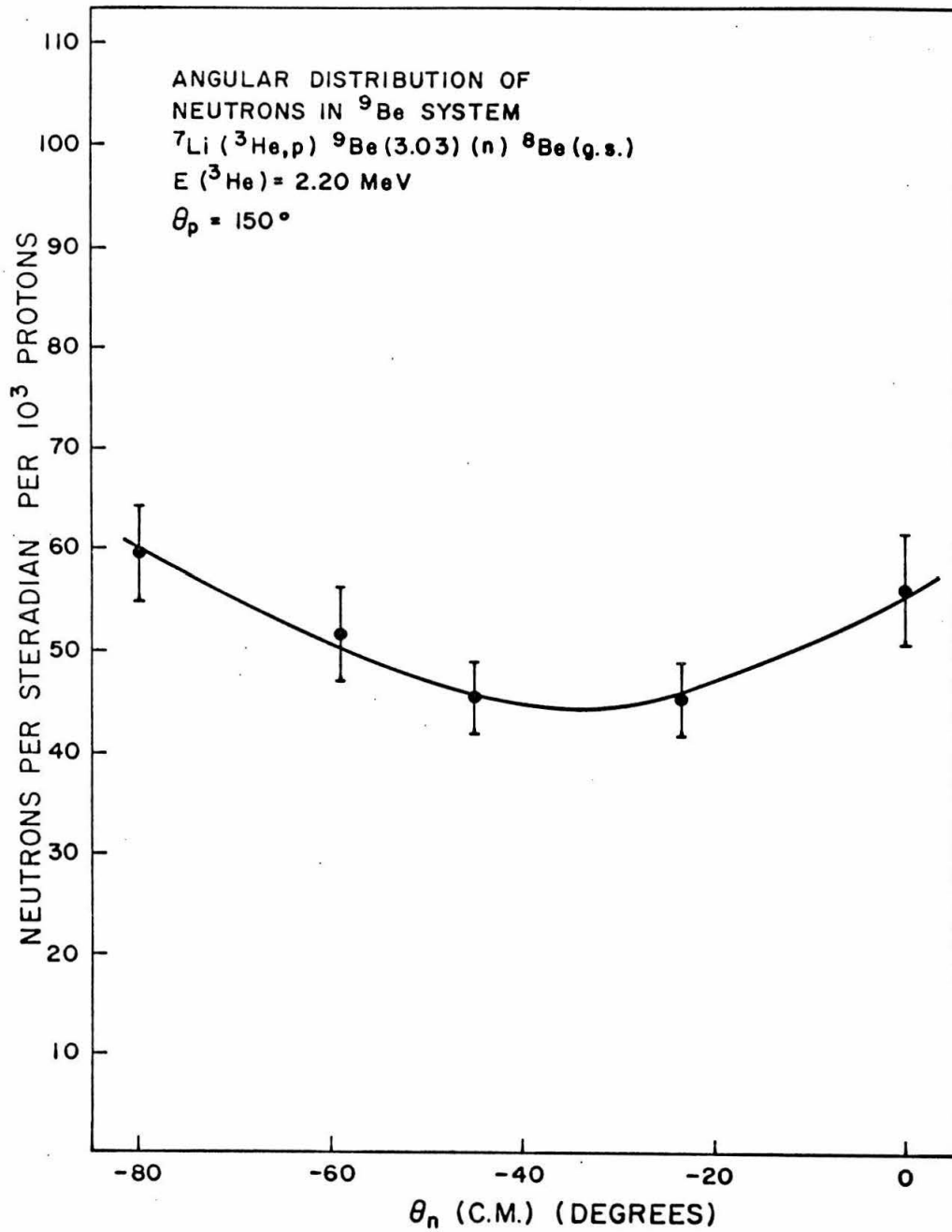
Figure 17

Figure 18

The angular distribution of neutrons from the decay of the ^{9}Be(2.43 MeV) state to ^{8}Be(g. s.) in the ^{9}Be(2.43 MeV) center-of-mass system is shown. The vertical scale is the number of neutrons per steradian per 10^3 protons leaving the ^{9}Be in its 2.43 MeV state. See page 27.

ANGULAR DISTRIBUTION OF
NEUTRONS IN ^{9}Be SYSTEM
^{7}Li (^{3}He,p) ^{9}Be(2.43) (n) ^{8}Be(g.s.)
E (^{3}He) = 2.20 MeV
θ_p = 150°
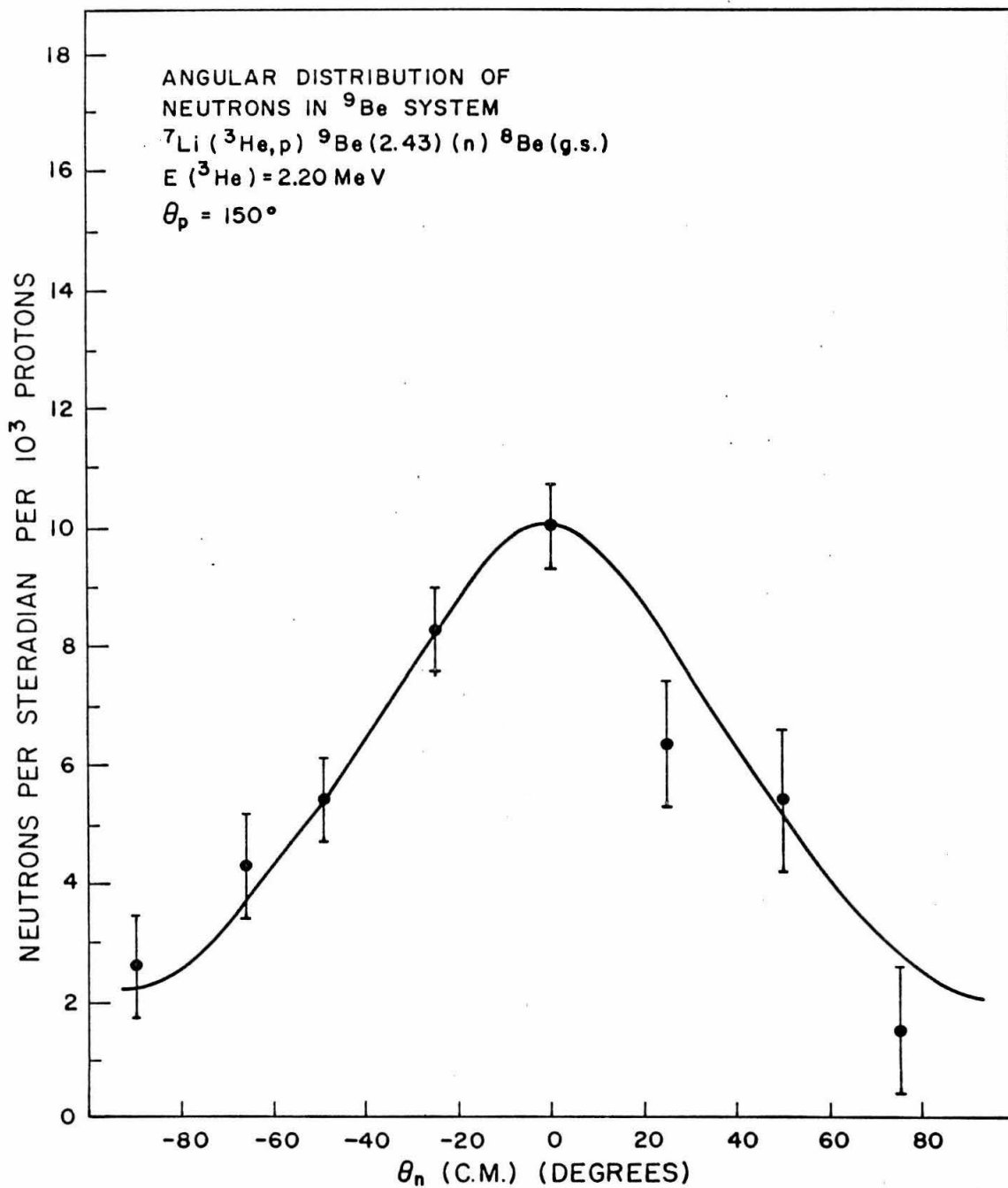
Figure 18

Figure 19

Calculated kinematic lines for the sequence ^{7}Li(^{3}He, p)^{9}Be(n)^{8}Be are presented in a proton energy versus neutron flight-time representation for cases in which the ^{8}Be is left in its ground state and in its first excited state. Excitation energies in ^{9}Be are included for convenience. Regions which are populated by the decay of levels in ^{9}Be at 2.43, 3.03, 4.65 and 6.76 MeV are denoted by their respective excitations in ^{9}Be. The regions are indicated to facilitate the discussion of the data shown in fig. 20. See pages 30, 31 for a discussion of the kinematics.

Figure 19

KINEMATICS FOR $^7Li(^3He,p)$ $^9Be(n)$ ^8Be
$\theta_{L,p} = 90°$
$\theta_{L,n} = -30°$
$E(^3He) = 10.0$ MeV

$^8Be(g.s.)$

2.43

3.03

4.65

6.76

$^8Be(2^+)$

PROTRON ENERGY (MeV)

NEUTRON FLIGHT TIME (ns/m)

EXCITATION IN ^9Be (MeV)

144
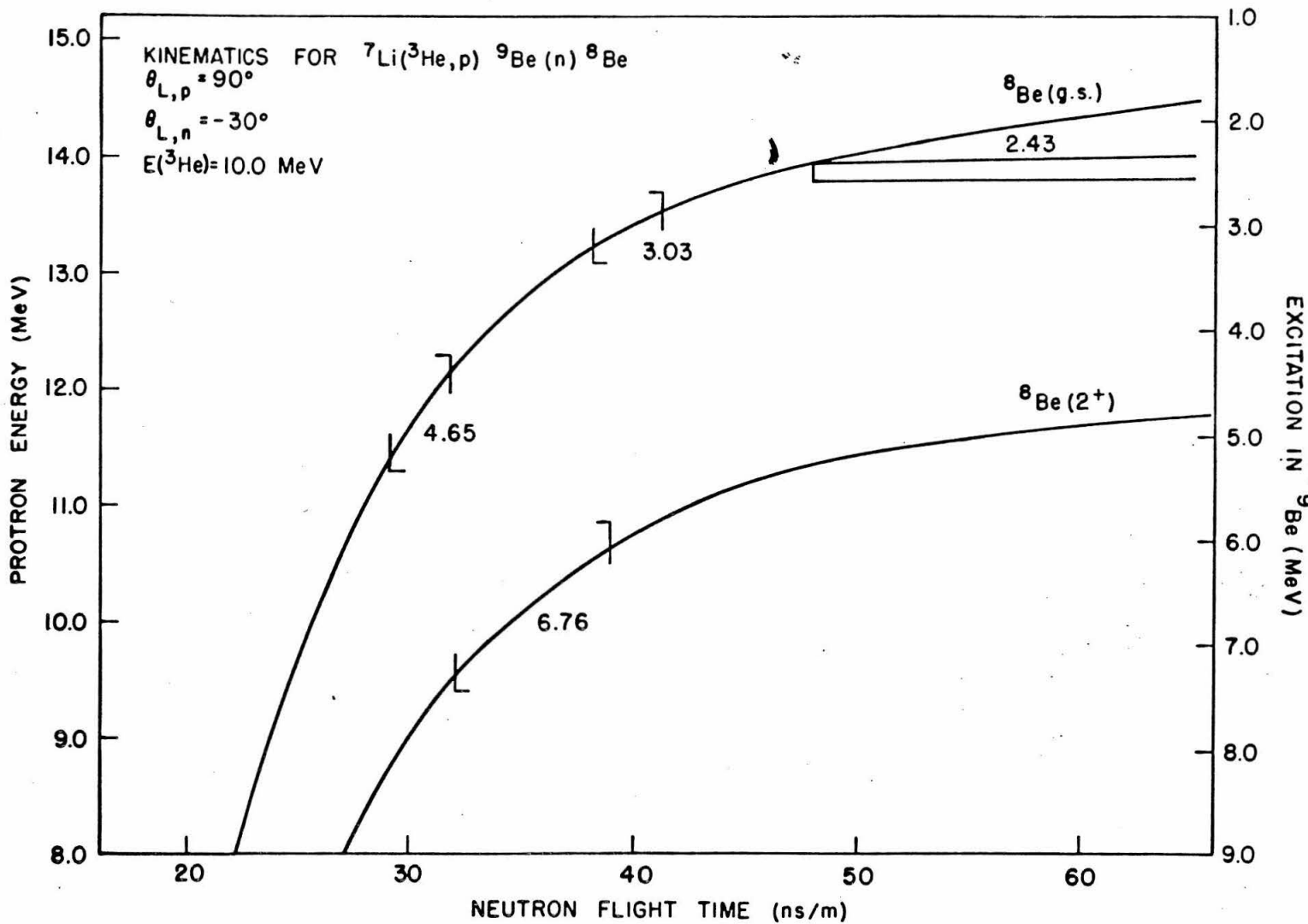
Figure 20

A sample two-dimensional coincidence spectrum taken at $\theta_{L,p} = 90^O$, $\theta_{L,n} = -30^O$, $E(^3He) = 10.0$ MeV and $d = 98$ cm is shown. The number of counts in each channel is proportional to the intensity of the spot in that channel. The decay of levels in ^9Be at 4.65 and 3.03 MeV to $^8Be(g.s.)$ appear at (31 ns, 11.8 MeV) and (40 ns, 13.4 MeV) respectively. The decay of the 6.76 MeV state in ^9Be is seen in the vicinity of (38 ns, 9.8 MeV). The decay of the 2.43 MeV state in ^9Be through the tail of $^8Be(2^+)$ and through the ground state of ^5He produces a band of neutron energies at approximately (50 - 65 ns, 13.9 MeV). The corresponding regions are indicated in fig. 19. See page 32.
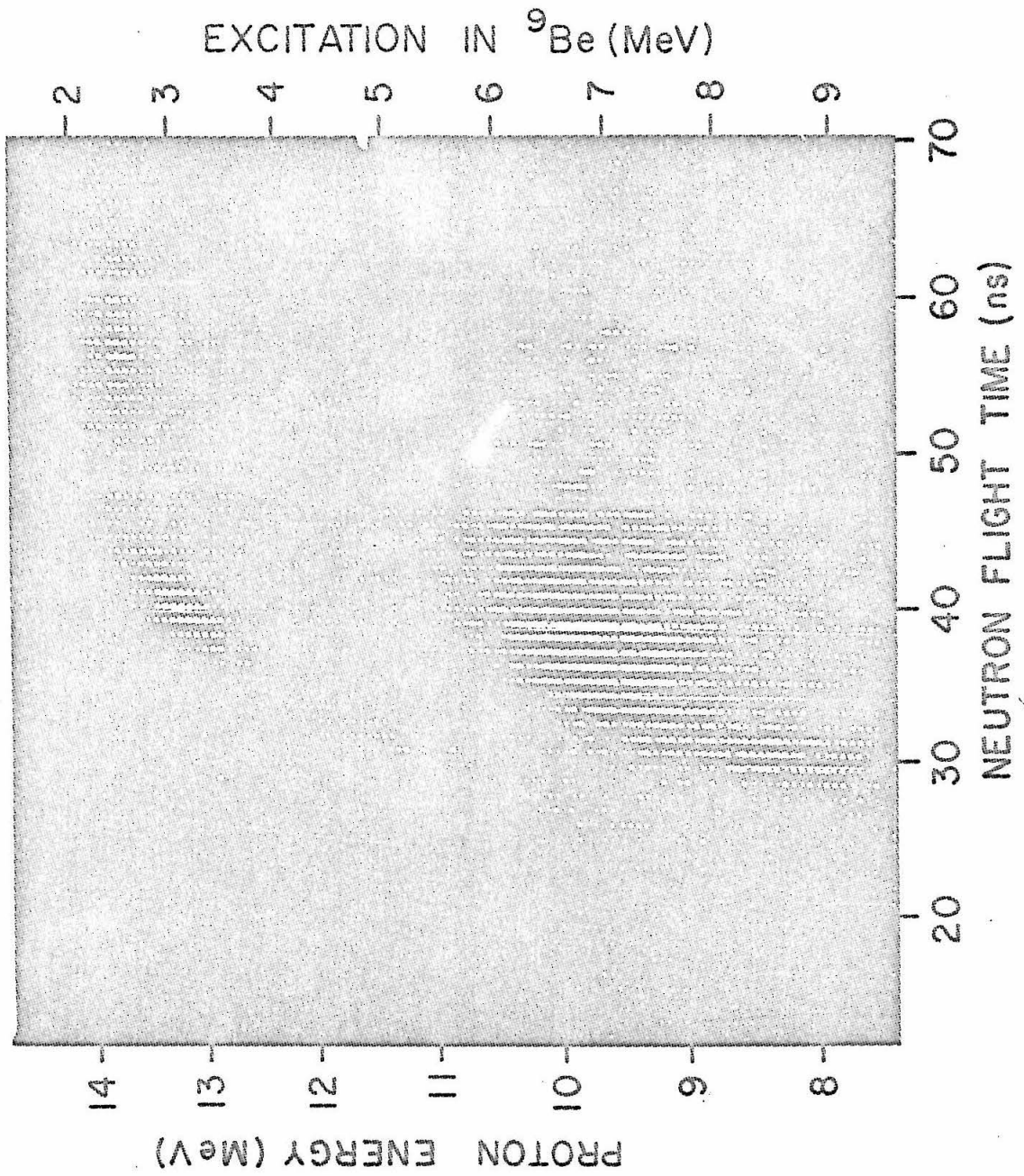
Figure 20

Figure 21

A sample charged particle singles spectrum, typical of those obtained during measurements of the branching ratio to ^{8}Be(g. s.) from the 4.65 MeV state in ^{9}Be. The particles must pass through the 0.051 mm tantalum target backing and a 0.025 mm aluminum foil en route to the 1000 μ counter. Protons populating the ground state of ^{9}Be are not stopped in the counter. Deuterons from ^{7}Li(^{3}He, d)^{8}Be(2$^+$) completely obscure the proton spectrum in the vicinity of ^{9}Be(4.65 MeV), requiring that a singles spectrum be taken with the magnetic spectrometer (fig. 22).

PARTICLE ENERGY (MeV)

PARTICLE SPECTRUM FROM ^{7}Li + ^{3}He

E (^{3}He) = 5.0 MeV

θ_L = 0°

^{7}Li(^{3}He,p) ^{9}Be(2.43 MeV)

^{7}Li(^{3}He,d) ^{8}Be(2$^+$)

^{7}Li(^{3}He,d) ^{8}Be(g.s.)

^{12}C(^{3}He,p) ^{14}N(g.s.)

COUNTS

CHANNEL NUMBER

Figure 21

148
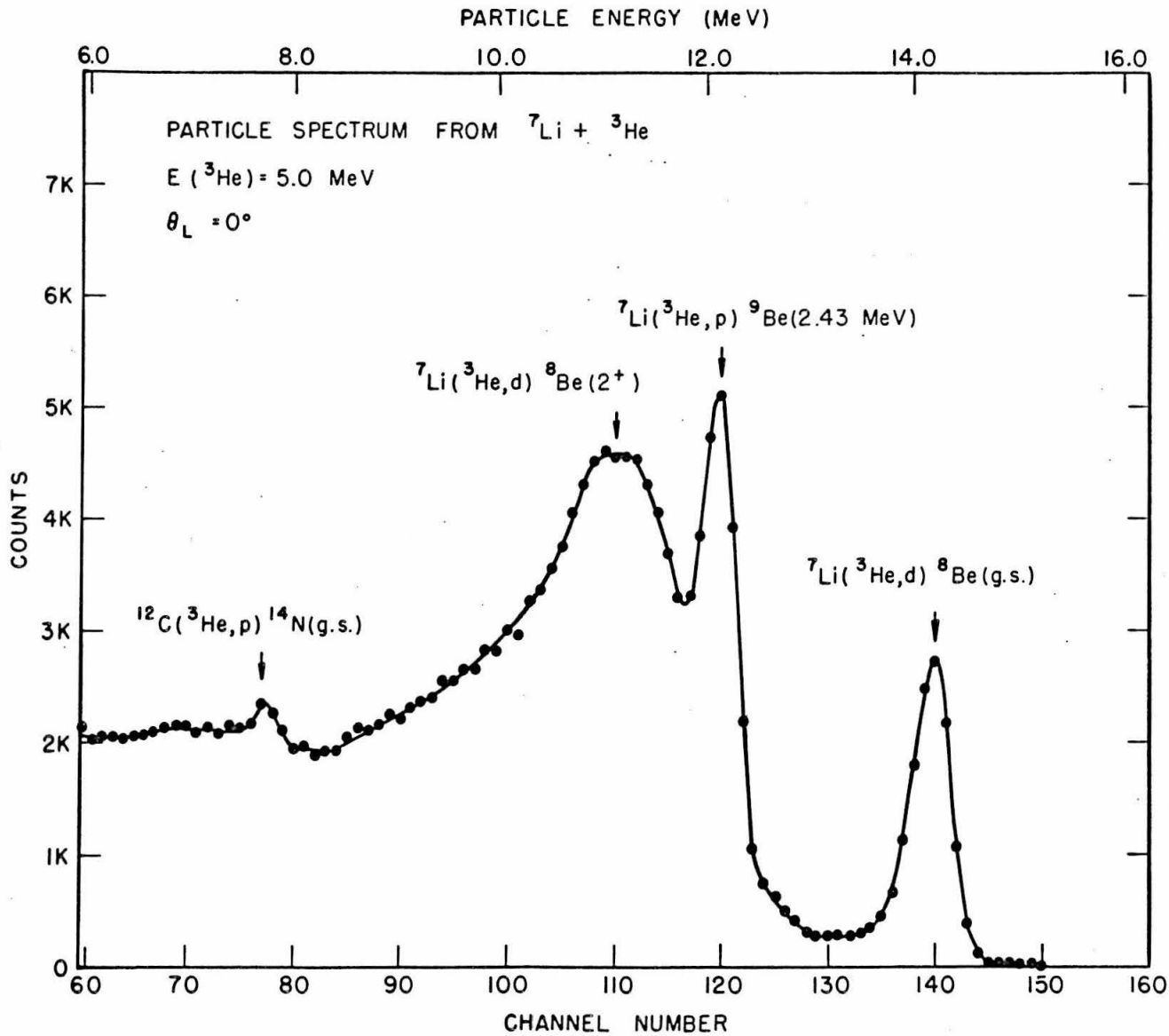
Figure 22

This proton spectrum from the magnetic spectrometer was taken at the same bombarding angle and energy as was that shown in fig. 21. The number of times the 4.65 MeV state in ^{9}Be was populated was derived from this spectrum. The proton yield from the 2.43 MeV state in ^{9}Be was used to normalize this spectrum to that of fig. 21. The solid line beneath the proton group from the 4.65 MeV level in ^{9}Be represents the background necessary to leave the width and excitation of this group as 900 keV and 4.65 MeV respectively, if a Breit-Wigner line shape (eq. 34, 1) is assumed for the level. This background was used in determining the proton yield from the state. See pages 33 and 34.

Figure 22

$^7Li(^3He,p)^9Be$

$\theta_p = 0°$

$E(^3He) = 5.0$ MeV

$^{14}N(0.0)$

^9Be (4.65)

$\times \frac{1}{2}$

RELATIVE PROTON COUNTS

NMR FREQ (Mc/s)

150
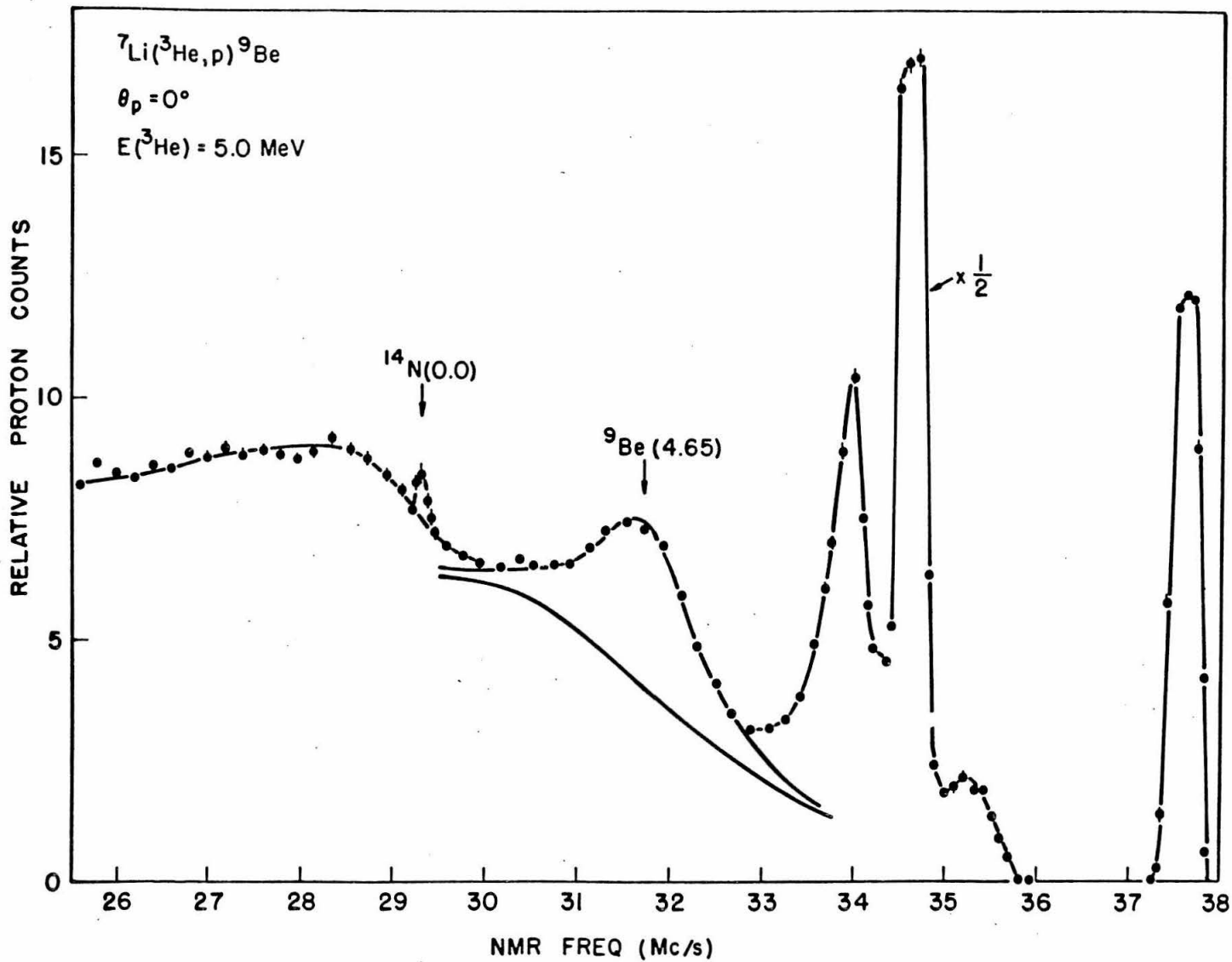
Figure 23

The time spectrum corresponding to neutron decay from an excitation region at 4.75 MeV in ^{9}Be is shown. This spectrum is taken from a two-dimensional coincidence spectrum, and corresponds to a single proton channel. The peak in channel 22 represents neutron decay to ^{8}Be(g.s.). The sum along the ^{8}Be(g.s.) line was made by measuring the number of counts in this peak as a function of proton channel. See pages 33 and 34.

FLIGHT TIME (n sec)

$^7\mathrm{Li}\,(^3\mathrm{He},\,p)\,^9\mathrm{Be}\,(4.75\ \mathrm{MeV})\,(n)$

$E(^3\mathrm{He}) = 5.0\ \mathrm{MeV}$

$\theta_{L,p} = 0°$ $E(p) = 11.422$

$\theta_{L,n} = 60°$ $d = 23.9\ \mathrm{cm}$

COUNTS PER CHANNEL
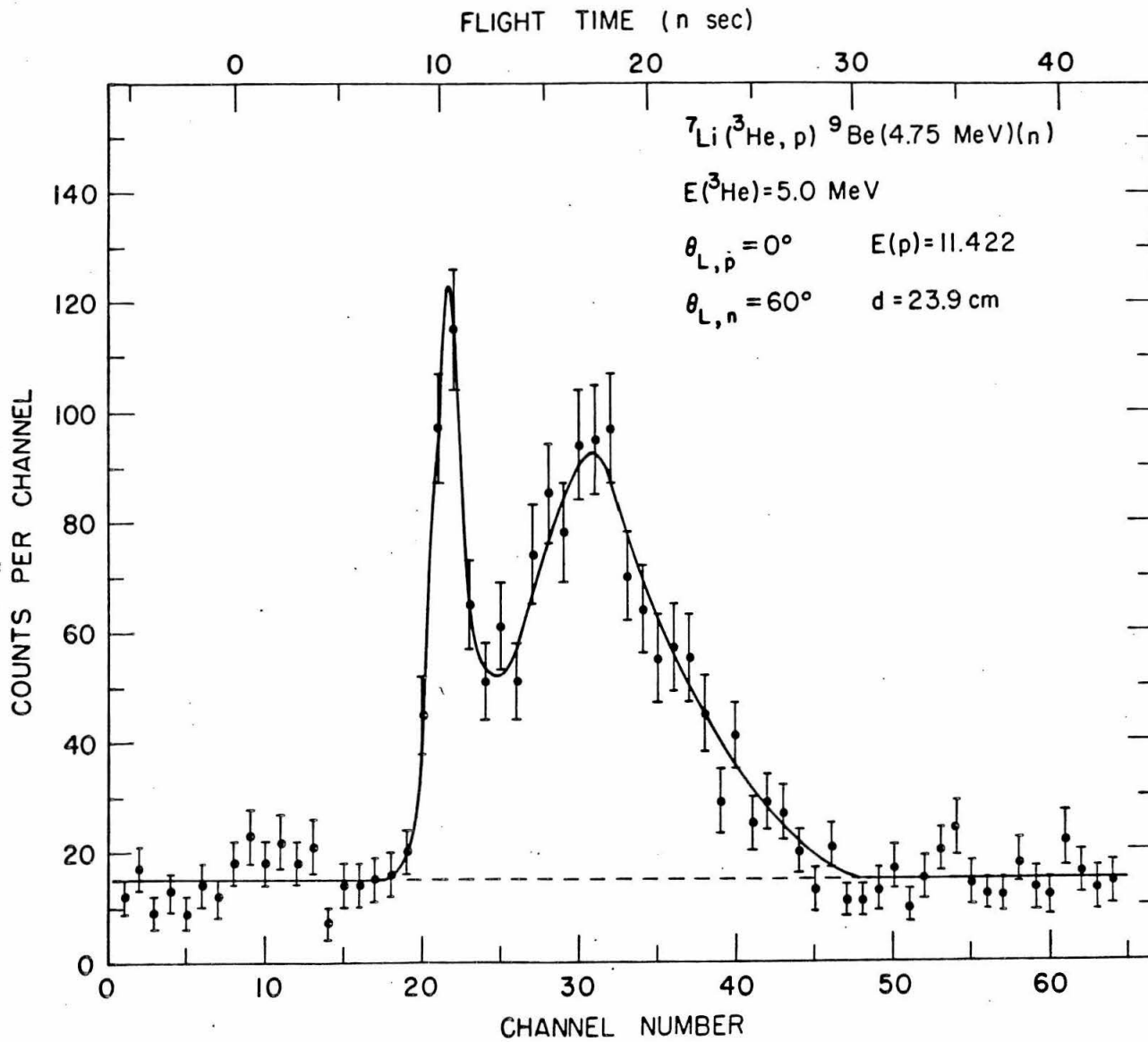
CHANNEL NUMBER

Figure 23

Figure 24

An example of the spectra obtained by summing along the ^{8}Be(g. s.) kinematic line is shown. The number of counts per proton channel in the ^{8}Be(g. s.) peak is plotted as a function of proton channel number. Neutron decay to ^{8}Be(g. s.) from states in ^{9}Be at 3.03 MeV and 4.65 MeV produces resonant groups along the ^{8}Be(g. s.) kinematic line. The solid curve through the data points in the vicinity of the ^{9}Be(4.65 MeV) group has a Breit-Wigner shape (eq. 34, 1) with width and excitation in ^{9}Be of 900 keV and 4.65 MeV respectively. The solid curve below the data points indicates the assumed background. The total ^{8}Be(g. s.) neutron yield from ^{9}Be(4.65 MeV) at $\theta_{L,n}$ = 60 was determined by measuring the number of counts in this peak. See pages 33 and 34.

^{8}Be(g.s.) YIELD FROM
^{7}Li(^{3}He, p) ^{9}Be (n) ^{8}Be(g.s.)
$\theta_{L,p} = 0°$
$\theta_{L,n} = 60°$
E(^{3}He) = 5.0 MeV

^{9}Be (3.03)

^{9}Be(4.65)

$\times \frac{1}{2}$

COUNTS

PROTON CHANNEL
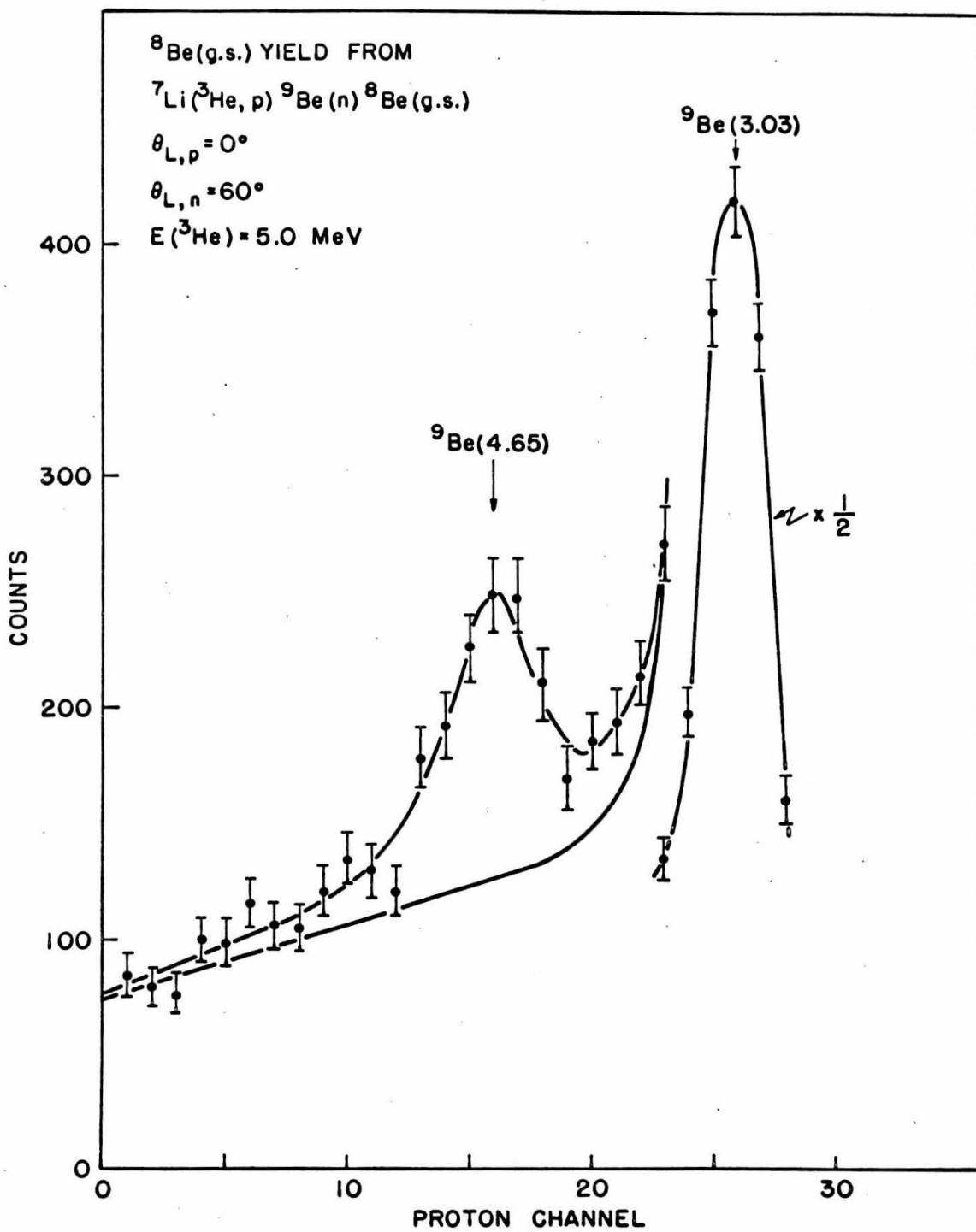
Figure 24

Figure 25

For the sequence ^{7}Li + ^{3}He → p + n + ^{8}Be(g.s.), a measurement of the outgoing neutron and proton angles leaves the determination of only one remaining independent variable necessary to provide enough information to calculate the final vector velocities of all three particles. If this variable is taken to be the excitation in ^{9}Be, the corresponding excitation in ^{9}B can be calculated. The resulting plots of excitation in ^{9}B as a function of excitation in ^{9}Be are shown as light solid lines for several values of the neutron angle for the kinematic conditions used in the measurement of neutron decay from ^{9}Be(4.65 MeV). The solid points show the experimental locations of the ^{9}Be(4.65 MeV) group on the ^{8}Be(g.s.) kinematic line for several neutron angles, with associated experimental errors. The apparent excitation of this group remains sufficiently constant for $\theta_{L,n} \leq 90^\circ$ to lend confidence to the interpretation of the group as coming from a single level in ^{9}Be. For $\theta_{L,n} \geq 90^\circ$, the apparent excitation falls, giving rise to the suspicion that the group may be receiving contributions from a level in ^{9}B in the vicinity of 9.5 MeV. Points in the backward hemisphere were accordingly excluded in calculating the branching ratio. See pages 34 and 35.

LOCATION OF ^{9}Be(4.65 MeV) GROUP
FROM ^{7}Li + ^{3}He $\rightarrow$ p + n + ^{8}Be (g.s.)
E(^{3}He) = 5.0 MeV
$\theta_{L,p} = 0°$

$\theta_{L,n} = 30°$

$\theta_{L,n} = 60°$

$\theta_{L,n} = 90°$

$\theta_{L,n} = 120°$

EXCITATION IN ^{9}B (MeV)

EXCITATION IN ^{9}Be (MeV)
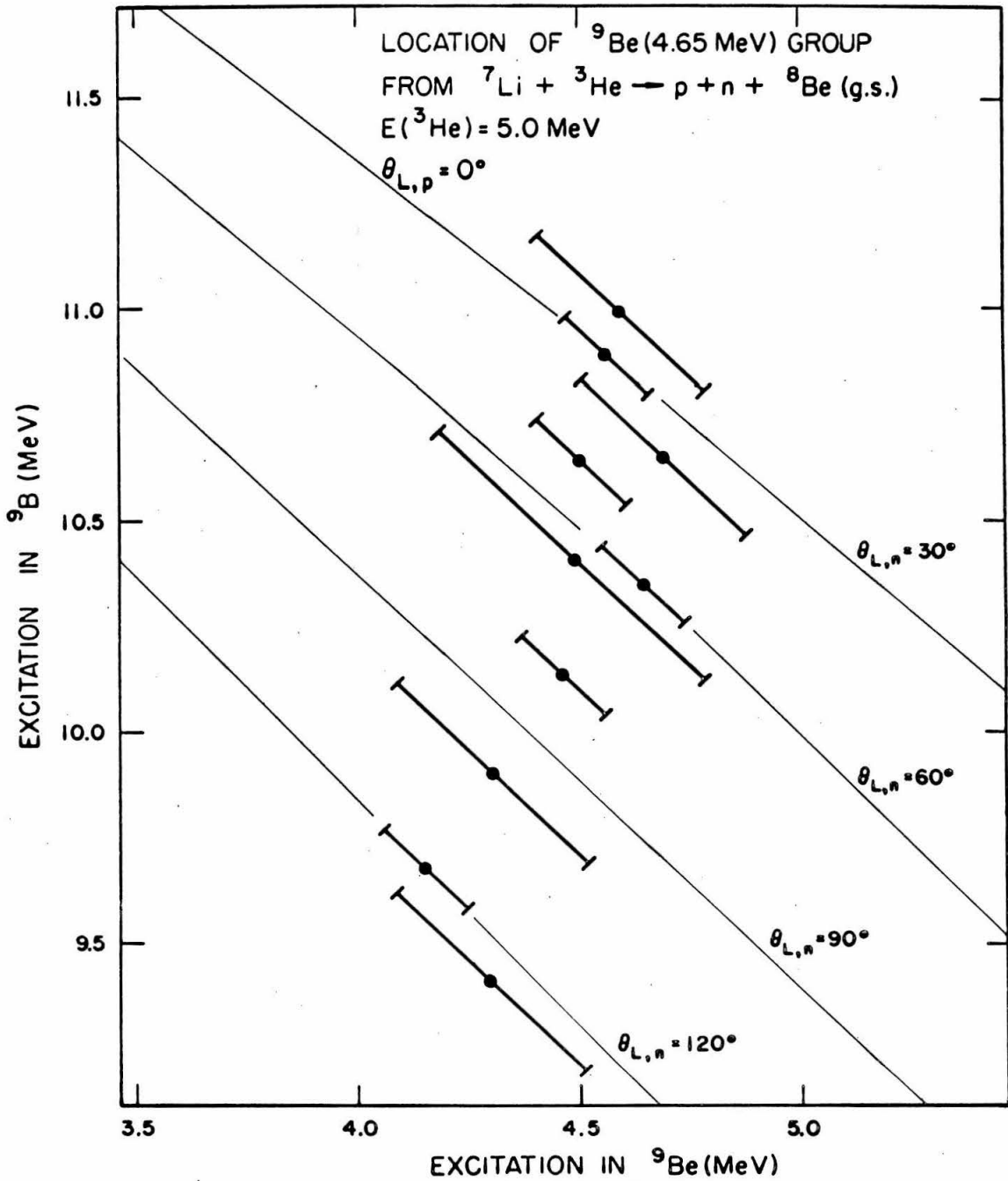
Figure 25

Figure 26

The angular distribution of neutrons from the decay of the ^{9}Be(4.65 MeV) state to ^{8}Be(g. s.) in the ^{9}Be(4.65 MeV) center-of-mass system is shown. The vertical scale is the number of neutrons per steradian per 10^3 protons leaving the ^{9}Be in its 4.65 MeV state. See page 35.

ANGULAR DISTRIBUTION OF NEUTRONS
IN ^{9}Be SYSTEM
^{7}Li(^{3}He, p) ^{9}Be(4.6)(n) ^{8}Be(g.s.)
E(^{3}He) = 5.0 MeV
$\theta_{L,p} = 0°$
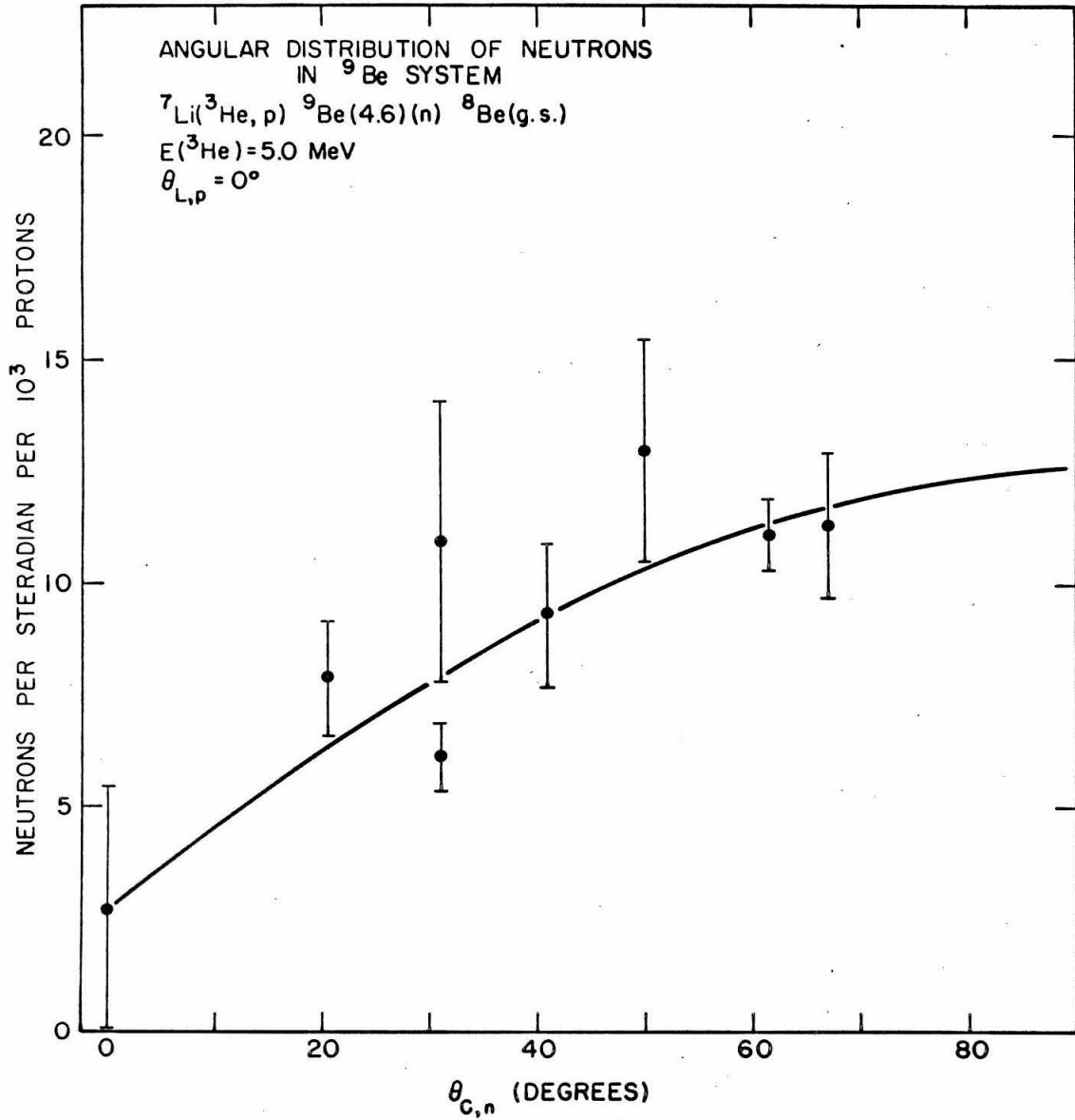
Figure 26

Figure 27

A sample surface barrier counter spectrum, typical of
those obtained in the measurement of neutron decay from
the 11.29 and 11.81 MeV states in ^{9}Be, is shown. The
particles must pass through the 0.076 mm tantalum target
backing and a 0.025 mm aluminum foil before entering the
counter. Proton groups are seen from the target con-
taminants ^{1}H (channel 65), ^{12}C (channel 136), and ^{16}O
(channel 125). The solid curve drawn through the data
points has the form of two non-interfering Breit-Wigner
resonance forms superimposed on a constant background
of 400 counts per channel. The background is due to
continuum protons and deuterons and of protons passing
through the counter. Values of the resonance parameters
used in calculating the smooth curve are compared with
those obtained from a magnetic spectrometer spectrum
at the same bombarding energy and angle in table II.
Regions denoted I-IV are discussed on page 37 . See
pages 36 and 37.

Figure 27

PARTICLE SPECTRUM FROM
^{7}Li $(^3$He,p$)$ ^{9}Be
$\theta_{L,p} = 0°$
E$(^3$He)= 10.0 MeV

^{9}Be (11.81)

^{9}Be (11.29)

H$(^3$He,p$)^3$He

^{18}F (1.7)

^{14}N (3.945)

COUNTS

I   II   III   IV

CHANNEL
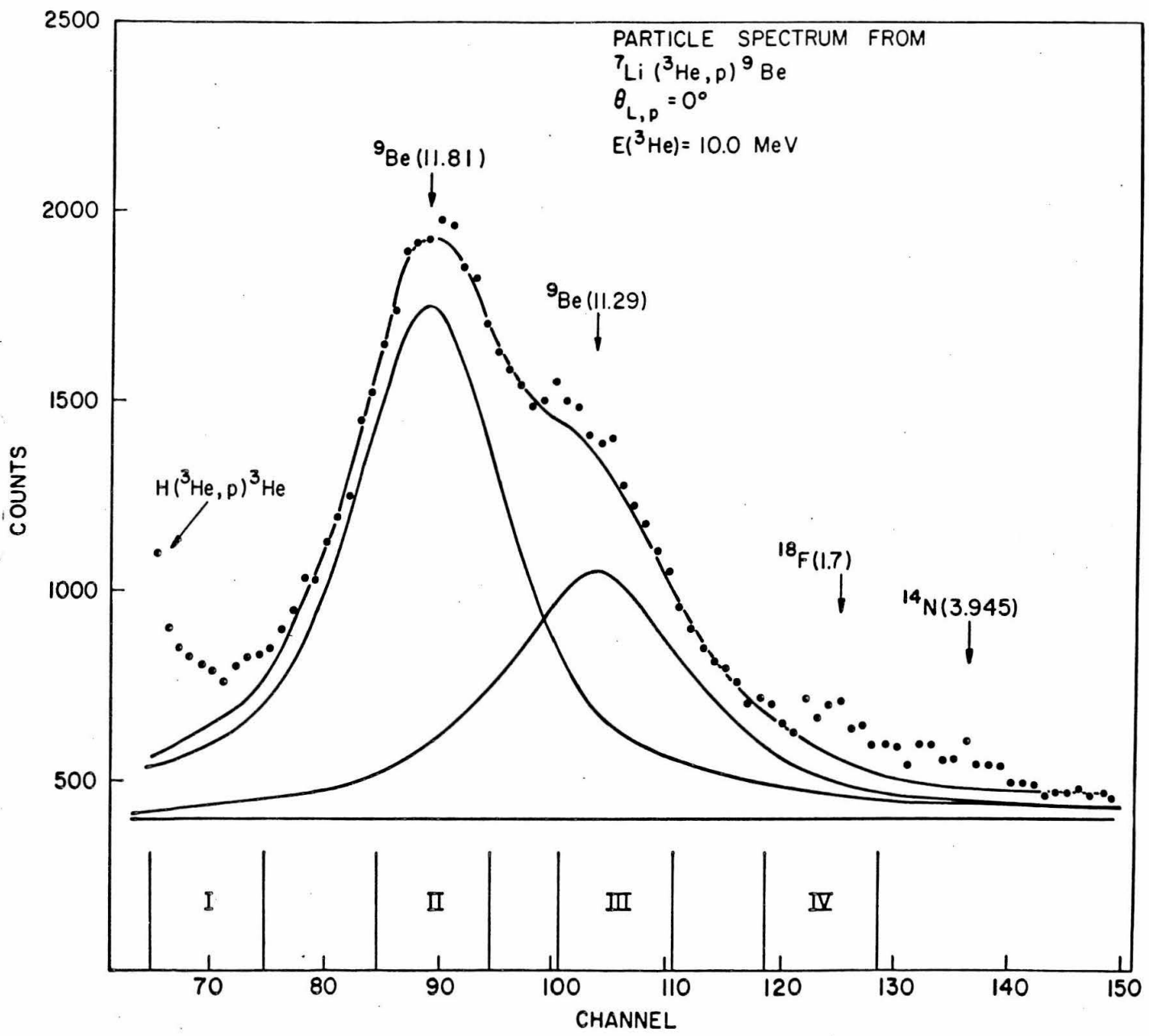
Figure 28

The raw data from a coincidence spectrum taken at $E(^3He) = 10.0$ MeV, $\theta_{L,p} = 0^O$, $\theta_{L,n} = 15^O$ and $d = 102$ cm is shown. Kinematic lines corresponding to $^8Be(g.s.)$ and $^8Be(2^+)$ decay are indicated. Random time coincidences have been subtracted. Regions I-IV correspond to excitation in ^9Be centered at approximately 12.5, 11.81, 11.25 and 10.5 MeV respectively, as indicated on the corresponding singles spectrum of fig. 27. Time spectra in these regions were added together, and the sums are shown in fig. 29. See pages 36 and 37.

SUMMED DATA LESS RANDOMS

TIME CHANNEL (INCREASING NEUTRON FLIGHT TIME ⟶)

^{8}Be(g.s.)

^{8}Be(2$^+$)

REGION I   REGION II   REGION III   REGION IV
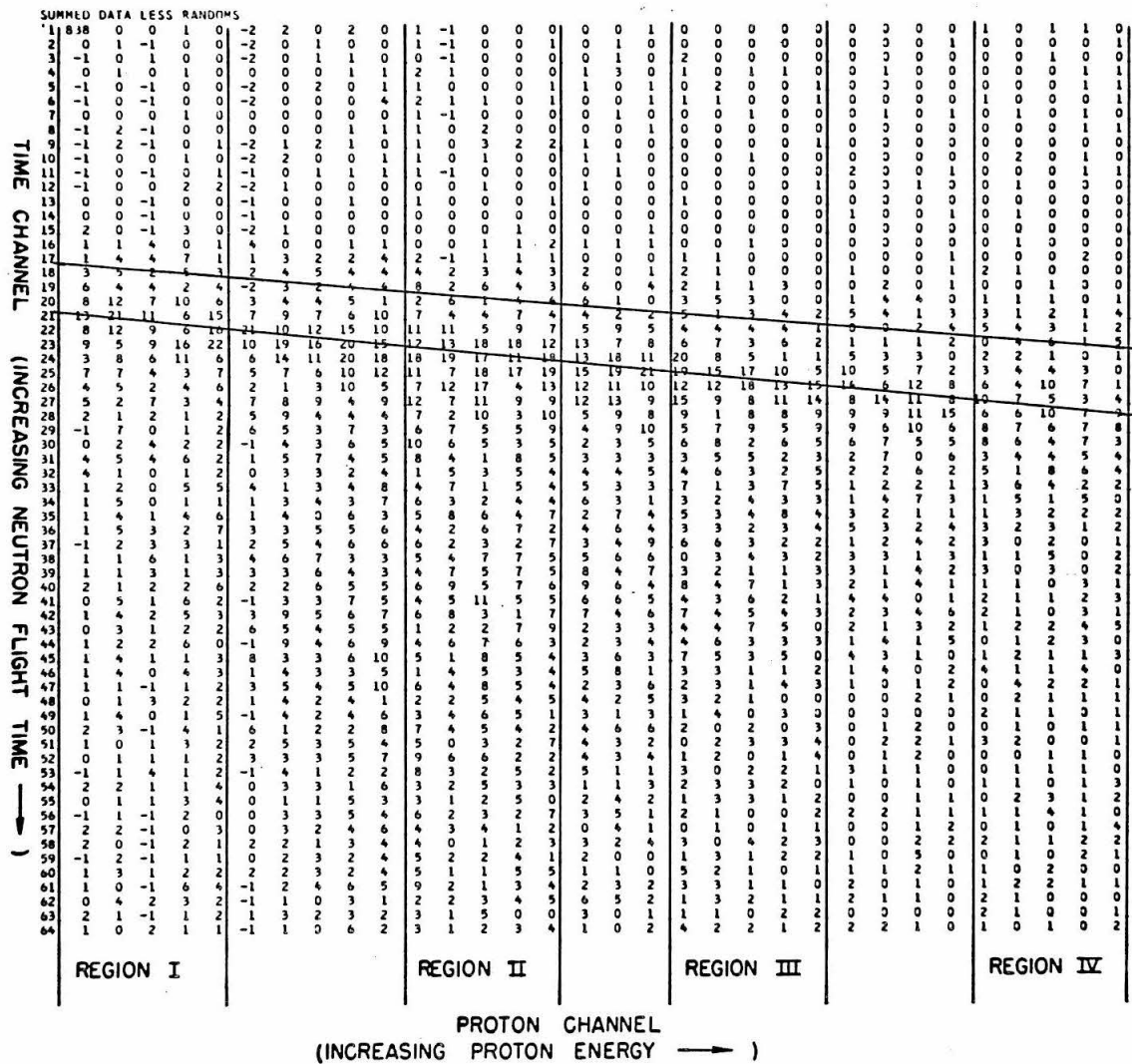
PROTON CHANNEL
(INCREASING PROTON ENERGY ⟶)

Figure 28

Figure 29

The summed time spectra from the regions indicated in fig. 28 are given. Neutron decays to ^{8}Be(g. s.) and ^{8}Be(2^+) are denoted in region I. The dashed curves represent the shapes of neutron time spectra from the sequence ^{7}Li(^{3}He, p)^{9}Be(α)^{5}He(g. s.)^{5}He, assuming isotopic breakup of ^{9}Be and ^{5}He(g. s.). Corrections for the change in detector efficiency with neutron energy were made in calculating the curves. These background shapes were used in extracting the ^{8}Be(2^+) yields from each of the four regions. See page 38.

TIME SPECTRA FROM $^7\text{Li}(^3\text{He},p)^9\text{Be}(n)$

$\theta_{L,p} = 0°$ $E(^3\text{He}) = 10.0$ .83 ns/ch

$\theta_{L,n} = 15°$ $d = 102$ cm
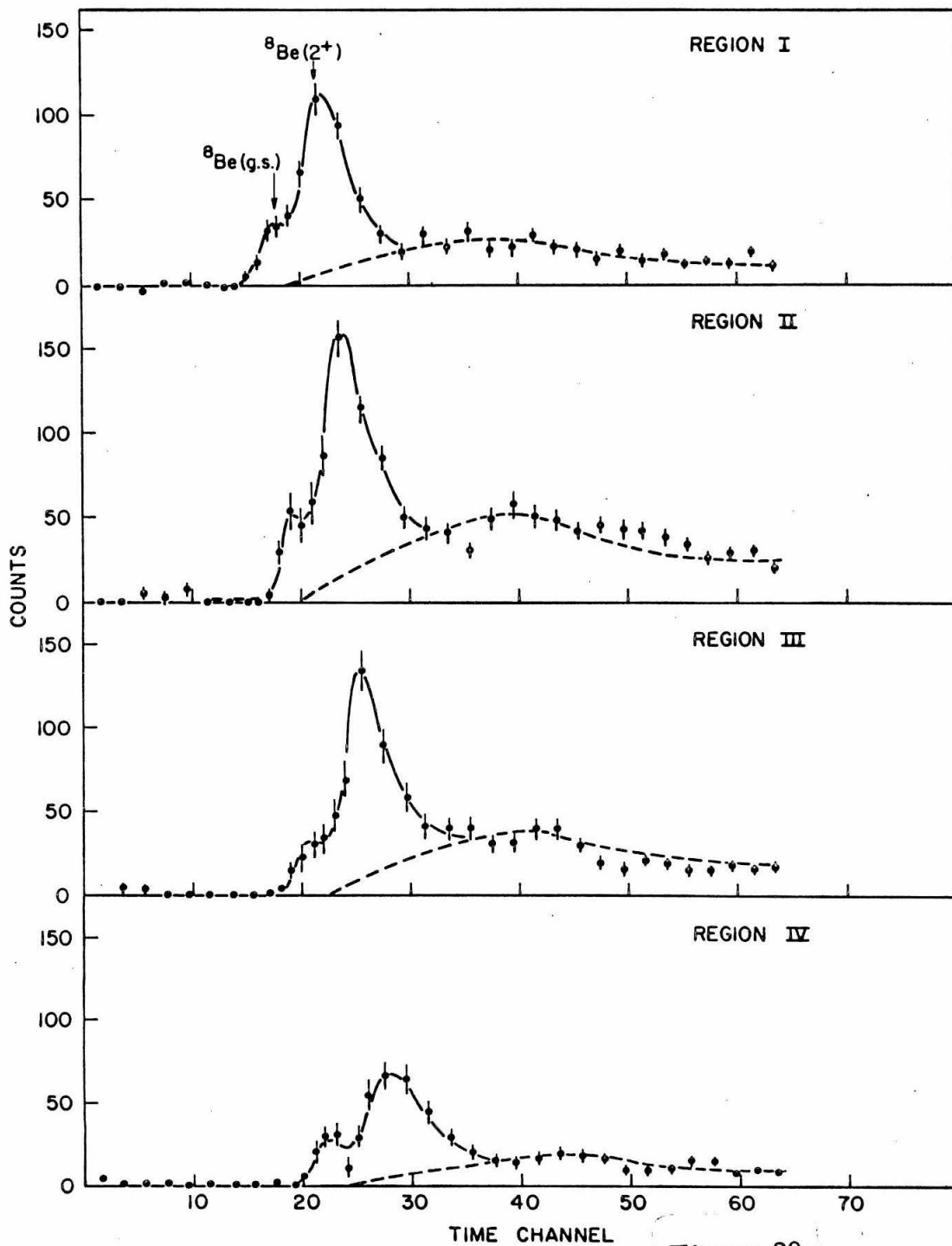
Figure 29

Figure 30

A sample time spectrum representative of neutron decay from ^{9}Be(11.29 MeV) (Region III) is given. The heavy solid curve represents the expected neutron time spectrum from the sequence ^{7}Li(^{3}He, p)^{9}Be(11.29 MeV)(α)^{5}He(g. s.) n for isotropic decays of the ^{9}Be(11.29 MeV) state and the ^{5}He(g. s.), assuming an $\ell = 2$ decay by ^{9}Be(11.29 MeV). The dashed curve is the spectrum expected from ^{7}Li(^{3}He, p)^{9}Be(11.29 MeV)(n)^{8}Be(4^+), assuming p-wave neutron emission. Corrections for the change in detector efficiency with neutron energy were made in calculating the curves. The shape of the solid curve was used in the extraction of ^{8}Be(2^+) yields. See page 38.

Figure 30
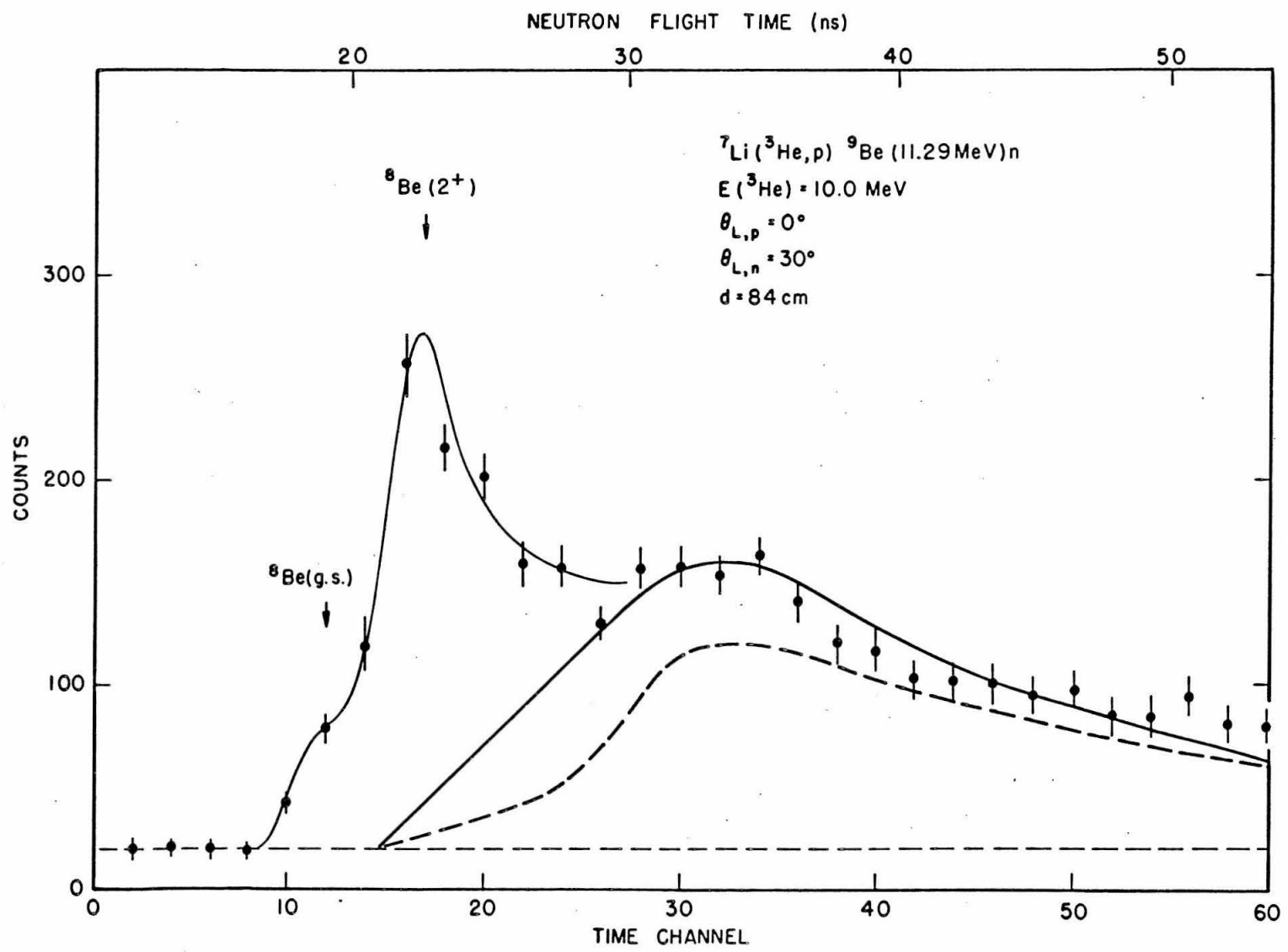
Figure 31

The angular distribution of neutrons from the decay of the ^{9}Be(11.29 MeV) state to ^{8}Be(2^+) in the ^{9}Be(11.29 MeV) center-of-mass system is shown. The vertical scale is the number of neutrons per steradian per 10^3 protons leaving the ^{9}Be in its 11.29 MeV state. See pages 38 and 39.

ANGULAR DISTRIBUTION OF NEUTRONS
IN ^{9}Be SYSTEM
^{7}Li(^{3}He,p) ^{9}Be(11.29 MeV)(n) ^{8}Be(2^+)
$\theta_{L,p} = 0°$

● E(^{3}He)= 10.0 MeV
○ E(^{3}He)= 9.0 MeV
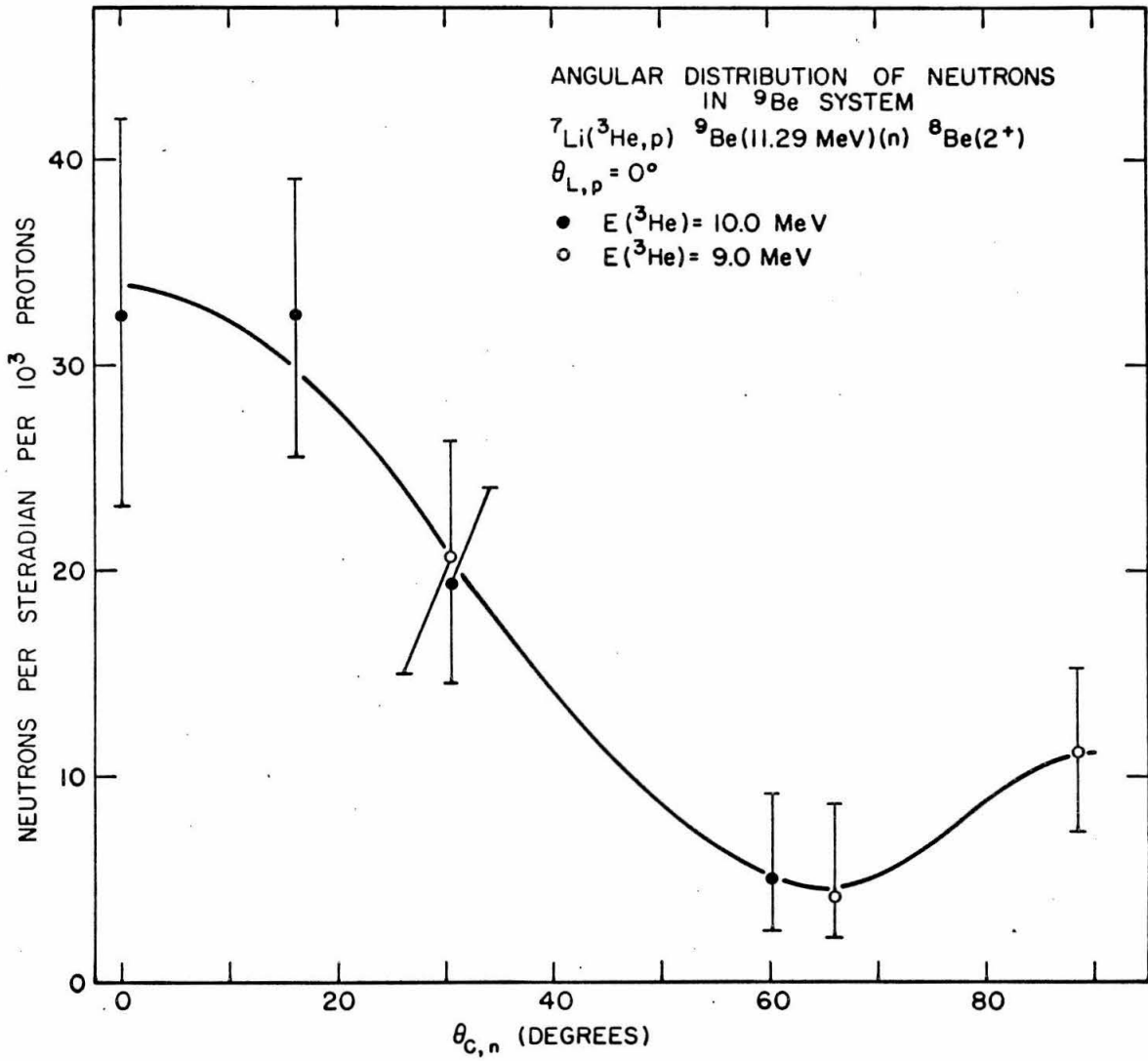
Figure 31

Figure 32

The angular distribution of neutrons from the decay of the ^{9}Be(11.81 MeV) state to ^{8}Be(2^+) in the ^{9}Be(11.81 MeV) center-of-mass system is shown. The vertical scale is the number of neutrons per steradian per 10^3 protons leaving the ^{9}Be in its 11.81 MeV state. See pages 38 and 39.
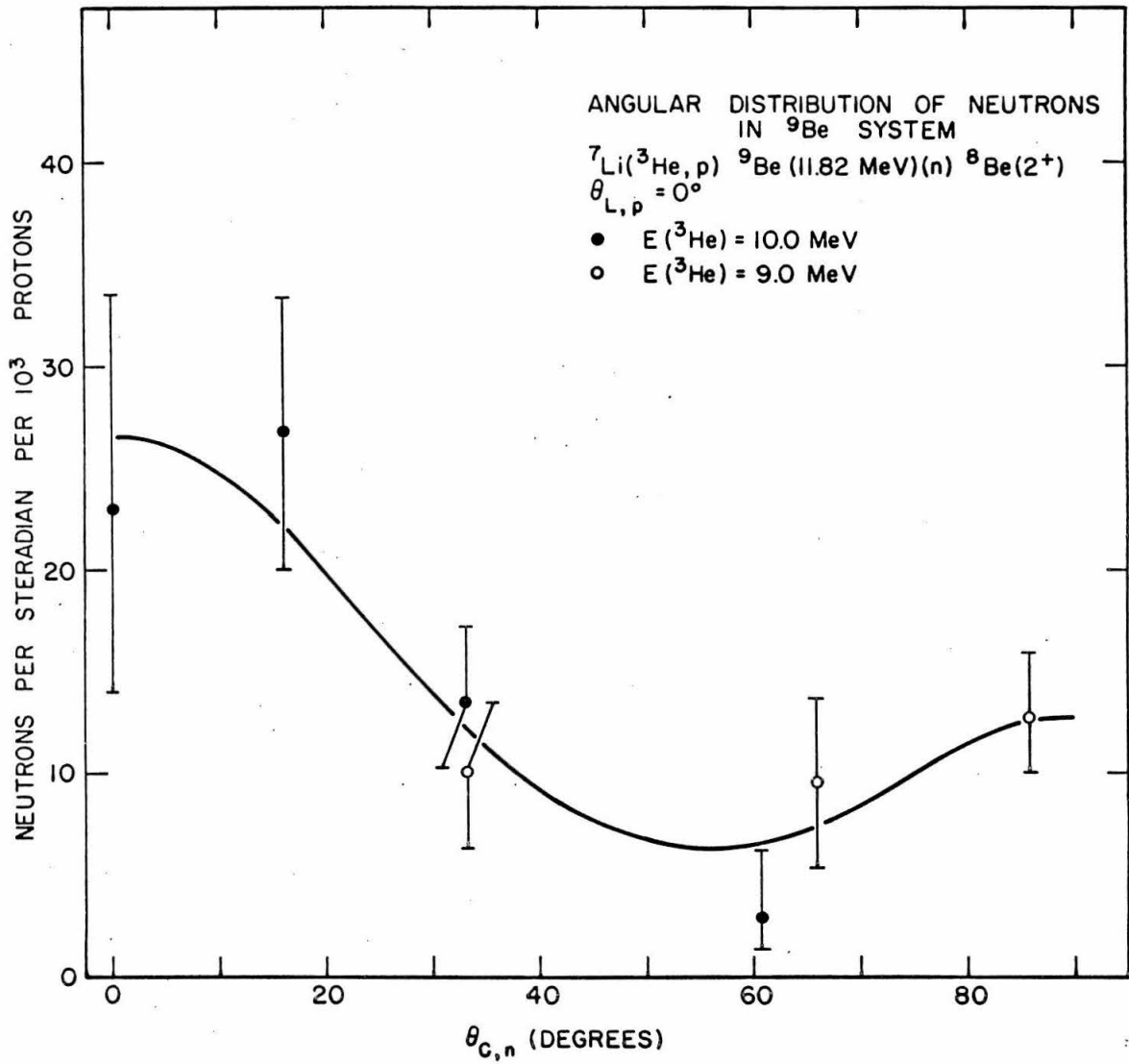
Figure 32

Figure 33

The coincidence spectrum of fig. 20 has been projected onto the proton energy axis in two pieces. Figure   A represents all events falling outside the ^{8}Be(g. s.) line. Random time coincidences have been subtracted. The large group in fig.   A corresponds to neutron decay from ^{9}Be(6.76 MeV). The solid curve through the data points has the form of a B-W. resonance (eq. (34, 1)) of width 2.3 MeV, superimposed on an assumed background shown by the dashed line. Figure B shows ^{8}Be(g. s.) decay from ^{9}Be(4.65 MeV) and ^{9}Be(3.03 MeV) groups, but no resonant behavior at ^{9}Be(6.76 MeV).
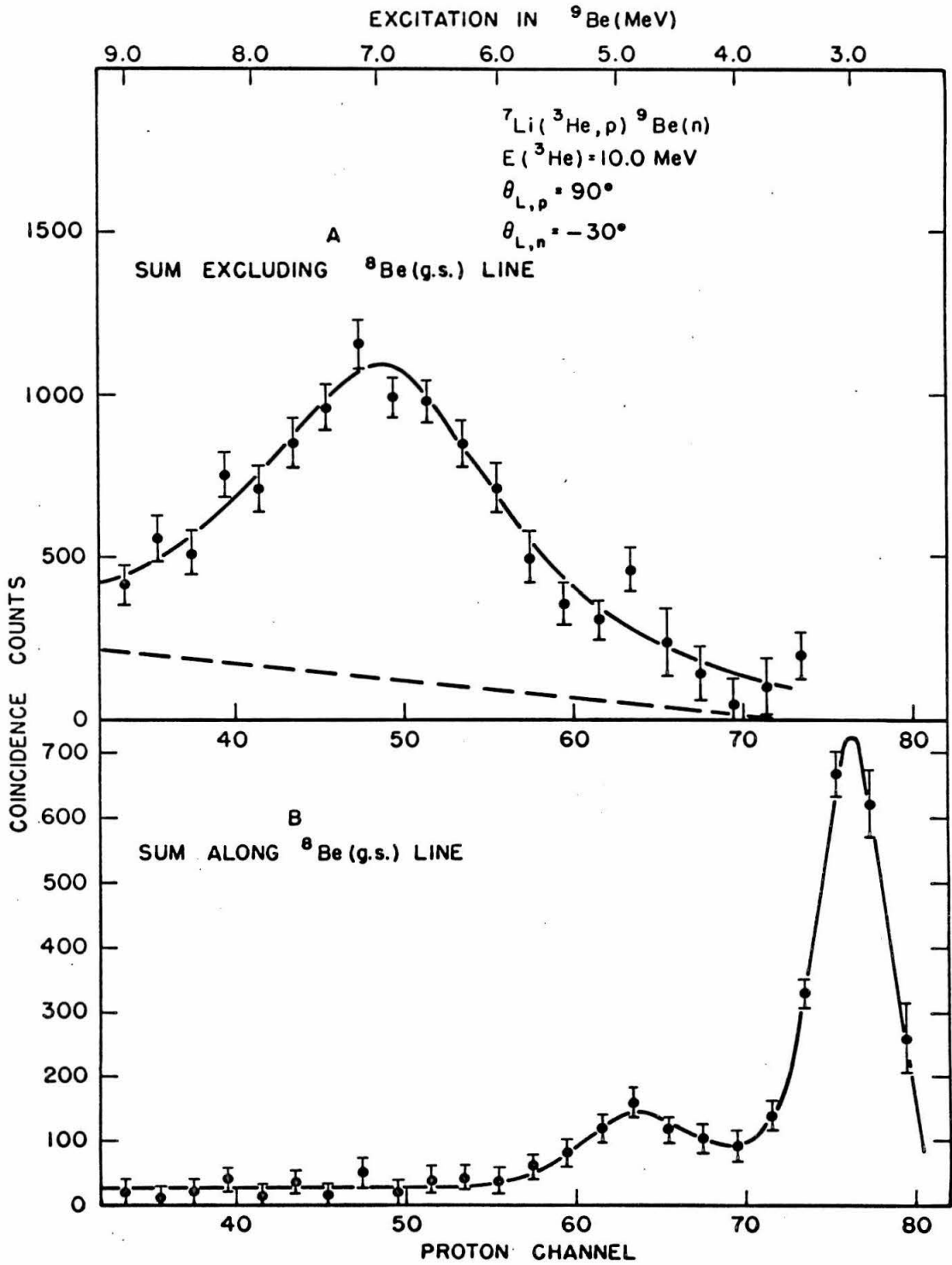
Figure 33

Figure 34

A neutron energy time spectrum corresponding to an excitation in ^{9}Be centered at 6.8 MeV is taken to represent neutron decay from the ^{9}Be(6.76 MeV) state. Figure A displays a portion of the data of fig. 20, converted to an energy spectrum in the ^{8}Be center-of-mass system; figure B displays a similar spectrum taken at a different neutron angle. The data points have been corrected for the variation of detector efficiency with neutron energy. For neutrons proceeding via ^{7}Li(^{3}He, p)^{9}Be(6.8 MeV)(n)^{8}Be(2.9 MeV), figures A and B represent neutron center-of-mass angles of 0° and 79° with respect to the ^{9}Be recoil direction. The heavy solid curves in both spectra represent shapes expected from neutron decay through ^{8}Be(2^+), folded into the experimental resolution. The dashed line in fig. A represents the expected shape from the process ^{7}Li(^{3}He, p)^{9}Be(6.8 MeV)(α)^{5}He(g. s.)(n)^{5}He, assuming isotropic decays of both ^{9}Be(6.8 MeV) and ^{5}He(g. s.). The dash-dotted curves represent expected shapes if the ^{5}He(g. s.) angular distribution is given by $W(\theta_{c,n}) = 1 + \cos^2 \theta_{c,n}$. See pages 40 and 41.

NEUTRON ENERGY SPECTRUM
IN ^{9}Be SYSTEM
^{7}Li(^{3}He, p) ^{9}Be(6.8 MeV)(n)
E(^{3}He) = 10.0 MeV
$\theta_{L,p}$ = 90°

$\theta_{L,n}$ = -30°
d = 98 cm
$\theta_{c,n}$ = 0°

A

$\theta_{L,n}$ = 25°
d = 50cm
$\theta_{c,n}$ = 79°

B

RELATIVE COUNTS PER EXCITATION INTERVAL PER STERADIAN
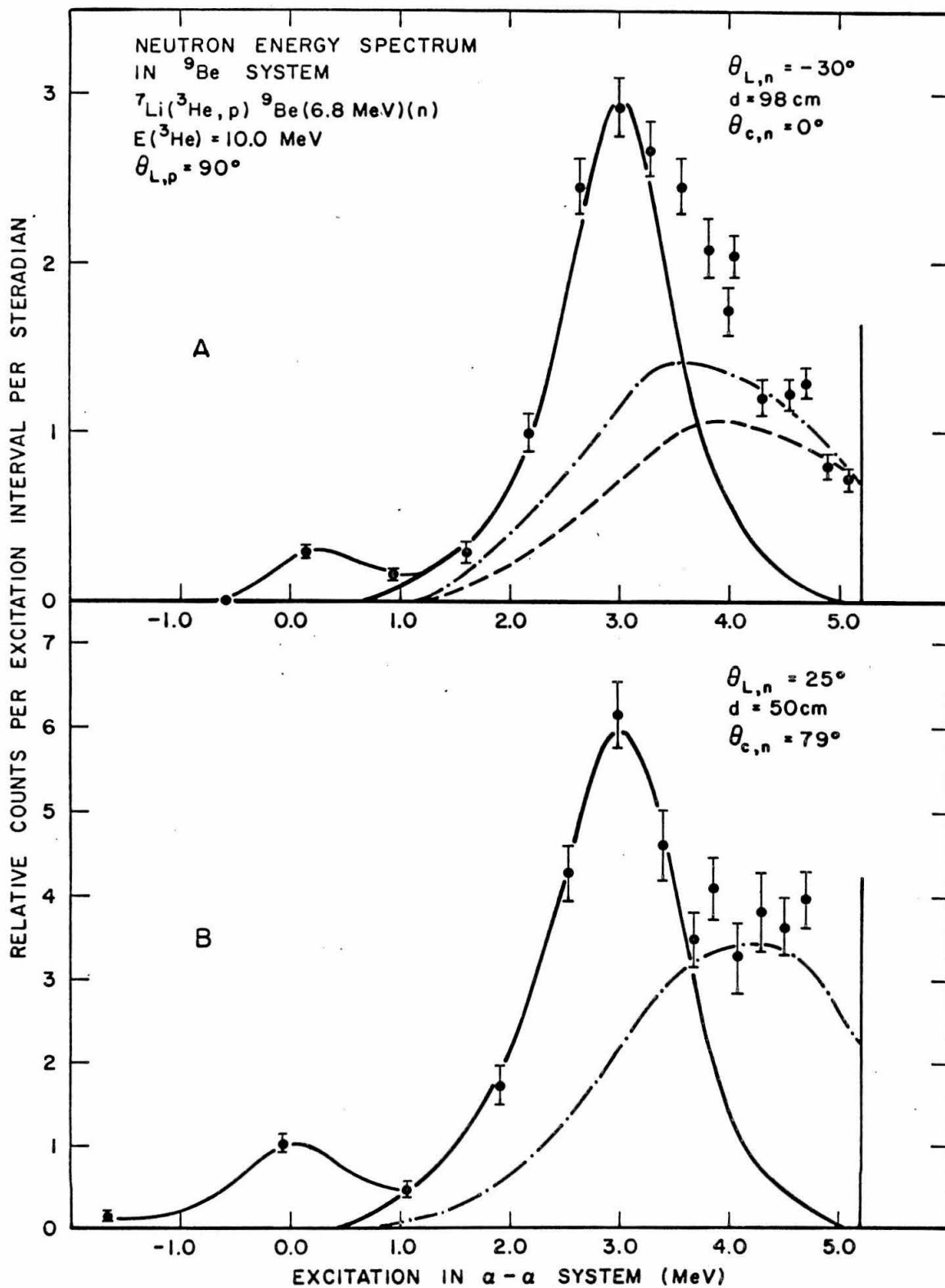
EXCITATION IN α - α SYSTEM (MeV)

Figure 34

Figure 35

An isobar diagram of the mass 9 system is shown. The entire diagram is taken from the recent compilations of Ajzenberg-Selove and Lauritsen (1966), with the exception of the excitations of levels in ^{9}Be for which the values found in the present work are given. See page 15.

Figure 35

176
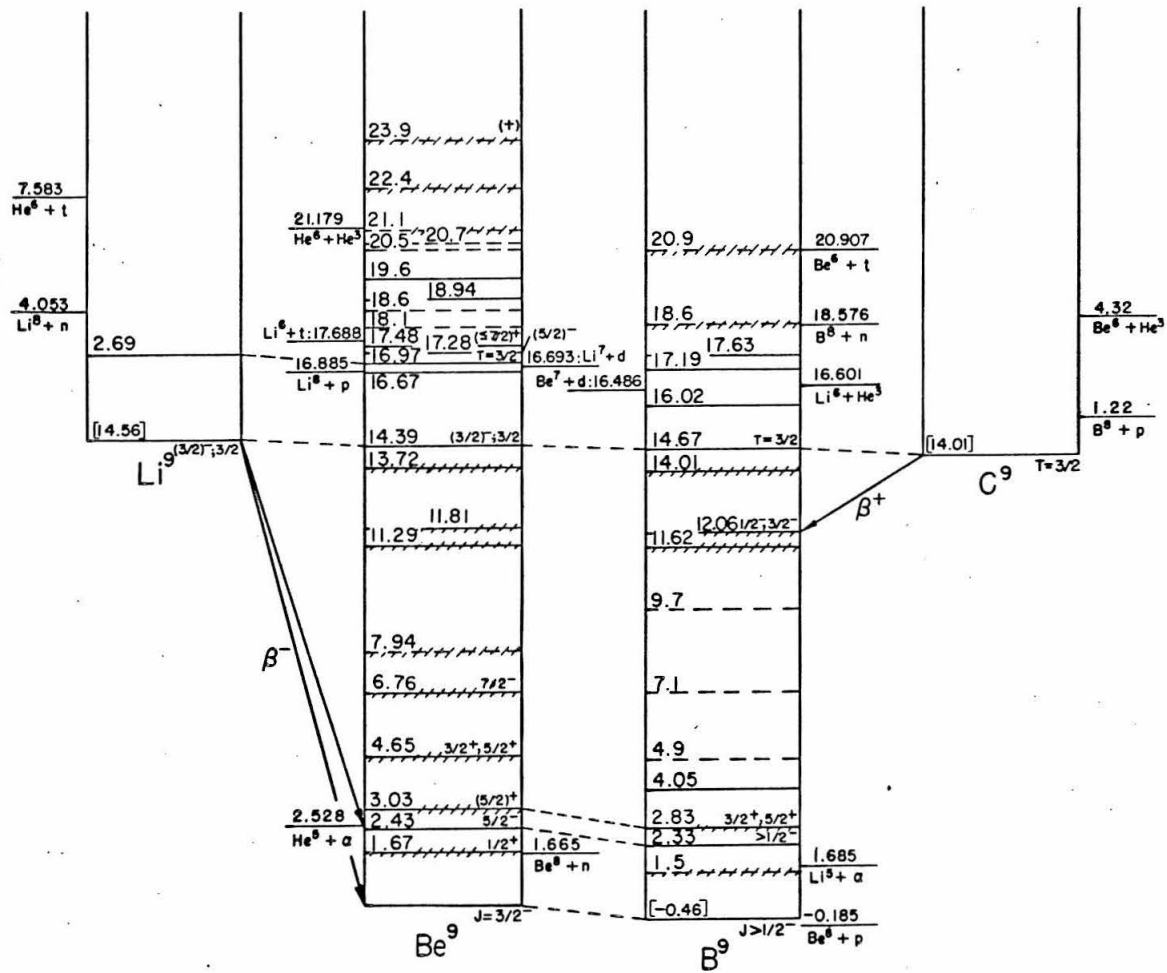
Figure 36

The positions of energy levels of ^{9}Be and ^{9}B and
with respect to two-particle decay channels are shown. The
ground states of ^{9}Be and ^{9}B have been aligned. See pages 17
and 18.

Figure 36

178

^{5}He$(3/2^-)+\alpha$

2.528

13.07
^{8}Be$(4^+)+n$

4.565
^{8}Be$(2^+)+n$

1.665

^{8}Be$(0^+)+n$

^{9}Be

14.39
13.78

11.81
11.29

7.94

6.76 $7/2^-$

4.65 $3/2^+,5/2^+$

3.03 $(5/2)^+$
2.43 $5/2^-$
1.67 $1/2^+$

3/2$^-$

^{9}B

14.67
14.01

12.06
11.62

9.7

7.1

4.9

4.05

2.83 $3/2^+,5/2^+$
2.33 $>1/2^-$

$>1/2^-$

-.185

^{8}Be$(0^+)+p$

11.21
^{8}Be$(4^+)+p$

2.715
^{8}Be$(2^+)+p$

^{5}Li$(3/2^-)+\alpha$

1.685
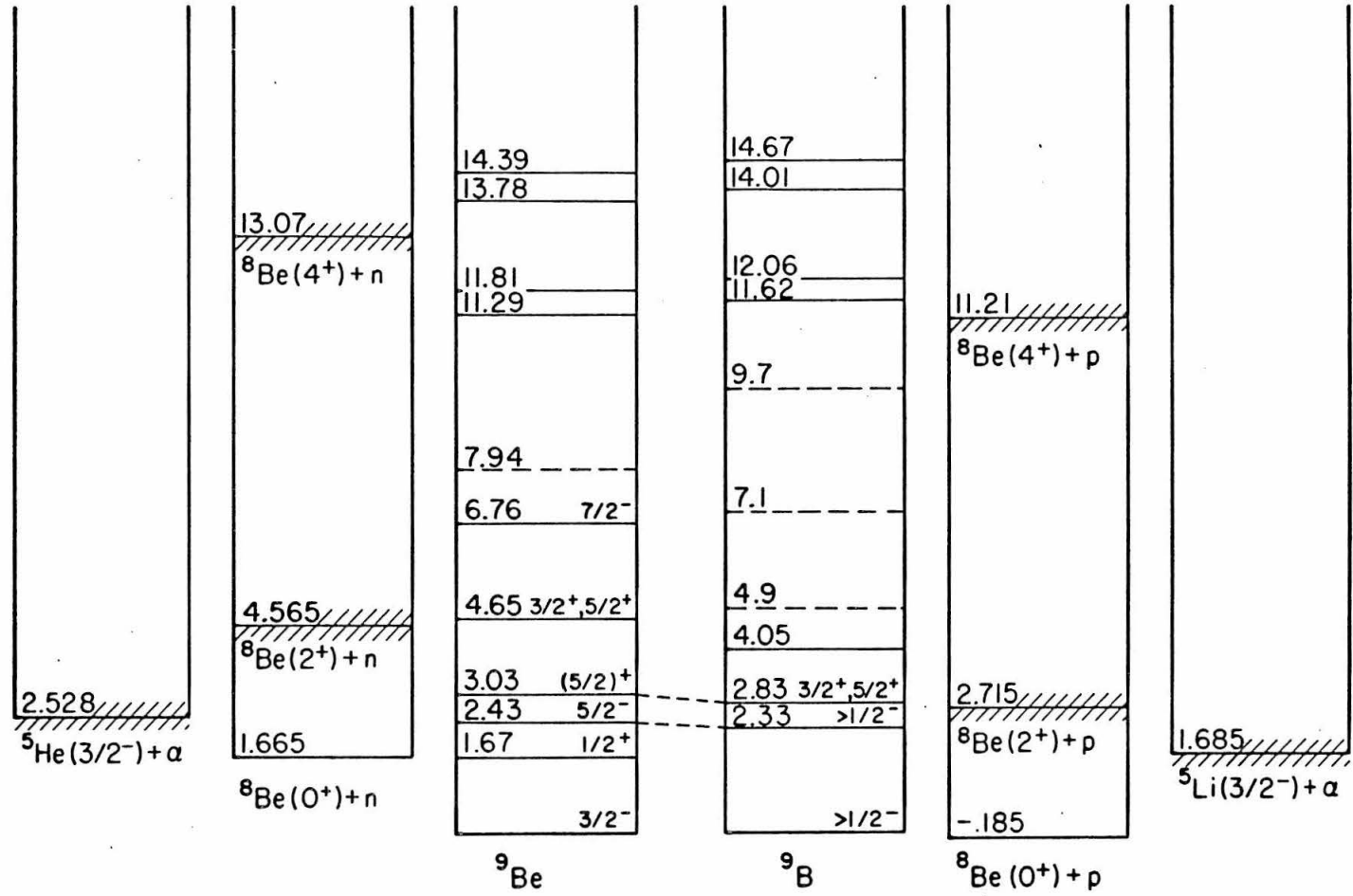
Figure 37

A comparison of theoretical and experimental level schemes for excitations below 14 MeV for ^{9}Be is shown. For the negative parity states, the intermediate coupling level scheme of Barker (1966) is given. Each state is labelled with the spectroscopic notation of the major LS-component in its wave function. See pages 46, 47 in the text for details. The level scheme predicted from a (^{8}Be + n) model (Barker, 1961) is shown. See pages 46, 47 and 48, 49 for further discussion.
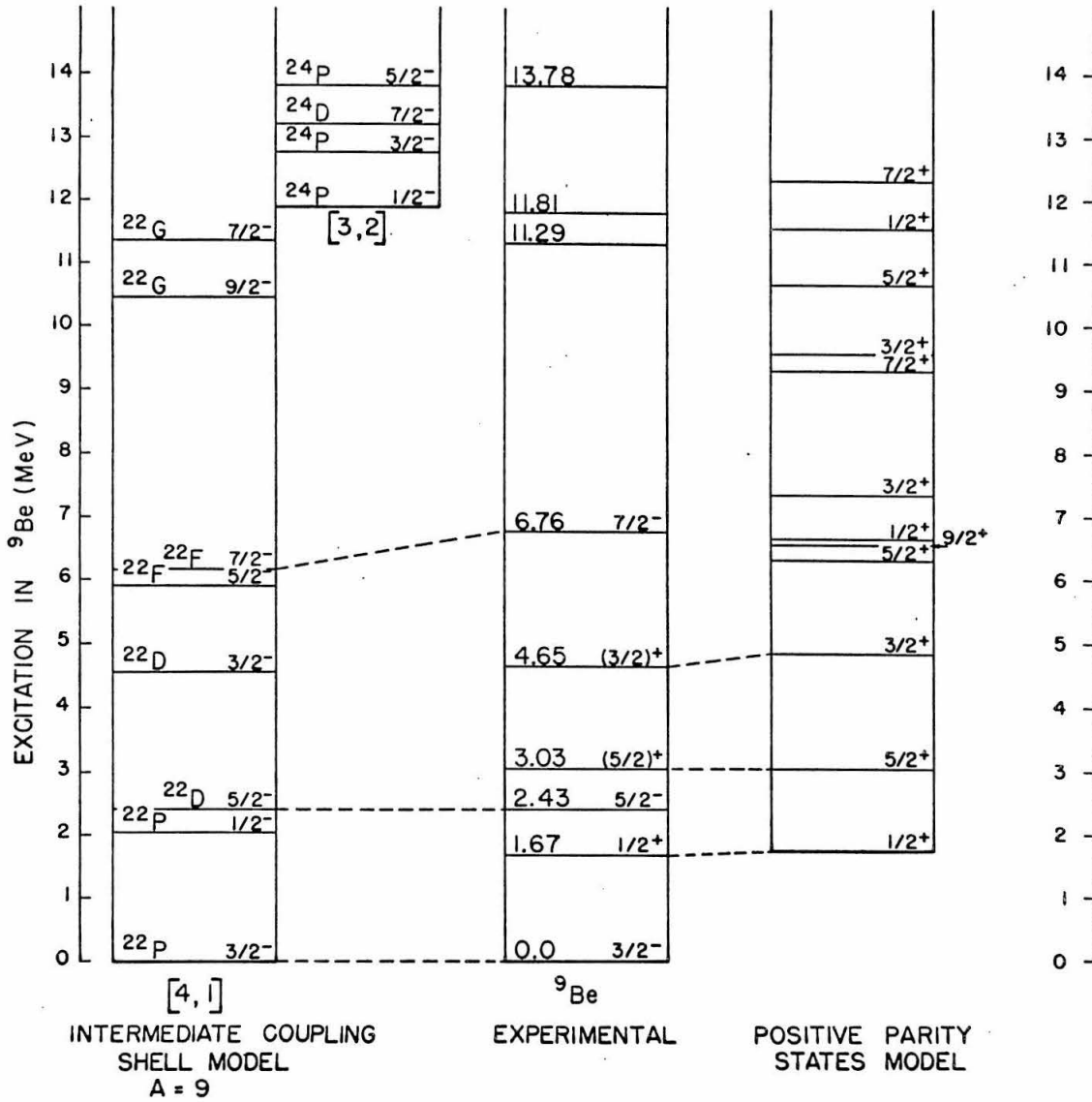
Figure 37

Figure 38

A sample energy spectrum of alpha particles from the bombardment of ^{7}Li with a 3.78 MeV ^{3}He beam is shown. The data were taken with a magnetic spectrometer and subsequently converted to an energy representation. The excitation scale has been corrected for target thickness. Groups were reported by Allen et al. at all of the indicated excitations. See page 82.
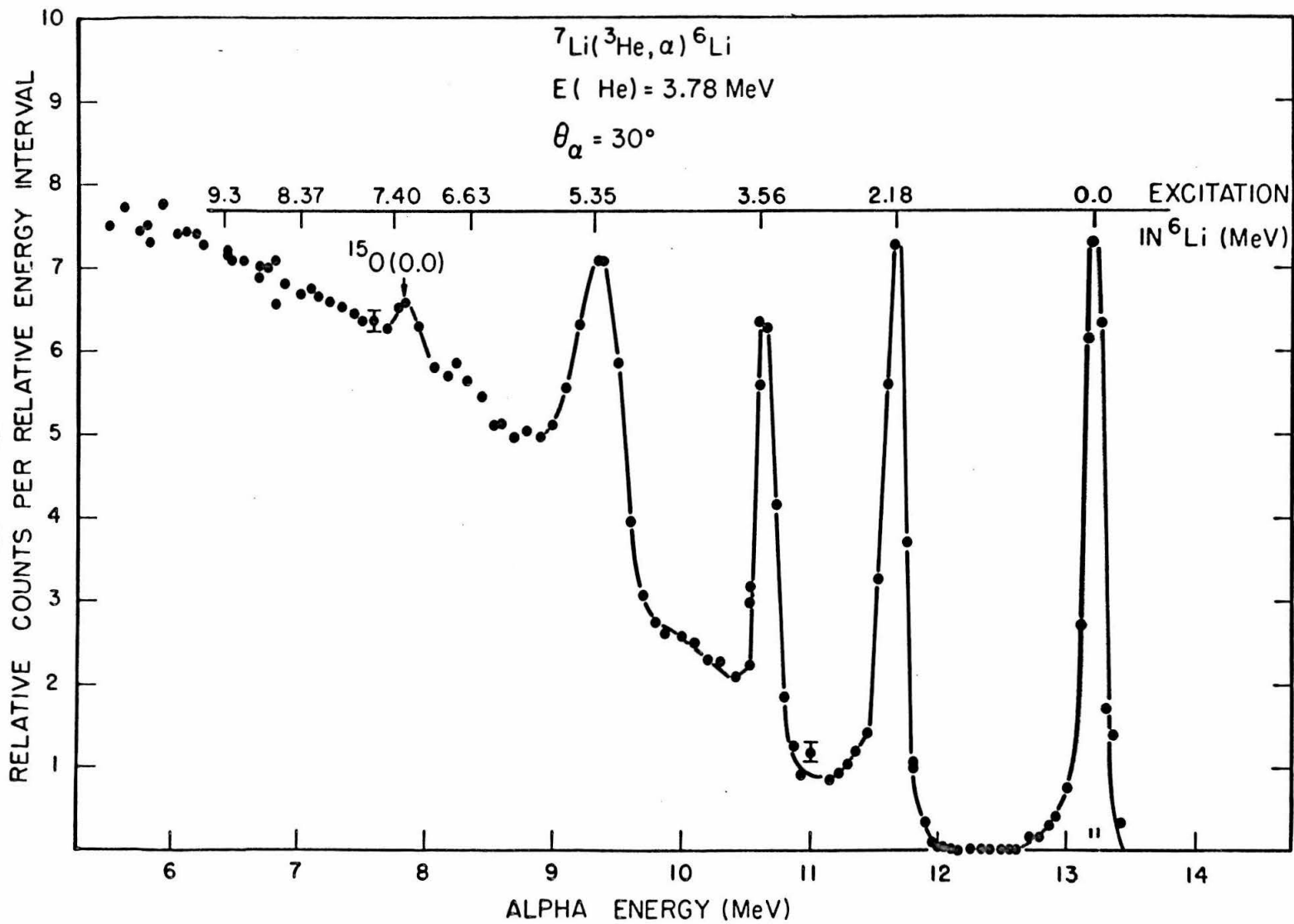
Figure 38

Figure 39

An alpha-particle spectrum taken with the magnetic spectrometer at a bombarding energy of 9.8 MeV is shown. The excitation scale has been corrected for target thickness. The kinematic limits of the alpha-particle energies from the processes ^{7}Li(^{3}He, d)^{8}Be(16.62 MeV)(α)^{4}He and ^{7}Li(^{3}He, d)^{8}Be(g. s.)(α)^{4}He are denoted by windows labelled " ^{8}Be(16.62 MeV) " and " ^{8}Be(g. s.) " respectively. The shaded group for ^{8}Be(16.62 MeV) represents the alpha-particle spectrum calculated from the measured angular distribution of the populating deuterons. See pages 82-84.
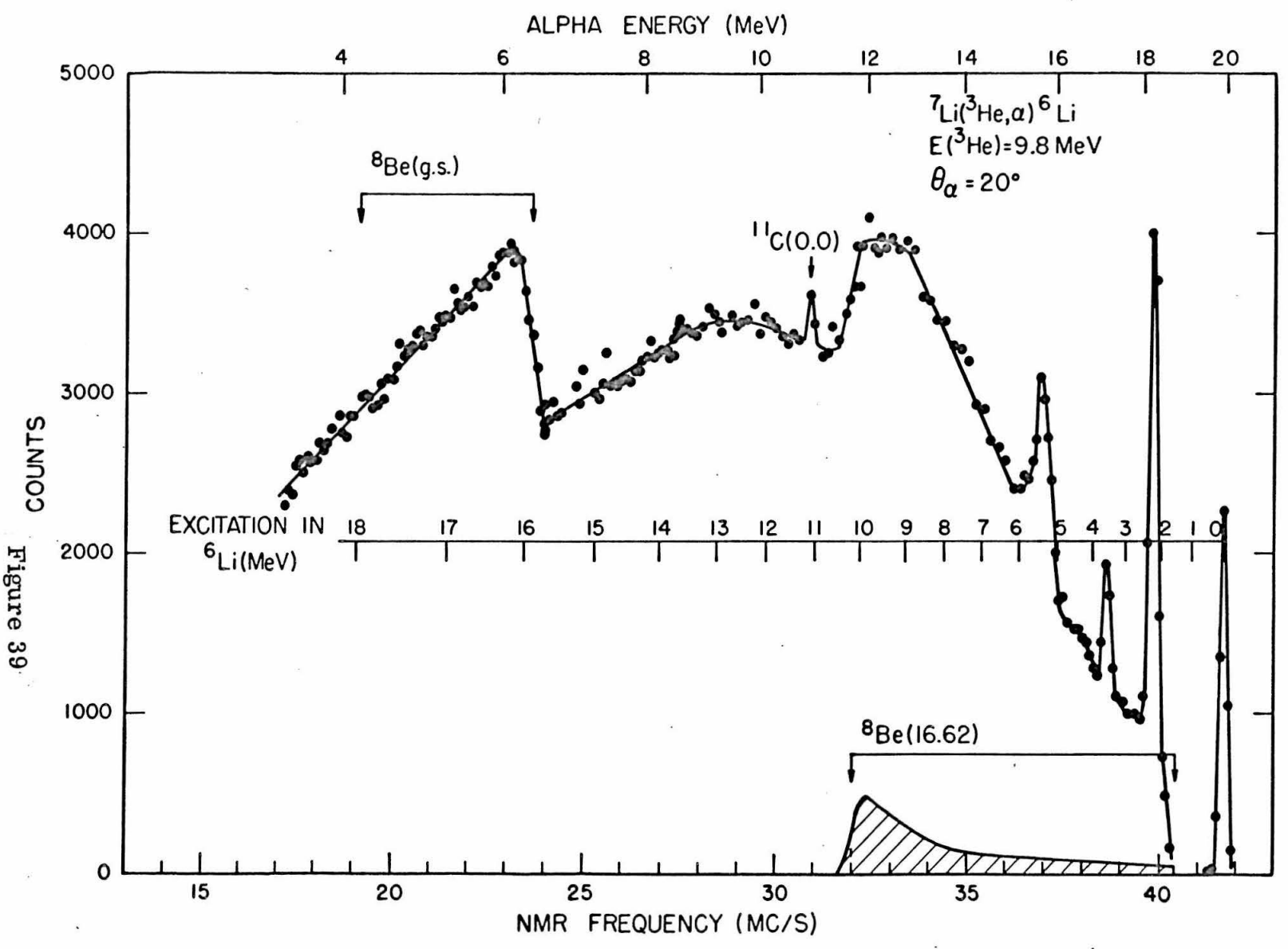
Figure 39

Figure 40

A spectrometer deuteron spectrum from the reaction ^{7}Li(^{3}He, d)^{8}Be in the region of the 16.62 and 16.92 MeV levels in ^{8}Be is shown in fig. A. Fig. B shows the center-of-mass angular distribution measured for the deuterons to the 16.62 MeV level in ^{8}Be. The solid line in fig. B is the shape used in calculating the alpha-particle energy spectrum from the decay of this state. See pages 83 and 84.
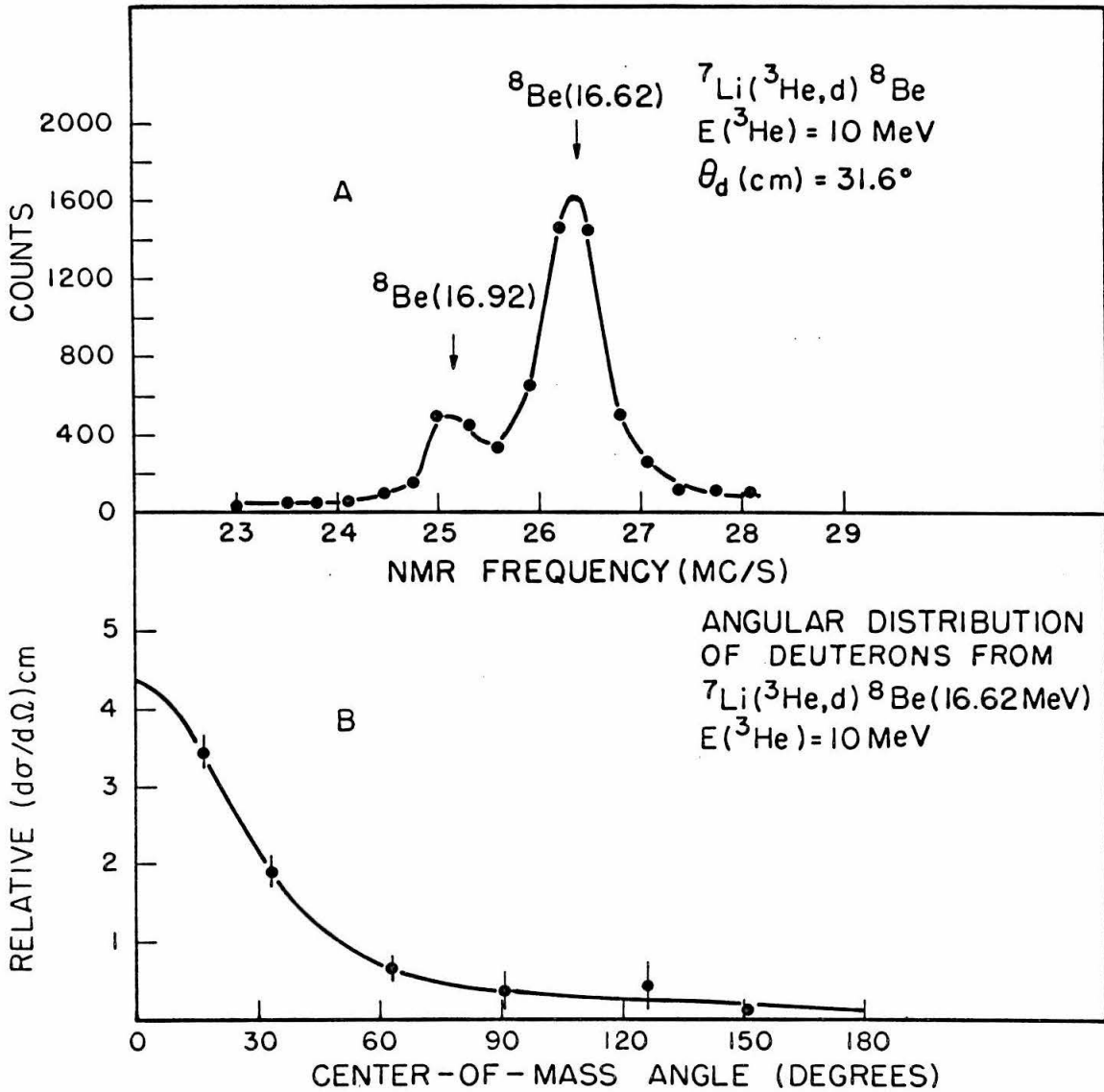
Figure 40

Figure 41

A series of alpha-particle spectra taken at different bombarding energies are shown. The calculated kinematic limits on the alpha-particle energies from the sequence ^{7}Li(^{3}He, d)^{8}Be(16.62 MeV)(α)^{4}He are indicated by windows labelled "^{8}Be(16.62)". The low energy edge of the observed group follows nicely the kinematics for this process. The expected kinematic behavior of a group from ^{7}Li(^{3}He,α)^{6}Li (9.3 MeV) is indicated for comparison. Threshold for the ^{7}Li(^{3}He, d)^{8}Be(16.62 MeV) is at E(^{3}He) = 6.94 MeV. See page 84.
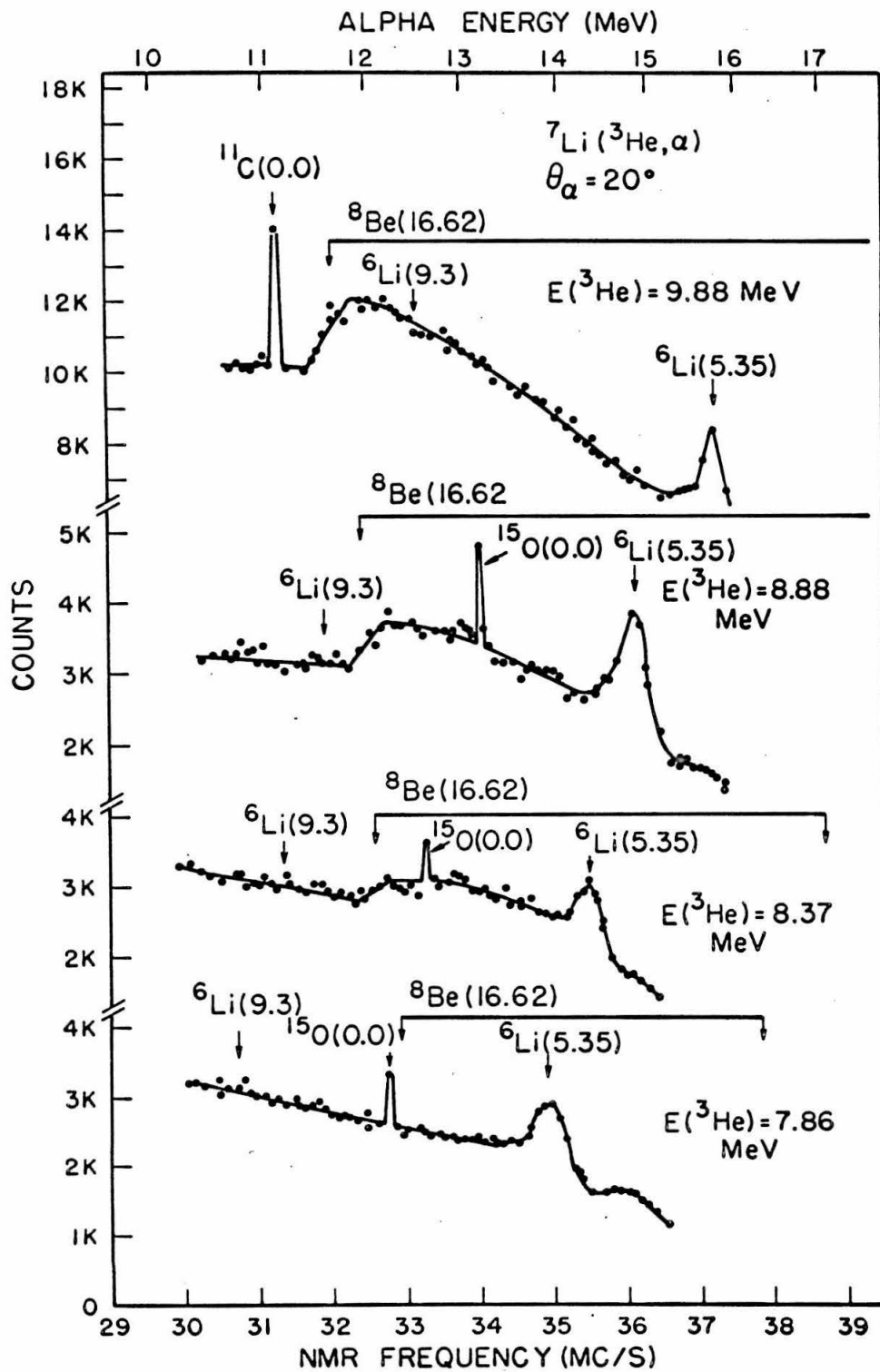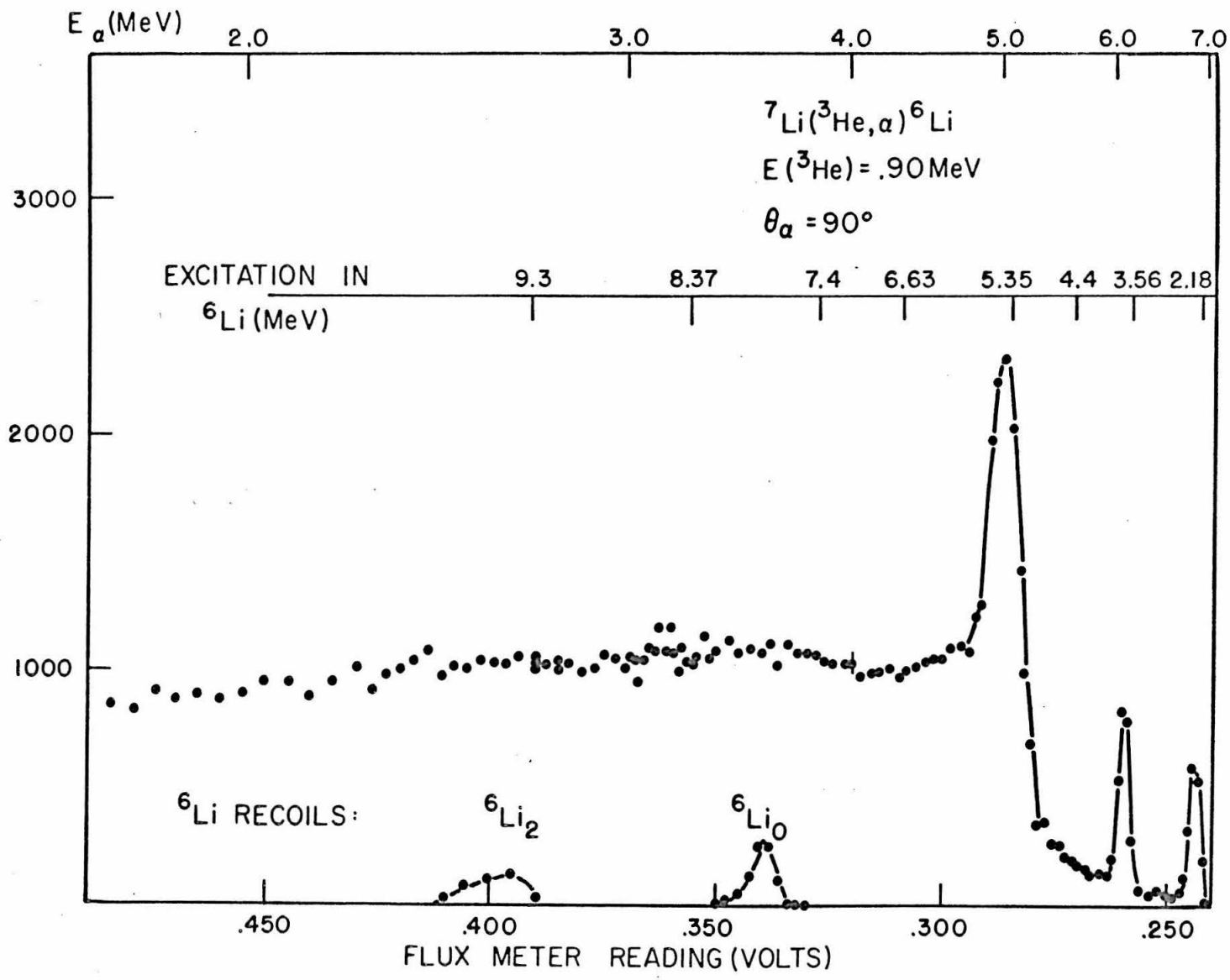
Figure 41

Figure 42

    This magnetic spectrometer alpha-particle spectrum
from ^{7}Li(^{3}He,α)^{6}Li was taken at the same bombarding energy
and angle as was that of Allen et al.   The abscissa fluxmeter
reading is inversely proportional to the alpha particle
momentum.   The excitation scale has not been corrected for
target thickness.   Alpha particles to the ground state of ^{6}Li
were too energetic to be detected by the spectrometer.
Groups were seen by Allen et al. at all of the excitations
indicated on the scale.   See page 85.

Figure 42

Figure 43

The spectrum of fig. 42 is shown in an alpha-particle
energy representation.   The excitation scale has not been
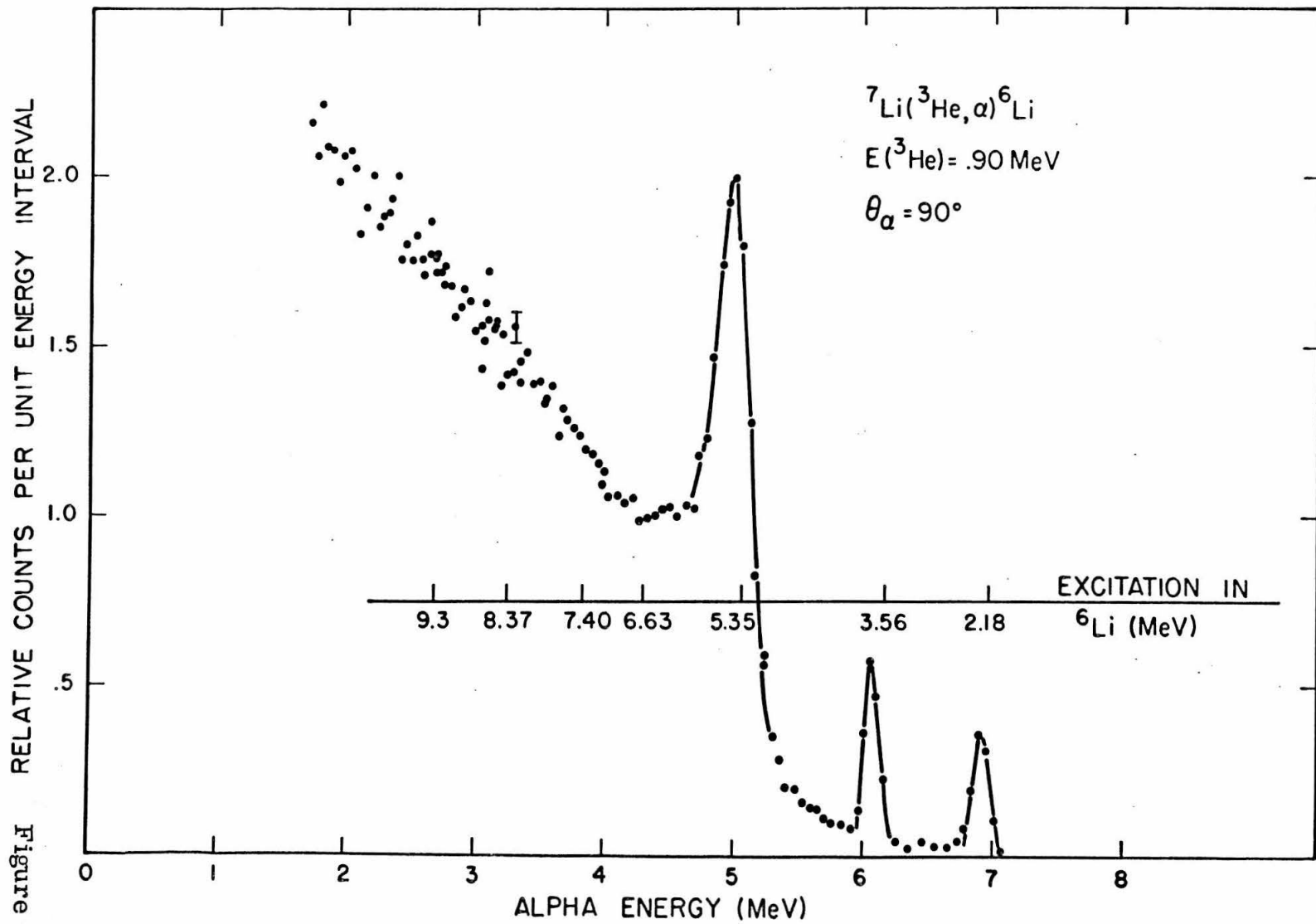corrected for target thickness.   See page 85.

$^7Li(^3He, \alpha)^6Li$

$E(^3He) = .90$ MeV

$\theta_\alpha = 90°$

EXCITATION IN ^6Li (MeV)

9.3   8.37   7.40   6.63   5.35   3.56   2.18

RELATIVE COUNTS PER UNIT ENERGY INTERVAL

ALPHA ENERGY (MeV)

Figure 43